Low-Grade Waste Heat Upgrade and Utilization through Advanced Adsorption Technologies: Open Carbon Dioxide Adsorption and Adsorption Heat Transformer

刘, 雪涛

Low-Grade Waste Heat Upgrade and Utilization through Advanced Adsorption Technologies: Open Carbon Dioxide Adsorption and Adsorption Heat Transformer

Dissertation

Liu Xuetao

June 2024

Interdisciplinary Graduate School of Engineering Science

Kyushu University, Japan

Low-Grade Waste Heat Upgrade and Utilization through Advanced Adsorption Technologies: Open Carbon Dioxide Adsorption and Adsorption Heat Transformer

A dissertation submitted in partial fulfilment of the requirements for the award of the degree of

Doctor of Philosophy

By

Liu Xuetao

Supervisor: **Professor Takahiko Miyazaki**

Co-supervisor: **Associate Professor Kyaw Thu**

Interdisciplinary Graduate School of Engineering Science

Declaration

I hereby declare that except where specific reference is made to the work of others, the contents of this dissertation are original and have not been submitted in whole or in part for consideration for any other degree or qualification in this, or any other university. This dissertation is my own work and contains nothing which is the outcome of work done in collaboration with others, except as specified in the text and Acknowledgements. This dissertation, submitted in partial fulfillment of the requirements for the Doctor of Philosophy degree at the Interdisciplinary Graduate School of Engineering Sciences, Kyushu University, Japan, represents an authentic record of my original research contributions.

Liu Xuetao

June 2024

Acknowledgements

I would like to express my gratitude to Professor Takahiko Miyazaki for providing me with the opportunity to study and conduct research at Kyushu University. Without his assistance, I would not have been able to enroll and successfully obtain my doctoral degree. His meticulous care and generous guidance have benefited me tremendously in both life and research, motivating me to persevere.

I am also truly grateful to Professor Kyaw Thu for his guidance and support in my research endeavors. Possessing exceptional research acumen and a rigorous academic attitude, he inspired me to continuously generate fruitful research ideas. His broad academic perspective and unwavering pursuit of scientific knowledge are deeply admirable, profoundly influencing my research career.

I extend my thanks to Dr. Takata for his assistance in the laboratory work. I am also grateful to Ms. Yamato for her support in financial and other administrative matters. Their selfless dedication and commitment to their roles have provided reliable support for my research, enabling me to complete my dissertation on schedule.

I would like to thank all members in Thermal Energy Conversion Systems Laboratory for their help and care in both life and research. The experience of getting on with them will be a precious treasure in my life.

Furthermore, I am grateful for the financial support provided by the China Scholarship Council (CSC), which enabled my research to proceed smoothly.

Finally, I must thank my family. Despite the ocean separating us, you have always provided me with understanding and emotional support when I needed it most. You

are my solid backbone.

Table of Contents

Abstract

The escalating industrial energy consumption and the associated environmental impacts necessitate innovative solutions for energy recovery and environmental sustainability. This thesis addresses the critical area of low-grade waste heat upgrade and utilization using advanced adsorption technologies. The primary focus is on the development of dynamic models for a large pressure jump (LPJ)-driven adsorption heat transformer (AHT) system, and the scaling analysis of open carbon dioxide (CO_2) adsorption process and cycle. These methodologies are applied to enhance the utility of low-grade waste heat and capture CO_2, which is often overlooked due to technological constraints.

The thesis begins by delving into the dynamic modeling of the LPJ-driven AHT system. This system utilizes a novel approach to elevate the temperature of low-grade heat to levels suitable for industrial use. The study explores various configurations and operational strategies of the AHT system, evaluating its performance under different conditions to maximize efficiency and stability.

Subsequent chapters discuss the scaling analysis of open CO_2 adsorption process, aimed at capturing atmospheric CO_2 from flue gas. A detailed theoretical and computational study establishes a robust framework for understanding the interplay of fluid flow and heat and mass transfer. This analysis leverages computational fluid dynamics (CFD) simulations to validate the scaling models, ensuring their accuracy and applicability in practical scenarios. The integration of the AHT system with CO_2 temperature swing adsorption (TSA) is also examined, showcasing potential improvements in system efficacy through synergistic operations. In addition,

sensitivity analyses are conducted to identify key parameters that significantly influence system performance, providing insights for future design and operational strategies.

In conclusion, this work not only advances the theoretical and practical understanding of adsorption-based heat transformer system but also demonstrates the potential in contributing to sustainable industrial practices. By pushing the boundaries of current technology, this research highlights the feasibility of recovering and upgrading low-grade waste heat as a valuable resource, aligning with global efforts towards improved energy efficiency and reduced carbon emissions.

List of Figures

List of Tables

Nomenclature

C	Concentration (mol/m^3)
C_P	Specific heat capacity (J/kg K)
D, d	Diameter (m)
D_c	Crystal diffusivity (m^2/s)
D_k	Knudsen diffusivity (m^2/s)
D_m	Molecular diffusivity (m^2/s)
D_p	Pore diffusivity (m^2/s)
E	Total energy (J/m^3)
E_a	Activation energy (J/mol)
ΔH	Molar adsorption heat (J/mol)
h	Sensible enthalpy (J/kg)
J	Diffusion flux (kg/m^2 s)
k	Thermal conductivity (W/m K)
K_0	Adsorption constant at infinite dilution (1/Pa)
K_{eq}	Equilibrium adsorption constant (1/Pa)
k_f	Film mass transfer coefficient (m/s)
k_L	Adsorption time constant (1/s)
L/D	Length-diameter ratio
M	Molar mass (kg/mol)
n	Heterogeneity constant
P	Pressure (Pa)
q	Adsorption uptake (mol/kg)
q^*	Equilibrium adsorption uptake (mol/kg)
q_m	Maximum capacity of adsorption uptake (mol/kg)
R	Gas constant (J/mol K)
r	Radius (m)
R_{re}	Removal rate
S	Sensitivity
t	Time (s)
T	Temperature (K)
v	Velocity (m/s)
X	Adsorption domain length (m)

X_i	Mole fraction of component i
x_i	Input variable for sensitivity analysis
Y	Adsorption domain width (m)
Y_i	Mass fraction of component i
y_j	Output variable for sensitivity analysis

Greek symbols

μ	Dynamic viscosity (Pa/s)
ε	Porosity
ρ	Density (kg/m^3)
τ	Stress tensor (Pa)
τ_p	Pore tortuosity

Subscripts

ad	Adsorption
c	Crystal
eff	Effective
eq	Equilibrium
feed	Feeding
HR	heat-removing
in	Inlet
max	Maximum
out	Outlet
p	Particle
po	Pore
s	Solid
sy	Symmetry
w	Wall

Chapter 1 Introduction

1.1 Background

Due to the burning of fossil fuels, deforestation, and changes in land utilization, the concentration of greenhouse gases in the atmosphere has increased, leading to a rise in global ambient temperature [1,2]. According to the relevant assessment [3], human activities have caused global temperature to rise by approximately 1.2 ^{o}C since industrialization. If the current rate persists, the global temperature rise is projected to reach 1.5 ^{o}C between 2030 and 2052. With the growing awareness of global warming and climate change, the need for reducing greenhouse gas emissions has become more pressing than ever. In December 2015, the 21th Session of the Conference of the Parties to the United Nations Framework Convention on Climate Change was held in Paris, France, where the Paris Agreement was reached [4]. The agreement stipulates that all countries should strive to achieve the peaking of global greenhouse gas emissions as soon as possible, in order to achieve the global climate neutrality by the middle of this century. Carbon dioxide (CO_2) is a major contributor to greenhouse gas emissions, while CO_2 capture and storage have been identified as an important strategy for mitigating the impact of climate change.

In addition, energy scarcity and environmental pollution have become severe challenges facing society today [5–8]. In global energy consumption, the industrial sector accounts for a significant share. A substantial amount of low-to-medium temperature waste heat is directly released during production processes, resulting in

massive energy waste. According to a report from the U.S. Department of Energy [9], 20-50% of the energy consumed in the industrial sector is lost in the form of waste heat, with 60% of it being below 230 ºC. Recovering and utilizing the low-to-medium temperature waste heat is crucial for improving energy efficiency, reducing greenhouse gas emissions and achieving sustainable development.

However, that is facing numerous challenges. On one hand, the dispersed and intermittent nature of waste heat sources poses difficulties in collection and storage [10]. On the other hand, the low-grade waste heat has a narrow application range and can even be challenging to utilize [11]. Fig. 1.1 illustrates the temperature requirements for various industrial applications in the low-to-medium temperature range. Evidently, the utilization rate of waste heat below 100 ºC in industry is relatively low. Furthermore, traditional technologies of waste heat utilization, such as power generation and absorption refrigeration, have low efficiency in the low-grade range. Therefore, it is necessary to develop efficient low-grade waste heat upgrade and utilization technologies [12,13].

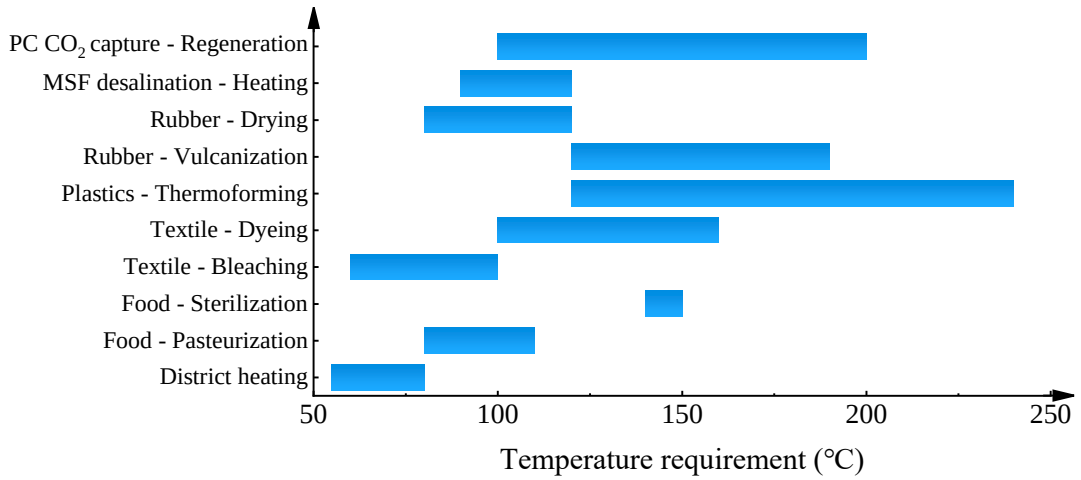

Fig. 1.1 Temperature requirements for different applications in range of low-to-

medium temperature [14–18,1].

1.2 Adsorption heat transformer for waste heat upgrade

Among existing studies, widely used waste heat upgrade technologies include mechanical vapor compression heat pump [19–21], chemical heat transformer [22] and absorption heat transformer [23–25]. Mechanical vapor compression heat pump performs well in the engineering applications requiring low-grade heat, such as district heating and hot water supply. While for high-temperature heat demands, challenges arise in the selection of refrigerants and the limitations in discharge pressure and temperature of compressors [26]. Chemical heat transformer often suffers from drawbacks such as poor cyclic stability of working pairs and slow reaction kinetics, hindering its wider application [27,28]. Absorption heat transformer usually employs harmful working pairs and may experience crystallization phenomenon [29].

Solid adsorption system offers advantages such as environmental friendliness, simple structure and the ability to utilize various heat sources, making it promising in various applications related to heat conversion. In the field of adsorption cooling, Naseem et al. [30,31] experimentally and theoretically analyzed a coupled system of an adsorption chiller with a proton exchange membrane fuel cell, achieving the recovery of waste heat generated by fuel cell unit through tri-generation of cooling, heating and power. Liu et al. [32,33] utilized a single-axis parabolic trough solar collector to provide heat for adsorbent bed, realizing summer cooling and winter heating. Based on the coefficient of performance and specific cooling power, they

found that the silica gel system outperformed the zeolite system for this application. Xu et al. [34–36] proposed a hybrid adsorption cooling system incorporating efficient desiccant coated heat exchanger, capable of utilizing heat sources in the range of 50-80 °C to provide chilled water and dry air. Thu et al. [37,38] developed an advanced adsorption cooling and desalination system with three beds and two evaporators, converting low-grade heat into cooling and desalinated water. Additionally, they established comprehensive numerical models considering mass recovery through pressure equalization and validated with relevant experiment. In the field of adsorption heat pump, Pal et al. [20] proposed a hybrid heat pump integrating chemical adsorption and mechanical compression, evaluating and acknowledging its technical and economic feasibility. AL-Dadah et al. [39] tested the performance of organic metal frameworks, aluminium fumarate, CPO-27(Ni) and MIL-100(Fe) in water-based adsorption heat pumps, demonstrating their superiority over traditional silica gel. For open-cycle adsorption heat pump, Li et al. [40] prepared super-hydrophobic zeolite 13X to improve the migration behavior of liquid water in adsorption bed, thereby significantly increasing the system performance coefficient. In the field of adsorption heat storage, Li et al. [41] conducted energy and exergy analyses of a residential heat storage system at low charging temperature, finding that the flow rate in adsorption bed has a greater impact on system performance than that in desorption bed. Schreiber et al. [42,43] evaluated the case of combining a heat storage system with combined heat and power generation to supply heat to a brewery, revealing a significant reduction in primary energy consumption for batch process. Besides, they experimentally investigated the heat loss coefficient of the adsorption heat storage system and recommended high-temperature charging for short-term storage to reduce heat loss and improve energy storage density.

In the field of waste heat upgrade, the adsorption technology exhibits stable cyclic performance, low toxicity of working pairs and excellent kinetics compared to other technologies. Chandra and Patwardhan [44] first proposed and theoretically studied the adsorption heat transformer (AHT) cycle based on zeolite/water, consisting of two adiabatic processes and two isothermal processes. Aristov et al. [45–47] proposed the "Hecol" cycle and conducted extensive research on heat upgrade in cold environment. In contrast to the AHT cycle, the "Hecol" cycle is externally heated or cooled during the preheating and precooling stages to meet the temperature requirements of next stages, thus requiring the prior provision of high-temperature and medium-temperature heat sources. Engelpracht et al. [48] simulated the dynamic operation of a single-bed AHT system that upgrades waste heat from 90 °C to 110 °C with the assistance of high-temperature heat source and optimized the design from the perspective of heat exchanger and cycle. Saren et al. [49,50] developed equilibrium models for a multi-effect desalination (MED) system coupled with waste heat driven AHT, and its performance was found to be superior to the pure MED system under the same temperature conditions. They also optimized the coupled system in terms of working pair selection and internal heat recovery.

1.3 Open CO_2 Adsorption

Adsorption technology is gaining increased attention as a promising approach for CO_2 capture [51–53]. In an open adsorption process, the adsorbate gas is adsorbed at the ambient pressure while flowing through an adsorption bed/column. Open adsorption systems have been widely applied in the dehumidification [54,55], heat storage [56,57] and adsorption refrigeration/heat pump system [40]. In CO_2 capture,

the open adsorption is usually applied in the flue gas treatment and direct air capture (DAC) [58–61], and has the advantages of low product loss, high recovery rate and stable operation compared to the closed adsorption systems [62]. Haghpanah et al. [63] simulated the vacuum swing adsorption of CO_2 in dry flue gas by zeolite 13X, obtaining results that pressurizing feed gas and vacuum depressurization were beneficial to improving productivity but also increased energy consumption. Qasem et al. [64] investigated the same system using Mg-MOF-74 and further found that the addition of a rinse process exhibited enhanced CO_2 capture performance. Besides, Liu et al. [65] and Wu et al. [66] experimentally explored the approaches to improve the performance of temperature swing adsorption system. Table 1.1 summarizes the relevant studies using the open adsorption process for CO_2 capture [10 – 22]. Improving the layout of adsorption cycle system and designing an efficient adsorption bed are crucial for enhancing overall performance.

Fig. 1.2 shows the working process of open CO_2 adsorption. The flue gas from processes goes through dust removal, desulfurization and denitrification during pretreatment, and then enters the adsorption bed for CO_2 capture. The treated decarbonized gas can be discharged directly, while the CO_2 product is further utilized or stored. Due to the exposure to the external environment, the open adsorption process is accompanied by relatively stable pressure and are commonly adopted in systems with temperature swing adsorption (TSA) [59,62,66–68], vacuum swing adsorption (VSA) [69,70] and temperature vacuum swing adsorption (TVSA) [62,67,71]. Fig. 1.3 introduces the difference in the operating steps of these systems.

The TSA typically includes adsorption, heating and cooling. In the adsorption step, the flue gas flows into the open adsorption bed, in which CO_2 is adsorbed. In the

heating step, the adsorbed CO_2 is desorbed at the high temperature, discharged from the inlet, and collected. In the cooling step, the adsorption bed is enclosed and cooled up to the initial temperature. The low-grade thermal energy sources such as solar energy or waste heat may be insufficient to change the temperature between the adsorption and desorption phases in this process. As shown in Fig. 1.3 (b), VSA generally consists of adsorption, blowdown, evacuation and pressurization steps. The adsorption process is the same as that in TSA, which is an open process. In the blowdown step, a vast majority of N_2 is expelled from the outlet through a vacuum pump in a relatively short time to improve the purity of the CO_2 product. In the evacuation step, CO_2 in the adsorption bed is desorbed and pumped out from the other end by vacuum depressurization. In the pressurization step, only the inlet of the adsorption bed is kept open, and the flue gas is replenished until the pressure in the bed rises to the initial pressure. The adsorbate CO_2 is adsorbed at atmospheric and desorbed at an ultra-low pressure by vacuum. The necessity of extremely low desorption pressure for high CO_2 recovery, the VSA process faces severe technological and economical challenges.

The TVSA process overcomes the abovementioned bottlenecks posed by the TSA and VSA processes by using a combination of temperature increase and depressurization in the desorption process. As shown in Fig. 1.3 (c), the typical steps include adsorption, blowdown, evacuation/heating, cooling and pressurization. Compared with TSA and VSA, the CO_2 desorption conditions in TVSA are more moderate, involving lower temperature and higher pressure [71,72]. Therefore, the utilization of waste heat or solar energy to increase the temperature in adsorption bed is suitable, thus reducing the energy consumption.

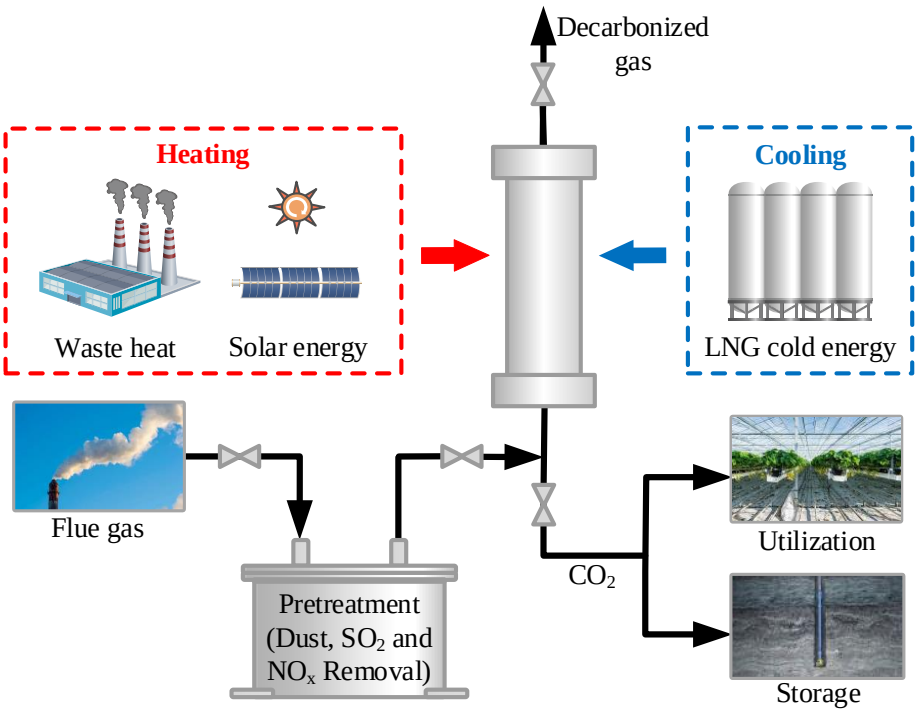

Fig. 1.2 Schematic diagram of open adsorption for CO_2 capture from flue gas.

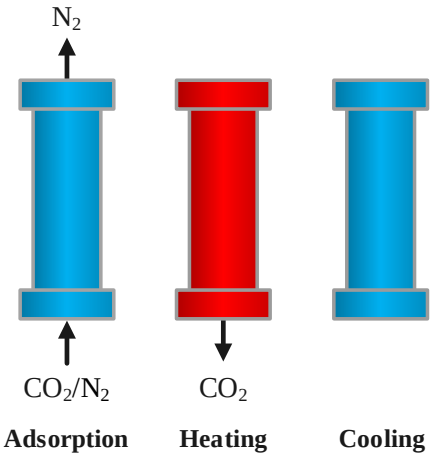

(a)

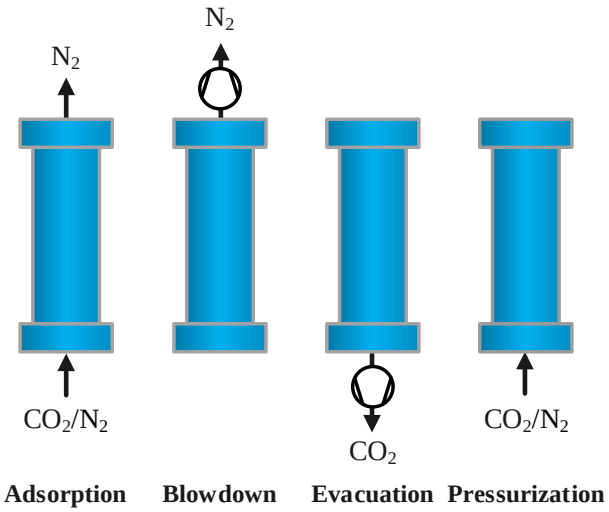

(b)

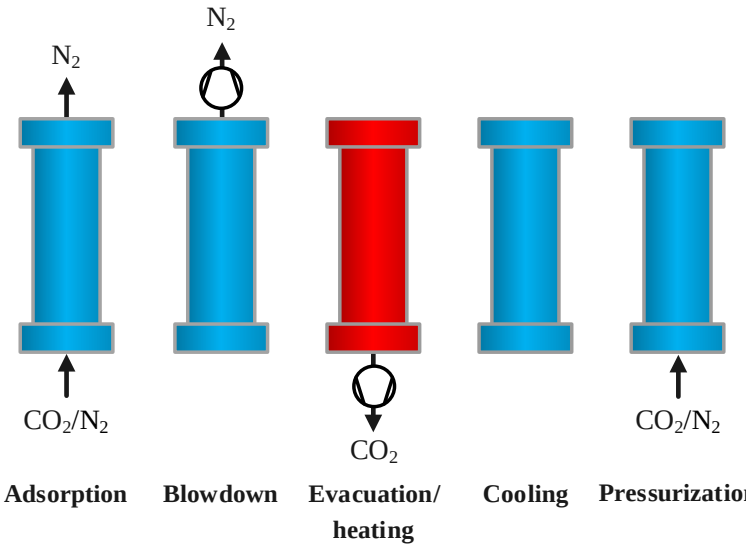

(c)

Fig. 1.3 Schematic diagrams of steps of typical open adsorption systems: (a) TSA, (b) VSA, (c) TVSA.

1.4 Objective

The principal objective of this study is to innovatively develop dynamic models for an LPJ-driven AHT system and conduct scaling analysis of open CO_2 adsorption cycle. Based on thermal load requirements, the study explores the dynamic equilibrium

performance of the integrated AHT-TSA system to achieve the "useful utilization" of low-grade waste heat. The specific objectives are outlined as follows:

(1) Address the issues of inaccurate pressure response and large fluctuations in output heat power in traditional AHT modeling and simulation. From the perspective of practical application, provide reasonable suggestions for the design and optimization of AHT system.

(2) By adopting scaling analysis to compare the terms within the governing equations describing open CO_2 adsorption process, identify the primary factors impacting fluid flow and heat and mass transfer, thereby making a deeper elucidation of the mechanisms of the behaviors. The calculation cost is reduced while the characteristics of open adsorption process are predicted.

(3) Based on the cycle description, conduct scaling analysis of the three-step TSA cycle, and investigate the performance of the single system as well as the integrated AHT-TSA system.

1.5 Thesis Outline

This thesis is organized into five chapters, addressing critical aspects of AHT dynamic modeling, open CO_2 adsorption, scaling analysis and integrated system analysis. The orderly arrangement of these chapters within this thesis is as follows:

Chapter 1: Introduction

This introductory chapter provides an overview of the motivations for studying adsorption technologies and their significance in sustainable energy applications. It

also outlines the specific objectives of this thesis and establishes the research context.

Chapter 2: Dynamic simulation of adsorption heat transformer for low-grade waste heat upgrade

Focuses on the dynamic modeling of an LPJ-driven AHT system. The chapter evaluates system performance under various operational conditions and explores the potential for maximizing the temperature lift and enhancing the system's efficiency.

Chapter 3: Scaling and sensitivity analyses of open adsorption process for atmospheric CO_2 capture

Presents the scaling analysis of open CO_2 adsorption cycles, detailing the theoretical framework and the methodology employed. It discusses the validation of these models through CFD simulations and sensitivity analysis, highlighting their implications for design optimization.

Chapter 4: Analysis of temperature swing adsorption system integrated with adsorption heat transformer

Investigates the integration of TSA with the AHT system. It examines the synergistic effects of this integration on the performance of the combined system, offering insights into optimization strategies.

Chapter 5: Conclusions and future prospects

Summarizes the key findings and contributions of the thesis. This final chapter also outlines the future research directions suggested by the results, emphasizing the potential for further advancements in adsorption technology for sustainable energy systems.

This outline ensures a logical progression of research, facilitating a thorough understanding of the complexities involved in adsorption systems and their heat and mass transfer mechanisms.

Table 1.1 Summary of studies concerning open adsorption for CO_2 capture.

Year	Author	Cycle system	Adsorbent material	Treated gas [a]	Method [b]	Research objects	Research results
2012	Wang et al. [67]	6-step TVSA 4-step VSA 5-step TSA	Zeolite 13X-APG	CO_2/N_2 (15/85)	Exp./Sim.	CO_2 purity and recovery	The novel TVSA system can achieve high CO_2 recovery and purity, which are 92.2% and 93.6%, respectively.
2012	Kulkarni et al. [59]	4-step TSA	TRI-PE-MCM-41	Dry air	Sim.	CO_2 purity, annual product throughput and cost estimate	Feasible strategies for reducing the cost of DAC are proposed by adjusting operation parameters.
2013	Haghpanah et al. [63]	4-step VSA	Zeolite 13X	CO_2/N_2 (15/85)	Sim.	CO_2 purity, recovery, productivity, specific energy consumption	Pressurizing the feed gas and vacuum depressurization are beneficial to improving productivity, but also correspondingly increase the energy consumption.
2016	Khurana et al. [69]	6-step VSA	UTSA-16 MOF	CO_2/N_2 (15/85)	Sim.	CO_2 productivity and energy consumption	A 6-step dual-reflux VSA cycle system is constructed to satisfy the industrial standard limits on CO_2 purity at the cost of certain energy consumption.
2017	Sinha et al. [73]	5-step TVSA	MIL-101(Cr)-PEI-800 and mmen-Mg_2(dobpdc)	Wet air	Sim.	Energy requirements, cost estimate	In DAC, the adsorbent mmen-Mg_2(dobpdc) exhibits a superior adsorption capacity and lower system energy consumption, which presents a promising opportunity for reducing running costs.
2018	Ben-Mansour et al. [74]	4-step TSA	Mg-MOF-74	CO_2/N_2 (15/85)	Exp./Sim.	CO_2 purity, recovery and productivity	Taking into account all factors, the optimal wall thickness, heating time and cooling time for system performance are obtained.
2018	Qasem et al. [64]	4-step VSA	Mg-MOF-74	CO_2/N_2 (15/85)	Sim.	CO_2 purity, recovery, productivity and power consumption	By adding a rinse process into the conventional VSA, the improved VSA system exhibits enhanced performance for CO_2 capture, and the optimal performance is explored.

2019	Lian et al. [75]	3-step TSA	Mg-MOF-74	CO_2/N_2 (20/80)	Sim.	CO_2 purity, recovery, productivity and energy consumption	The length-diameter ratio of adsorption bed is obtained by comparing different cases when the system performance is optimal in a fixed 2D adsorption area.
2019	Liu et al. [65]	4-step TSA	Zeolite 13X-APG	CO_2/N_2 (15/85, 17/83 and 19/81)	Exp.	CO_2 purity, recovery, energy consumption and second-law efficiency.	It is found that there is a certain effective desorption time, and beyond this time, the specific energy consumption increases, leading to the decrease of the energy efficiency of system.
2019	Zhao et al. [60]	4-step TVSA	APDES-NFC	Dry air	Sim.	Minimum separation work and second-law efficiency	The application of TVSA to CO_2 capture and ventilation system in buildings has a great potential for energy saving, providing possibilities for the realization of carbon negative buildings.
2021	Chen et al. [76]	3-step TSA	Zeolite 13X-APG	CO_2/N_2 (15/85)	Sim.	CO_2 purity, recovery, energy consumption and COP_{CO2}	A three-tube heat exchanger is proposed based on a single-tube heat exchanger in adsorption bed. The performance of the three-tube heat exchanger is better in all aspects.
2021	Zhu et al. [77]	3-step S-TVSA	MIL-101(Cr)-PEI-800 and MCF silica-PEI-80b	Wet air	Sim.	CO_2 purity, capture ratio, productivity and energy consumption	In the optimized results, 80.6% of energy consumption is from generating the regeneration steam, which demonstrates the energy-saving potential of applying solar energy or industrial waste heat to S-TVSA system.
2022	Wu et al. [66]	4-step TSA	Zeolite 13X-APG	CO_2/N_2 (13/87, 15/85, 17/83 and 19/81)	Exp.	CO_2 purity, recovery, productivity, energy consumption, COP_{CO2} and exergy efficiency.	The utilization of heat recovery and vacuum technology can improve the adsorption performance of the prototype.

a: The content in the parentheses represents the mole fraction (%) of CO_2/N_2.

b: Exp. refers to experiment, and Sim. refers to simulation.

Chapter 2 Dynamic simulation of adsorption heat transformer for low-grade waste heat upgrade

2.1 Introduction

The capability of adsorption heat transformer (AHT) system to elevate the temperature of existing heat sources marks a significant advancement in the field of energy technologies. It enhances the usability of low-temperature waste heat, which otherwise remains largely untapped due to technological constraints. Operating through an adiabatic-isothermal cycle, the AHT system predominantly utilizes the pressure difference to drive the adsorption and desorption processes within the adsorption bed, efficiently transforming heat energy.

To meet the demand for waste heat upgrade, the operation of AHT system should not involve the supply of high-temperature heat source. Instead, a portion of waste heat should be released to the environment to upgrade the remaining portion. Due to the pressure difference between the evaporator, condenser, and beds, the large pressure jump (LPJ) typically occurs within the beds [78,79], driving the adsorption and desorption processes. However, existing AHT simulation studies have neglected the consideration of LPJ in modeling, leading to inaccurate dynamic pressure responses. Additionally, these systems often exhibit significant rises and falls over the target output temperature, making it challenging to precisely meet the temperature

requirements of different applications with the upgraded heat.

In order to address the aforementioned issues, based on the lumped parameter modeling method, we established the dynamic simulation models of a dual-bed AHT system driven by LPJ for low-grade waste heat upgrade and introduced different operating stages of the system and their specific operations. The maximum temperature lift potential that governs the selection of adsorbent materials and operating conditions was analyzed. To enhance the usability and applicability of the system, two heat output modes were proposed: constant flow output (CFO) and constant temperature output (CTO). The dynamic variations and system performance of cycle were comparatively studied for the AHT system based on the AQSOA-Z05/water working pair under different modes. For the more practicable CTO mode, a sensitivity analysis was conducted to investigate the influence of different condition parameters on system performance parameters and survey the condition ranges for efficient and stable system operation. In the end, from the perspective of practical applications, reasonable suggestions were put forward for the design and optimization of AHT system to match the heat load demands of different applications.

2.2 System description

In this study, the dual-bed AHT system primarily consists of an evaporator, a condenser, a liquid pump and two adsorption beds. Fig. 2.1 illustrates its configuration as well as the operational schemes across four stages. The specific operations in different stages are described as follows:

I: V1 and V4 are opened while V2, V3, V5 and V6 are closed. The pressure inside

bed 1 increases, leading to adsorption, marking the pre-heating stage. Simultaneously, the pressure inside bed 2 decreases, leading to desorption, marking the pre-cooling stage.

II: V1 and V4 keep open, V2 and V3 keep closed. V5 and V6 are opened. V7 is connected to the heating way, while V8 is connected to the cooling way. Adsorption continues in bed 1, releasing high-temperature useful heat, marking the adsorption stage. Desorption continues in bed 2, absorbing medium-temperature waste heat, marking the desorption stage.

III: V2 and V3 are opened, V1, V4, V5 and V6 are closed. The pressure inside bed 1 decreases, leading to desorption, marking the pre-cooling stage. Conversely, the pressure inside bed 2 increases, leading to adsorption, marking the pre-heating stage.

IV: V2 and V3 remain open, V1 and V4 remain closed. V5 and V6 are opened. V7 is connected to the cooling way, while V8 is connected to the heating way. Desorption continues in bed 1, absorbing medium-temperature waste heat, marking the desorption stage. Adsorption continues in bed 2, releasing high-temperature useful heat, marking the adsorption stage.

Throughout all stages, the evaporator consistently operates under high pressure, absorbing waste heat, while the condenser remains under low pressure, releasing heat into the environment. The function of the pump is to elevate the pressure of the liquid flowing out from the condenser and convey it to the evaporator.

According to Saren et al. [49], the AHT cycle involves three temperatures: T_L, T_M and T_H, corresponding respectively to the ambient temperature, the waste heat temperature and the target temperature. Here, the target temperature lift can be defined

as follows:

$$\Delta T = T_H - T_M \tag{2.1}$$

Furthermore, there are two heat output modes: CFO and CTO. Under the CFO mode, the heat transfer fluid (HTF) flow rate of adsorption bed remains constant during the adsorption stage. Differently, under the CTO mode, the HTF flow rate of bed during the adsorption stage is adjusted in real time to maintain a constant outlet temperature. Besides, they also differ in the judgement condition for determining stage change, which will be presented and specifically explained in the next section.

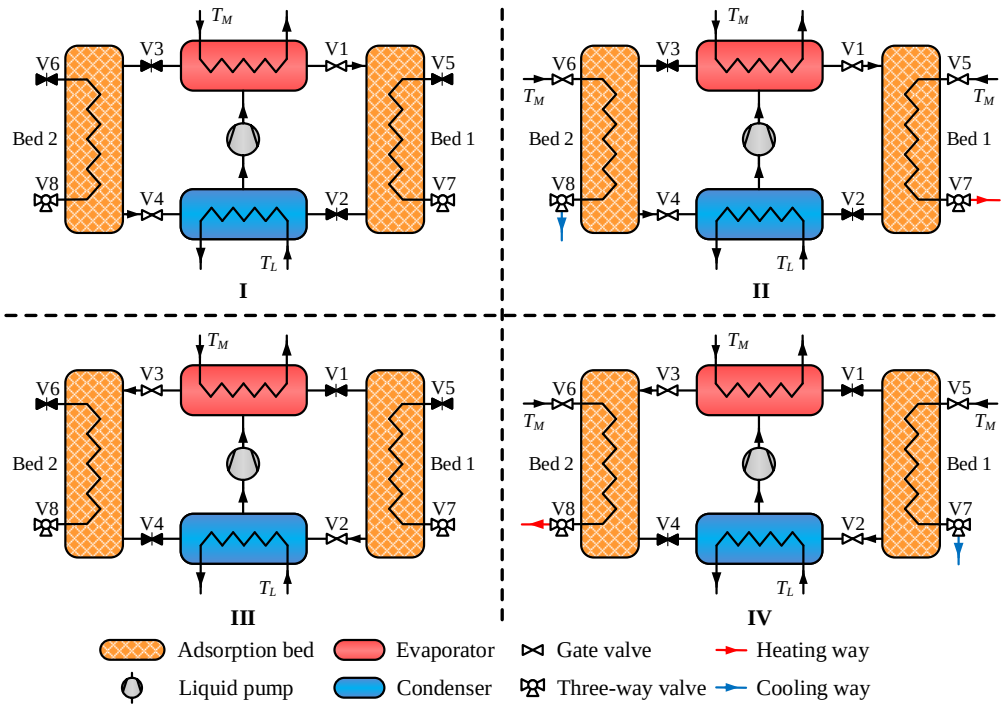

Fig. 2.1 Schematic diagram of configuration and operational schemes of dual-bed AHT system during four stages.

2.3 Modeling

2.3.1 Model assumptions

Using the lumped parameter method, the mass transfer, temperature and pressure within the dual-bed AHT system are simulated dynamically. To reasonably simplify the models, the following assumptions are adopted:

(1) In the energy equation, the adsorbent, refrigerant and heat exchanger within adsorption bed are considered to be at the same temperature. Additionally, the refrigerant and heat exchanger in the evaporator and condenser are also assumed to be at the same temperature.

(2) The thermophysical properties of the adsorbed phase are calculated based on those of the saturated liquid state.

(3) The evaporation and condensation pressures keep constant throughout the cycle.

(4) The difference between the saturation temperatures at the evaporation and condensation pressures and the corresponding HTF inlet temperatures is 3 ºC.

(5) The gas discharged from the evaporator and the liquid discharged from the condenser are both in the saturated state.

(6) The opening and closing processes of valves and their friction losses are not considered.

2.3.2 Mass transfer driven by LPJ

In this study, the adsorption and desorption behaviors are primarily influenced by the significant pressure differences between the evaporator and the adsorption bed, and between the condenser and the adsorption bed. This rapid and notable pressure change within the system is referred to as the large pressure jump (LPJ). To accurately predict the LPJ process, the mass transfer can be described by the modified Darcy formula for compressible gas flow [80], as follows:

$$\dot{m}_{LPJ} = \sqrt{2} Y A_p \sqrt{\frac{\Delta P \rho_1}{K}} \tag{2.2}$$

where K is the total resistance coefficient and ΔP is the pressure drop between inlet 1 and outlet 2. Y is the expansion factor derived from K and ΔP, and the relevant equations can be expressed as [81]:

$$Y = 1 - \frac{\mathrm{a} + K}{\mathrm{b} + \mathrm{c}K} \frac{\Delta P}{P_1} \tag{2.3}$$

$$\Delta P = \min(P_1 - P_2, \Delta P_c) \tag{2.4}$$

$$\Delta P_c = \frac{K}{\mathrm{d} + \mathrm{e}K + \mathrm{f}K^{1/2}} P_1 \tag{2.5}$$

$$K = f \frac{L_p}{D_p} \tag{2.6}$$

$$f = \begin{cases} \dfrac{64}{Re} & Re < 2300 \\ \dfrac{0.3164}{Re^{0.25}} & 2300 \le Re < 5000 \\ \dfrac{1.325}{\left[\ln\left((e_P / 3.7D_P) + (5.74 / Re^{0.9})\right)\right]^2} & Re \ge 5000 \end{cases} \quad (2.7)$$

where ΔP_c represents the critical pressure drop due to the limitation at the outlet of straight pipe where the critical flow velocity is the sonic velocity. D_p and L_p are the diameter and length of the connecting pipe between high-pressure HX and low-pressure HX. f is the friction factor. The constants a ~ f are listed in Table 2.1.

Table 2.1 Constants for calculation of expansion factor.

a	b	c	d	e	f
4.0433	3.0857	3.3579	0.1052	0.9966	0.9161

2.3.3 Components in AHT system

Based on the principles of mass and energy balance, the following models are developed to describe the changes in energy and mass of each component in the AHT system, as well as the pressure variations in the adsorption beds.

2.3.3.1 Pump

The function of liquid pump is to boost the pressure of the refrigerant from condenser outlet to the evaporation pressure, and the outlet specific enthalpy of pump can be expressed as:

$$h_{pu,out} = h_{pu,in} + \frac{h_{pu,out,is} - h_{pu,in}}{\eta_{pu}} \tag{2.8}$$

where η_{pu} represents the isentropic efficiency of pump, which is set as 0.6 [82]. $h_{pu,in}$ is the inlet specific enthalpy of pump, which is set as:

$$h_{pu,in} = h_{sl,con} \tag{2.9}$$

To ensure the mass balance of system in a cycle, the mass flow rate of pump is configured to be the real-time average of the mass transfer flow rates driven by LPJ:

$$\dot{m}_{pu} = \frac{\dot{m}_{LPJ,ads} + \dot{m}_{LPJ,des}}{2} \tag{2.10}$$

2.3.3.2 Evaporator

The energy balance of evaporator can be expressed by the lumped model as follows:

$$\begin{aligned} &\frac{d}{dt}(MC_pT)_{eva} = \\ &\dot{m}_{pu}h_{pu,out} - \dot{m}_{LPJ,ads}h_{sg,eva} - \dot{m}_{LPJ,ads}h_{fg,eva} + \left[\dot{m}C_p(T_{in} - T_{out})\right]_{eva,HTF} \end{aligned} \tag{2.11}$$

where $(MC_p)_{eva}$ includes the refrigerant in evaporator and the heat exchanger metal:

$$(MC_p)_{eva} = \left[(MC_p)_{ref} + (MC_p)_{HX}\right]_{eva} \tag{2.12}$$

The mass variation of the refrigerant in evaporator is as follows:

$$\frac{dM_{ref,eva}}{dt} = \dot{m}_{pu} - \dot{m}_{LPJ,ads} \tag{2.13}$$

2.3.3.3 Condenser

The energy balance of condenser can be represented by the lumped model as follows:

$$\frac{d}{dt}(MC_pT)_{con} = \dot{m}_{LPJ,des}h_{ref,des} - \dot{m}_{pu}h_{pu,in} + \dot{m}_{LPJ,des}h_{fg,con} + \left[\dot{m}C_p(T_{in} - T_{out})\right]_{con,HTF} \quad (2.14)$$

where $(MC_p)_{con}$ includes the refrigerant in condenser and the heat exchanger metal:

$$(MC_p)_{con} = \left[(MC_p)_{ref} + (MC_p)_{HX}\right]_{con} \quad (2.15)$$

In addition, the mass variation of the refrigerant is obtained by:

$$\frac{dM_{ref,con}}{dt} = \dot{m}_{LPJ,des} - \dot{m}_{pu} \quad (2.16)$$

2.3.3.4 Adsorption bed

In this study, AQSOA-Z05/water is chosen as the working pair to explore its application potential in the AHT system. AQSOA-Z05 is a sort of advanced zeolite adsorbent, characterized by its stability over a wide range of temperature and pressure and its high efficiency in adsorption/desorption of water vapor [83]. These attributes provide significant benefits for the energy efficiency and operation of system.

The linear driving force (LDF) model assumes a linear relationship between the adsorptive driving force and the mass transfer rate, thereby simplifying the mathematical treatment of adsorption kinetics. The LDF equation is employed to describe the change rate of uptake:

$$\frac{dq}{dt} = k_{LDF}\left(q_{eq} - q\right) \quad (2.17)$$

where k_{LDF} is the LDF adsorption time constant, which is obtained by [84]:

$$k_{LDF} = \frac{15 D_{s0}}{r_p^2} \exp\left(-\frac{E_a}{RT} \right) \tag{2.18}$$

where d_p, D_{s0} and E_a represent the particle radius, the pre-exponential factor of surface diffusivity and the activation energy, respectively.

For the working pair AQSOA-Z05/water, the equation by Sun and Chakraborty [85] has been found to be effective in fitting the S-type isotherm, thereby being utilized to calculate the equilibrium adsorption uptake [86]:

$$q_{eq} = \frac{q_0 K_{eq} \left(P / P_s \right)^m}{1 + (K_{eq} - 1) \left(P / P_s \right)^m} \tag{2.19}$$

$$K_{eq} = \alpha \exp\left[m(Q_{st}^* - h_{fg}) / R_g T \right] \tag{2.20}$$

where q_0, P_s, m, α, Q^*_{st} and h_{fg} stand for the limiting uptake, the saturated pressure, the heterogeneity constant, the pre-exponential factor, the isosteric heat of adsorption under zero surface coverage and the latent heat, respectively. All parameters used for adsorption equilibrium and adsorption kinetics are listed in Table 2.2. Besides, the adsorption isotherms from 60 to 140 °C are shown in Fig. A.1.

Table 2.2 Parameters for adsorption equilibrium and adsorption kinetics [86,87].

q_0 (kg/kg)	Q^*_{st} (kJ/kg)	m	α	r_p (mm)	D_{s0} (m^2/s)		E_a (kJ/mol)
					$P/P_{amb} > 0.1$	$P/P_{amb} < 0.1$	
0.22	2800	6.55	6.77×10^{-5}	0.5	4.85×10^{-9}	2.77×10^{-5}	38.7

The lumped energy model for the adsorption bed at different stages is presented as follows:

$$\frac{d}{dt}(MC_pT)_{bed}=\begin{cases}\dot{m}_{LPJ,ads}h_{sg,eva}+M_a\dfrac{dq}{dt}Q_{st} & \text{Pre-heating}\\ \dot{m}_{LPJ,ads}h_{sg,eva}+M_a\dfrac{dq}{dt}Q_{st}+\left[\dot{m}C_p(T_{in}-T_{out})\right]_{ads,HTF} & \text{Adsorption}\\ -\dot{m}_{LPJ,des}h_{ref,des}+M_a\dfrac{dq}{dt}Q_{st} & \text{Pre-cooling}\\ -\dot{m}_{LPJ,des}h_{ref,des}+M_a\dfrac{dq}{dt}Q_{st}+\left[\dot{m}C_p(T_{in}-T_{out})\right]_{des,HTF} & \text{Desorption}\end{cases} \tag{2.21}$$

where $(MC_p)_{bed}$ encompasses the adsorbent, free and adsorbed refrigerant in bed, and the heat exchanger metal:

$$(MC_p)_{bed}=\left[(MC_p)_{ref}+M_a(C_{p,a}+qC_{p,l})+(MC_p)_{HX}\right]_{bed} \tag{2.22}$$

where $C_{p,l}$ represents the specific heat capacity of the adsorbed phase, which is assumed to be equivalent to that of the saturated liquid phase. The mass variation of the free refrigerant in adsorption bed is given as follows:

$$\frac{dM_{ref,bed}}{dt}=\begin{cases}\dot{m}_{LPJ,ads}-M_a\dfrac{dq}{dt} & \text{Pre-heating/Adsorption}\\ -\dot{m}_{LPJ,des}-M_a\dfrac{dq}{dt} & \text{Pre-cooling / Desorption}\end{cases} \tag{2.23}$$

Thus, the variation of the pressure in adsorption bed can be derived from the change of mass and temperature:

$$\frac{dP}{dt} = \frac{\partial P}{\partial \rho}\left[\frac{1}{V}\frac{dM_{ref,bed}}{dt} - \frac{\partial \rho}{\partial T}\frac{dT}{dt}\right] \tag{2.24}$$

In addition, in order to simplify the heat exchange between the lumped unit and the HTF, the outlet temperature of HTF for each HX can be represented as follows [88]:

$$T_{HTF,out} = T_{HX} + (T_{HTF,in} - T_{HX})\exp\left[-\frac{UA_{HX}}{(\dot{m}C_p)_{HTF}}\right] \tag{2.25}$$

The essential parameters used for the simulation of AHT system in this study are listed in Table 2.3, where the metal material of the HXs is copper. The HTF selected in this study is Therminol D-12, which has good thermal stability and low viscosity in the range of -85 to 230 ºC [89]. Because of the flow rate control under CTO mode, UA_{bed} needs to be calculated according to the variation of flow rate, as follows:

$$\frac{1}{UA_{bed}} = \frac{1}{h_{ads/des}\eta_o A_{total}} + \frac{d_o}{2A_o k_{HX}}\ln\frac{d_o}{d_i} + \frac{1}{h_{HTF}A_i} \tag{2.26}$$

$$A_i = A_o\frac{d_i}{d_o} \tag{2.27}$$

$$A_o = \frac{A_{total}}{\beta} \tag{2.28}$$

$$A_{total} = M_a(A/M) \tag{2.29}$$

$$h_{HTF} = \frac{Nu_{HTF}k_{HTF}}{d_i} \tag{2.30}$$

where the meanings and values of the parameters required for the bed finned tube heat

exchanger are displayed in Table A.1. Nu_{HTF} is obtained by the following heat transfer correlations [90,91]:

$$Nu_{HTF}=\begin{cases}4.36+5.36\times10^{-9}\,Re_{HTF}^{2.39} & Re_{HTF}<2300\\ \dfrac{(f_{HTF}/8)(Re_{HTF}-1000)Pr_{HTF}}{1.07+12.7\sqrt{f_{HTF}/8}\,(Pr_{HTF}^{\ 2/3}-1)} & Re_{HTF}\geq2300\end{cases} \tag{2.31}$$

$$f_{HTF}=\left[1.82\log_{10}(Re_{HTF})-1.64\right]^{-2} \tag{2.32}$$

Table 2.3 Essential parameters for simulation of AHT system [84,89].

Parameter	Value
M_a (kg)	47
$C_{p,a}$ (kJ/(kg·K))	0.9
Q_{st} (kJ/kg)	2800
$(MC_p)_{HX,bed}$ (kJ)	27.69
$(MC_p)_{eva,ini}$ (kJ)	251.16 + 15.44
$(MC_p)_{con,ini}$ (kJ)	167.44 + 15.44
UA_{eva} (kW/K)	14
UA_{con} (kW/K)	10
$\dot{m}_{HTF,des}$ (kg/s)	2
$\dot{m}_{HTF,eva}$ (kg/s)	2
$\dot{m}_{HTF,con}$ (kg/s)	2
$C_{p,HTF}$ (kJ/(kg·K))	2.5
L_p (m)	0.4
$D_{p,ads}$ (mm)	10~20 (14) [a]

$D_{p,des}$ (mm)	30
T_L (°C)	0~30 (25) [a]
T_M (°C)	60~90 (80) [a]
ΔT (°C)	20~40 (40) [a]

a: The content in the parentheses represents the reference condition.

2.3.4 System performance

The AHT system extracts the heat from the waste heat and releases the high-temperature useful heat through the adsorption process. The parameters available for evaluating system performance include specific heating power (SHP), useful adsorption heat ratio (UAHR), coefficient of performance (COP) and exergy efficiency (η_{ex}), which are defined as follows:

$$\mathrm{SHP}=\frac{\int_0^{t_{cycle}}\left[\dot{m}C_p(T_{in}-T_{out})\right]_{ads,HTF}\,dt}{M_a t_{cycle}} \tag{2.33}$$

$$\mathrm{UAHR}=\frac{\int_0^{t_{cycle}}\left[\dot{m}C_p(T_{in}-T_{out})\right]_{ads,HTF}\,dt}{\int_0^{t_{cycle}}M_a(dq/dt)_{ads}Q_{st}dt} \tag{2.34}$$

$$\mathrm{COP}=\frac{\bar{Q}_{out}}{\bar{Q}_{in}} \tag{2.35}$$

$$\eta_{ex}=\frac{\bar{E}_{out}}{\bar{E}_{in}} \tag{2.36}$$

where $\bar{Q}_{in}$, $\bar{Q}_{out}$, $\bar{E}_{in}$ and $\bar{E}_{out}$ stand for the average input thermal power, average

output thermal power, average input exergy and average output exergy, which are computed by:

$$\bar{Q}_{in}=\frac{\int_0^{t_{cycle}}\left\{\left[\dot{m}C_p(T_{in}-T_{out})\right]_{des,HTF}+\left[\dot{m}C_p(T_{in}-T_{out})\right]_{eva,HTF}\right\}dt}{t_{cycle}} \tag{2.37}$$

$$\bar{Q}_{out}=\frac{\int_0^{t_{cycle}}\left[\dot{m}C_p(T_{in}-T_{out})\right]_{ads,HTF}dt}{t_{cycle}} \tag{2.38}$$

$$\bar{E}_{in}=\frac{\int_0^{t_{cycle}}\left\{\left[\dot{m}C_p(T_{in}-T_{out})\right]_{des,HTF}(1-T_{amb}/T_{bed,des})+\left[\dot{m}C_p(T_{in}-T_{out})\right]_{eva,HTF}(1-T_{amb}/T_{eva})\right\}dt}{t_{cycle}} \tag{2.39}$$

$$\bar{E}_{out}=\frac{\int_0^{t_{cycle}}\left[\dot{m}C_p(T_{in}-T_{out})\right]_{ads,HTF}(1-T_{amb}/T_{bed,ads})dt}{t_{cycle}} \tag{2.40}$$

It is noteworthy that the cycle used to compute system performance should be in dynamic equilibrium, namely, equilibrium cycle. In this study, the attainment of equilibrium is determined through the energy balance of cycle, which can be expressed as:

$$\frac{\int_0^{t_{cycle}}\left\{\left[\dot{m}C_p(T_{in}-T_{out})\right]_{ads,HTF}+\left[\dot{m}C_p(T_{in}-T_{out})\right]_{con,HTF}\right\}dt}{\int_0^{t_{cycle}}\left\{\left[\dot{m}C_p(T_{in}-T_{out})\right]_{des,HTF}+\left[\dot{m}C_p(T_{in}-T_{out})\right]_{eva,HTF}\right\}dt}<0.01 \tag{2.41}$$

The logic flow chart of dynamic simulation of dual-bed AHT system under the CTO mode is shown in Fig. 2.2. For comparison, CTO and CFO differ only in the judgement condition for transitioning from the adsorption/desorption to the next stage. Under the CTO, the condition is that the HTF flow rate of bed during the adsorption

stage is less than 0.1 kg/s with weak availability of output heat, while under the CFO, the condition is that the HTF outlet temperature of bed during the adsorption stage is less than T_H. The bed in the desorption stage simultaneously changes to the next stage. Since the desorption time is longer than the adsorption time under the same conditions, there is no need to regulate the desorption process, but to improve the rate as much as possible from the operating conditions. Moreover, the state parameters of refrigerant in the simulation process are accessed from REFPROP 10.0 in real time.

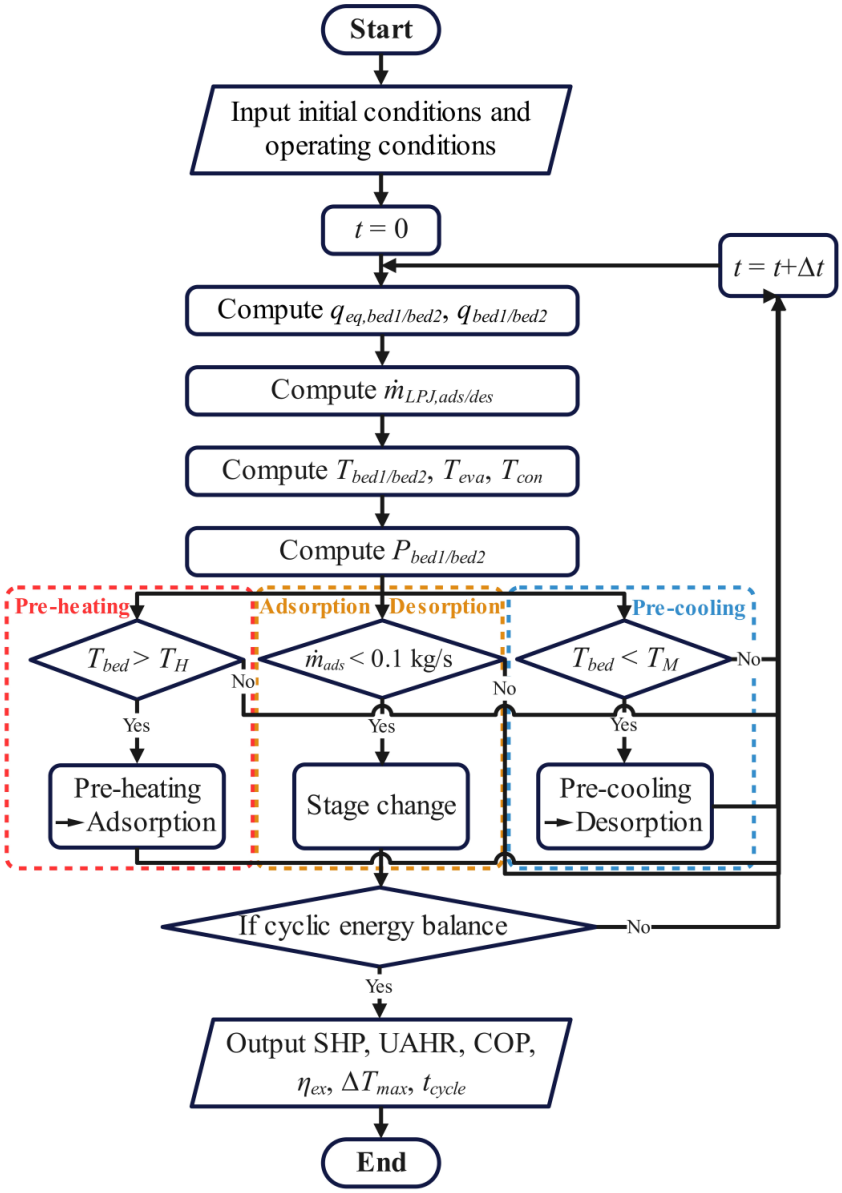

Fig. 2.2 Logic flow chart of dynamic simulation of dual-bed AHT system under CTO mode.

2.4 Results and discussion

2.4.1 Validation

Unlike the adsorption refrigeration/heat pump system, the AHT system experiences significant pressure variation within the adsorption bed during the adsorption and desorption, deeply influencing the processes. Therefore, the accurate prediction of the adsorption process is crucial for the dynamic cyclic simulation of the entire system. To validate the rationality and accuracy of the models of this study, the experimental results [79] of adsorption heating process driven by LPJ are compared with the simulation results under the same conditions, as shown in Fig. 2.3. Slightly differing from the operation of regular AHT system, the adsorption bed begins to transfer heat with the HTF from the beginning of adsorption. Over time, the pressure within the bed first rapidly increases, then stabilizes. Due to the diverse changes between the mass transfer driven by LPJ and the adsorption uptake as pressure varies, the process experiences a slight pressure drop before rising to a stable level. The temperature also rapidly increases, reaches a peak, and then gradually decreases. Besides, the temperature variation in the simulation closely matches the experimental results, while the maximum relative error in pressure prediction is 4.53%, which may be attributed to the uncertainty of measurement data and the simplification in the LDF model. Overall, the simulation results show a consistent trend with the experimental results, and the errors are within a reasonable range, thus validating the rationality and accuracy of the models.

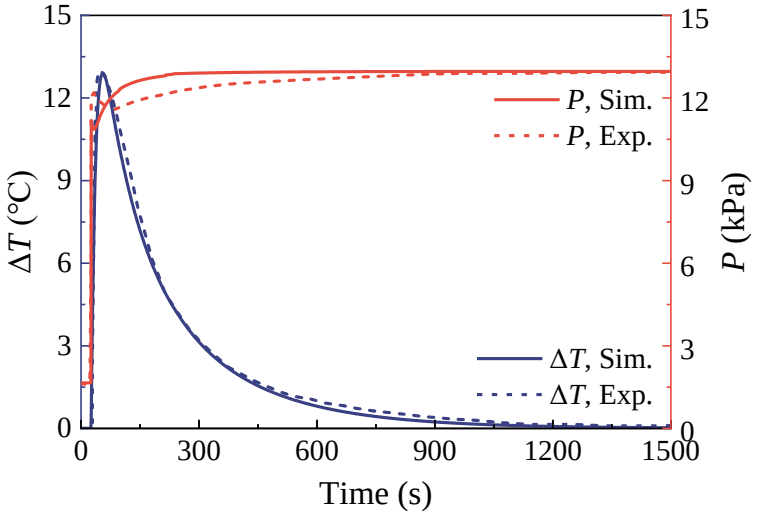

Fig. 2.3 Comparison of simulated results by models and experimental results by Tokarev et al. [79] for adsorption process driven by LPJ.

2.4.2 Maximum temperature lift potential

Through the adsorption driven by LPJ, the AHT system elevates waste heat to a higher level. There exists a theoretical limit of temperature lift within the AHT system, known as the maximum temperature lift potential [92]. This potential determines the highest level of useful heat that the adsorbent can produce under specific operating conditions. In this study, the maximum temperature lift potential is defined as the maximum temperature lift that the adsorption bed could reach, assuming it continuously remains in the pre-heating stage without heat exchange with the environment. Since the target temperature lift must be set below this value, the maximum temperature lift potential dictates the selection of adsorbent material and operating conditions in system design. Fig. 2.4 shows the trend of the maximum temperature lift potential and the time required to achieve it as a function of ambient temperature and waste heat temperature. As T_M (waste heat temperature) increases, the

maximum temperature lift potential increases, and the time required decreases. This is because an increase in T_M raises the evaporation pressure, which lowers the initial uptake and improves the final uptake, thereby enhancing the net uptake. The increased pressure differential of water vapor also accelerates the pressure lift. When T_M exceeds 70 °C, T_L (ambient temperature) has virtually no impact. Below 70 °C, as T_L increases, the maximum temperature lift potential significantly decreases, and the time shortens. This is because T_M determines the initial temperature, while T_L determines the initial pressure, and the adsorption isotherm of AQSOA-Z05/water includes a low-pressure region where the uptake is nearly zero, the extent of which depends on the temperature. When T_M is below 70 °C, in the T_L range of 0-30 °C, the initial state point exists out of the low-pressure region, causing significant change in the initial uptake with variation in T_L.

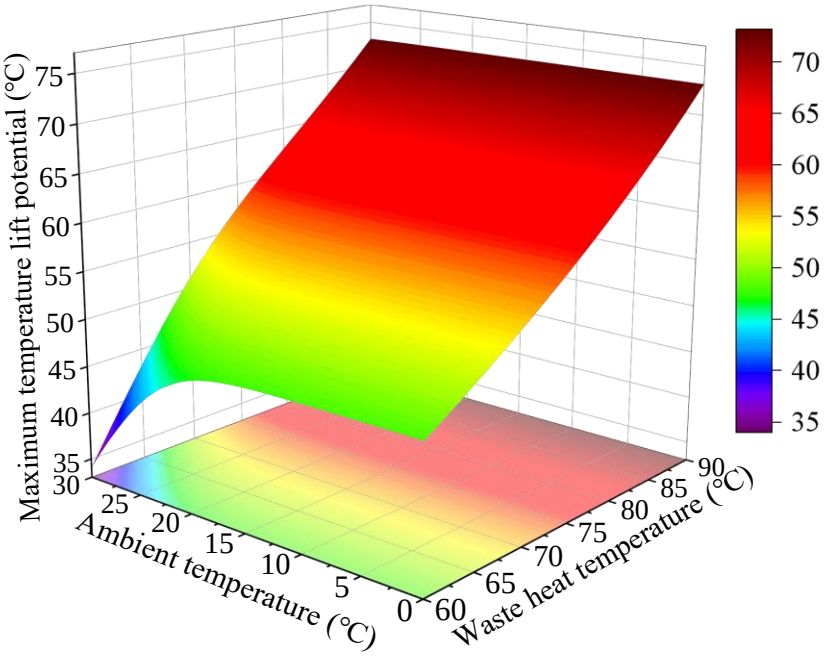

(a)

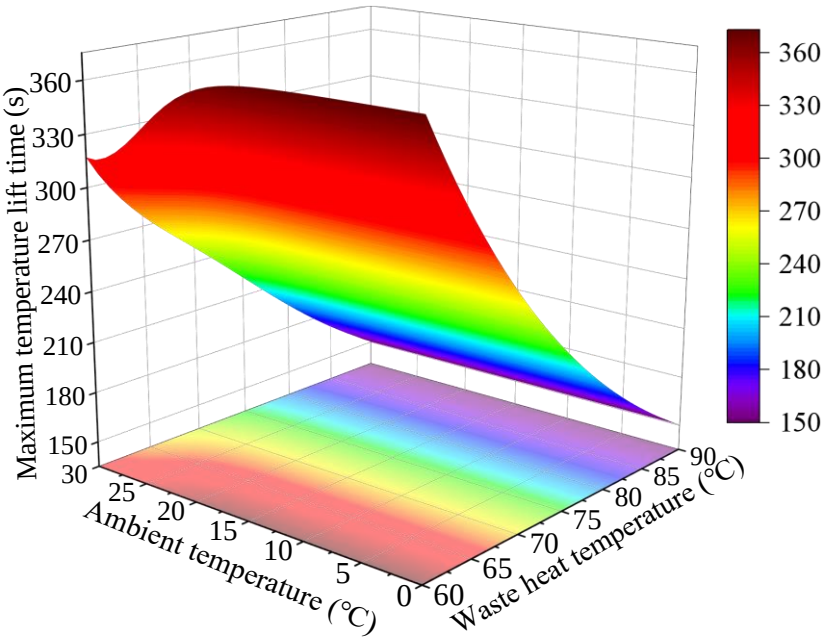

(b)

Fig. 2.4 3D surface plots of (a) maximum temperature lift potential and (b) maximum temperature lift time with ambient temperature and waste heat temperature.

In modeling, it can be known that the diameter of the connecting pipe between the high-pressure HX and low-pressure HX has a significant impact on the mass transfer driven by the LPJ, subsequently affecting the rate of the adsorption process. Fig. 3.5 displays the variation of maximum temperature lift potential and maximum temperature lift time with respect to the diameter of the adsorption connecting pipe (from evaporator to bed) under reference conditions (T_L = 25 ºC and T_M = 80 ºC). It is observable that while the pipe diameter does not impact the maximum temperature lift potential, it does influence the time required to achieve it. As the pipe diameter increases, the maximum temperature lift time gradually decreases, due to the accelerated mass transfer rate into the adsorption bed and the faster rate of pressure

lift, thus hastening the adsorption process. It can be inferred that in the AHT system, an increase of pipe diameter also helps to accelerate the production and output of high-level useful heat. This inference will be analyzed in detail later.

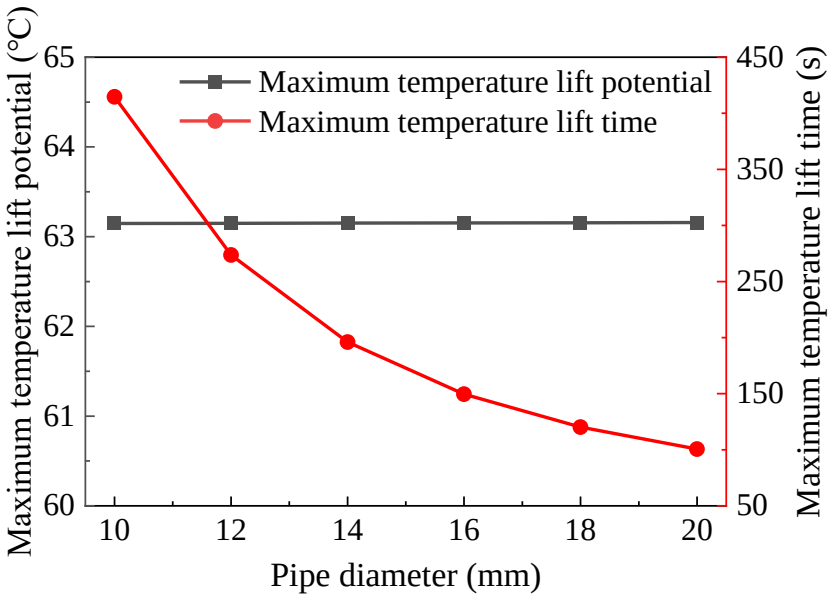

Fig. 2.5 Variation of maximum temperature lift potential and maximum temperature lift time with diameter of adsorption connecting pipe.

2.4.3 Comparison of different heat output modes

In pursuit of enhancing the performance and applicability of the AHT system in practical applications, this study presents two heat output modes, CFO and CTO, and compares them from the perspective of cycle. Fig. 2.6, 2.7 and 2.8 compare the cyclic variations of the temperature and pressure of HXs, and the adsorption uptake in adsorption beds under the reference conditions (T_L = 25 °C, T_M = 80 °C, and ΔT = 40 °C) for both modes. It should be noted that initially, the two beds are at points of

maximum and minimum equilibrium uptake, as shown in Fig. A.1. For a clear demonstration of the heat exchange effect, the HTF outlet temperature of each HX is selected as the comparative temperature. It is evident, as shown in Fig. 2.6 (a), that under the CFO mode, the output temperature of adsorption bed continues to rise after reaching the target temperature and then decreases, with the temperature in the equilibrium cycle peaking at 128 ºC. Conversely, as depicted in Fig. 2.6 (b), under the CTO mode, the output temperature of adsorption bed remains stable during the adsorption stage due to controlled HTF mass flow rate. The CTO mode provides a constant temperature heat output that is more conveniently utilized in practical projects requiring different specific temperatures, such as district heating and carbon capture. During the adsorption stage, as illustrated in Fig. 2.7 (a), the rate of pressure lift inside the beds under CFO mode gradually slows down. In contrast, as shown in Fig. 2.7 (b), the pressure inside the beds under CTO mode rises almost linearly over time, influenced by the stable temperature within the beds. Notably, the pressure inside the beds under CTO mode can almost reach the evaporation pressure during the adsorption stage, suggesting a more thorough adsorption process. Fig. 2.8 reveals that the cyclic net adsorption uptake in the CTO mode is greater than in the CFO mode. This is attributed to the higher equilibrium adsorption uptake at lower adsorption temperature, which consequently enhances kinetic adsorption.

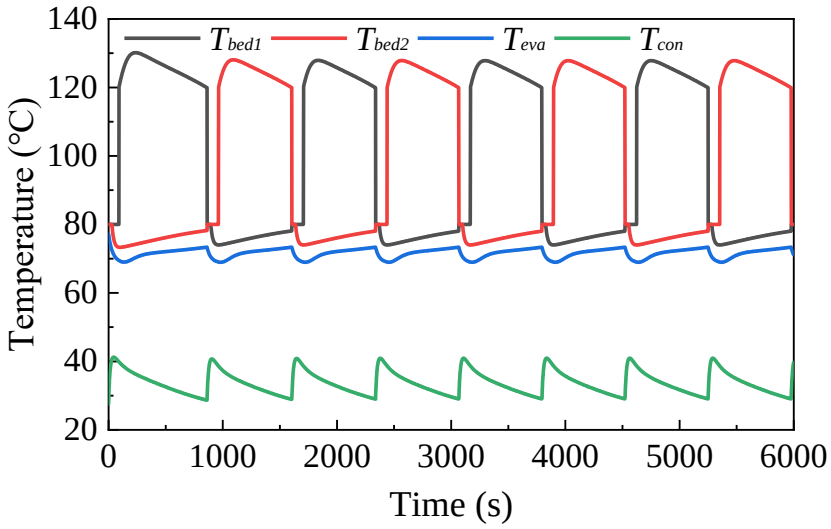

(a)

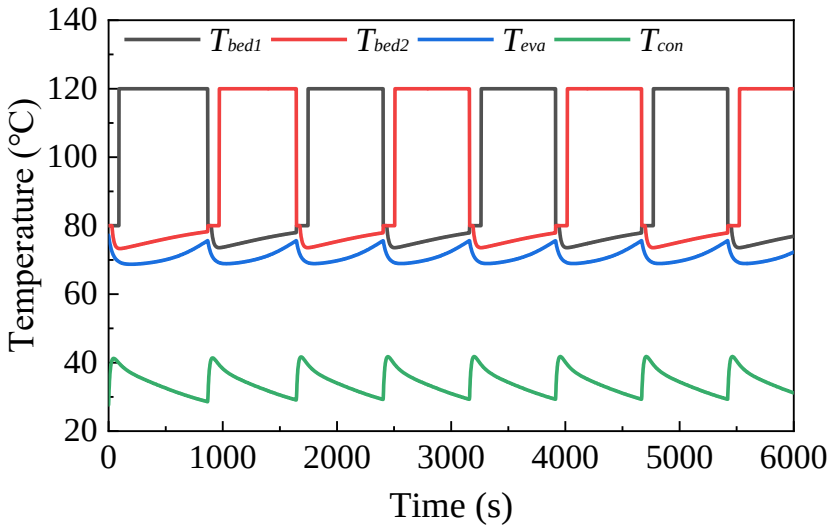

(b)

Fig. 2.6 Variation of HTF outlet temperature of bed 1, bed 2, evaporator and condenser over time under modes of (a) CFO and (b) CTO.

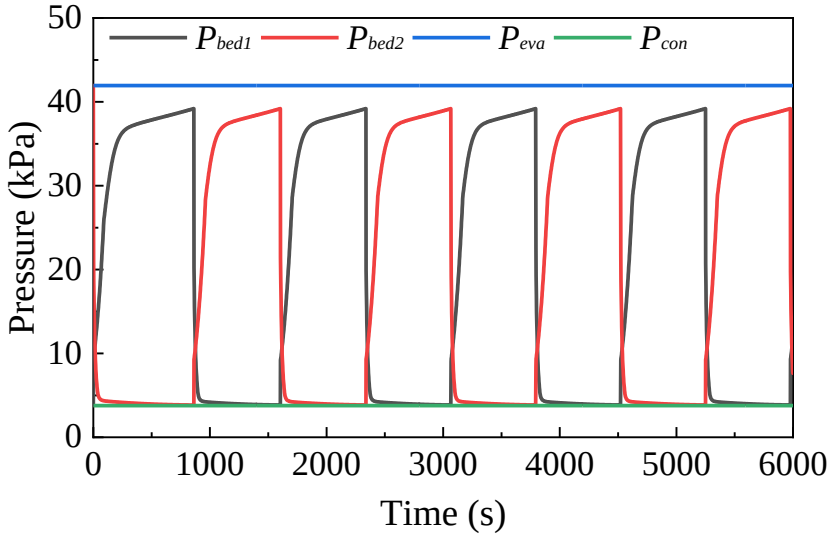

(a)

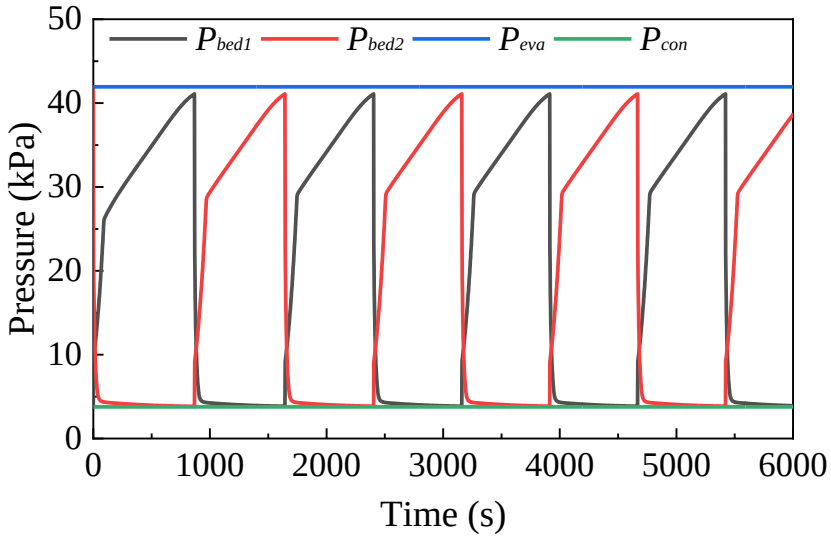

(b)

Fig. 2.7 Variation of pressure in bed 1, bed 2, evaporator and condenser over time under modes of (a) CFO and (b) CTO.

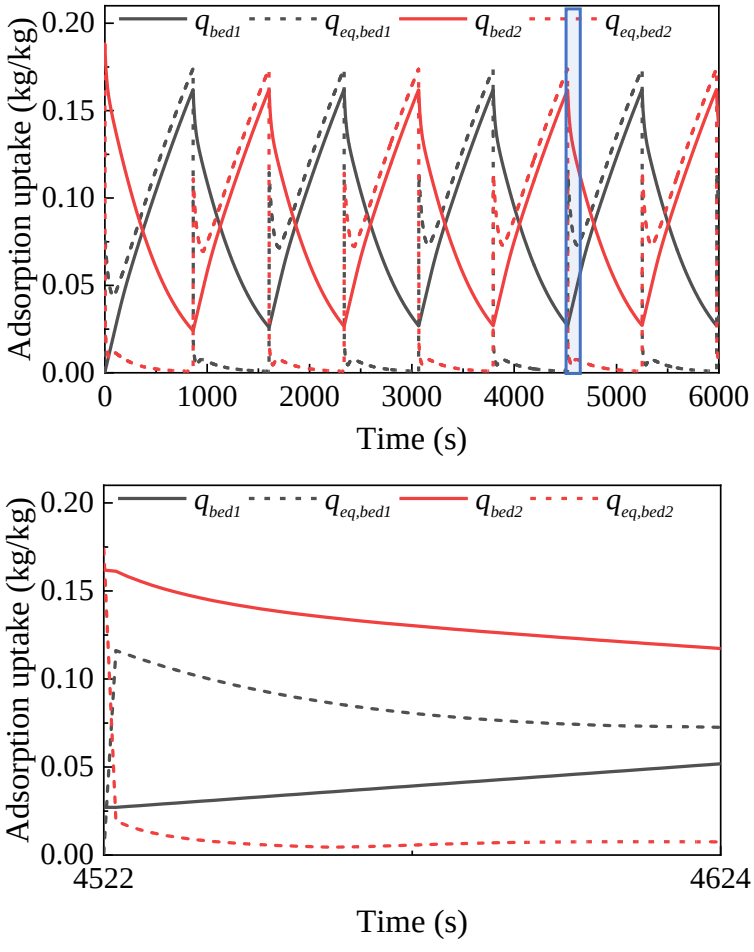
q_{bed1}
$q_{eq,bed1}$
q_{bed2}
$q_{eq,bed2}$
Adsorption uptake (kg/kg)
0.00
0.05
0.10
0.15
0.20
0
1000
2000
3000
4000
5000
6000
Time (s)
4522
4624

(a)

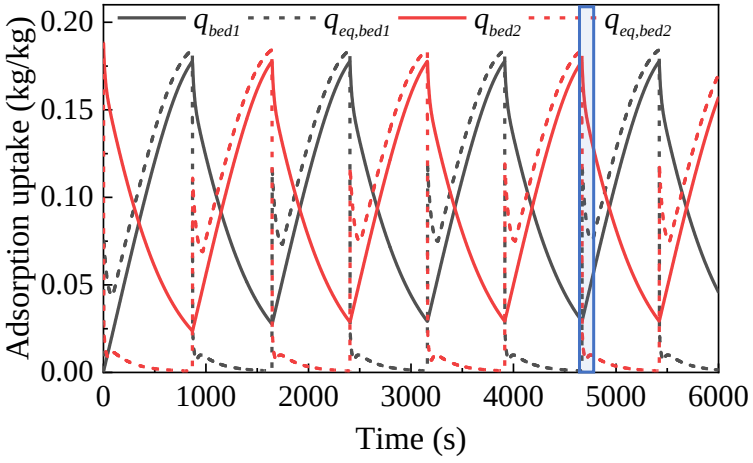
q_{bed1}
$q_{eq,bed1}$
q_{bed2}
$q_{eq,bed2}$
Adsorption uptake (kg/kg)
0.00
0.05
0.10
0.15
0.20
0
1000
2000
3000
4000
5000
6000
Time (s)

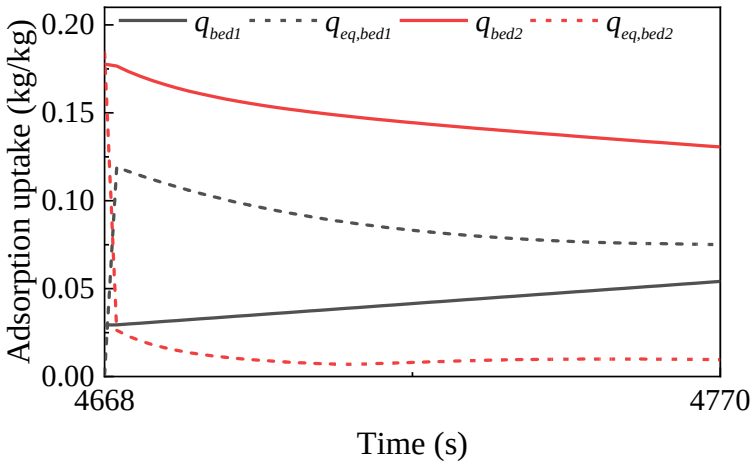

(b)

Fig. 2.8 Variation of adsorption uptake in bed 1 and bed 2 over time under modes of (a) CFO and (b) CTO.

Fig. 2.9 compares the AHT cycles in dynamic simulation under CFO and CTO modes with the ideal cycle on a pressure-temperature diagram. AHT cycle utilize the adsorption heat of adsorbate to change the temperature of adsorption bed, thus the external heat exchange is unnecessary during the pre-heating and pre-cooling stages. Theoretically, an ideal equilibrium cycle comprises two adiabatic processes for pre-heating and pre-cooling, and two isothermal processes for adsorption and desorption. As the adsorption kinetics are not considered, it is assumed that each point is at adsorption equilibrium. Differing from the ideal cycle, under the drive of LPJ, the pressure in adsorption bed in the dynamic simulation responds first, followed by significant temperature increase or decrease. To accelerate the desorption stage, the temperature control through flow regulation is not required. Instead, it is expedited by enlarging the diameter of desorption connecting pipe and increasing the HTF flow rate to complete desorption as quickly as possible in the adsorption bed. During the

adsorption stage, under CFO mode, the real-time adjustment of HTF flow is not necessary. However, due to the attenuation of performance, its HTF flow rate is also limited, which will be explained in detail later. Under CTO mode, due to the regulation of HTF flow, the temperature of adsorption bed remains stable, achieving the isothermal heat release' process during the adsorption stage in the ideal cycle. Moreover, apart from the initial states, the maximum and minimum equilibrium adsorption uptake are hardly reached in the subsequent cycles.

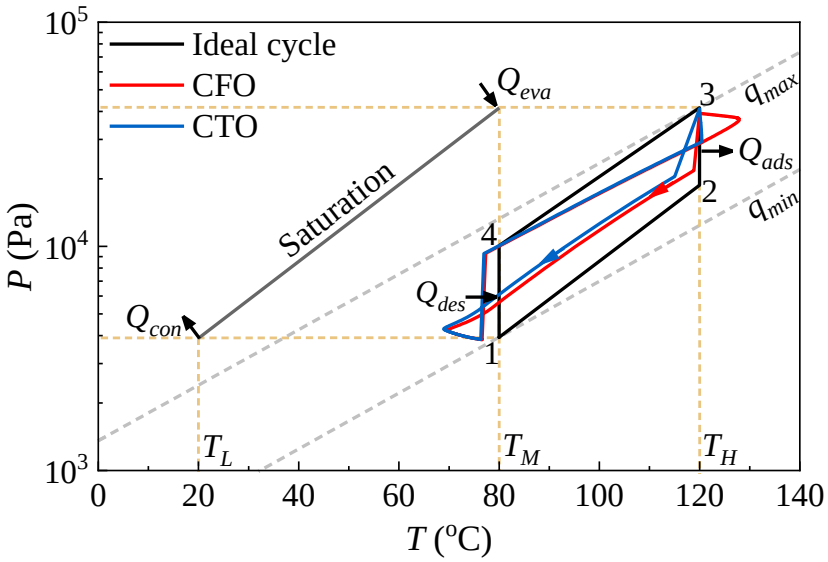

Fig. 2.9 Comparison of AHT cycles in dynamic simulation under CFO and CTO modes with ideal cycle.

Through the regulation for HTF flow of adsorption bed, the CTO mode achieves constant temperature heat output. Fig. 2.10 illustrates the variation of HTF mass flow rate in adsorption beds under CTO mode in dynamic simulation. During the pre-heating and pre-cooling stages, there is no heat exchange with the HTF, and the mass flow rate is 0 kg/s. In the desorption stage, to accelerate the process, a higher HTF flow

rate is employed to enhance the heat exchange with the adsorption bed. During the adsorption stage, under the control of CTO mode, to match the heat exchange demand for constant temperature output, the HTF flow rate spikes first, and then gradually decreases to 0.1 kg/s. As can be seen, during the period from 4700 to 5500 s, the peak of mass flow rate reaches 0.31 kg/s. The magnitude of this value reflects the intensity of the adsorption. In practical engineering applications, the control systems can be used to continuously compute temperature deviation and automatically adjust pump speed, thereby achieving the constant HTF outlet temperature.

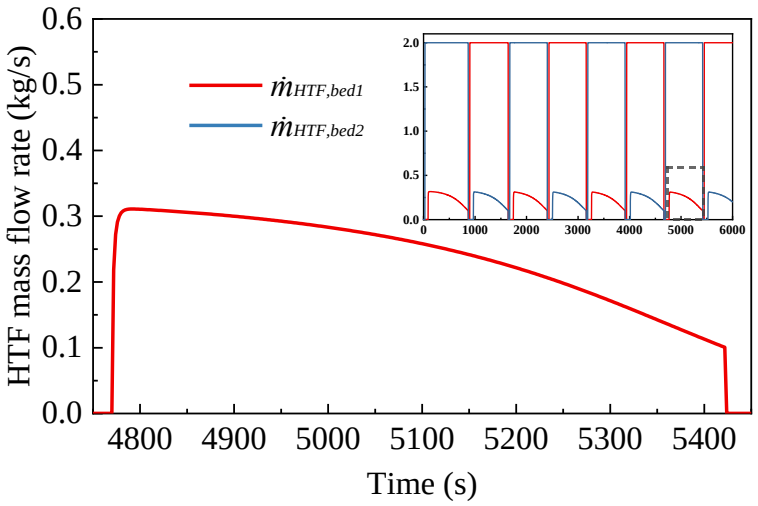

Fig. 2.10 Variation of HTF mass flow rate of adsorption beds over time under CTO mode.

The preceding results provided the comparative analyses of parameter variations in CFO and CTO modes in dynamic simulation; next, we will conduct an in-depth analysis of system performance parameters of equilibrium cycle. Fig. 2.11 compares

the impact of HTF mass flow rate of adsorption bed under CFO mode on different system performance parameters, alongside a direct comparison to those computed under CTO mode. These important performance parameters include SHP, UAHR, COP, exergy efficiency, cycle maximum temperature lift and cycle time.

In the CFO mode, as the HTF mass flow rate increases, there is a noticeable reduction in UAHR, COP and exergy efficiency, and the reductions becoming progressively more substantial as the flow increases. This trend suggests that smaller HTF flow rate are more beneficial for enhancing the energy conservation of the system. While SHP, which is a critical indicator of energy productivity, initially increases, reaching a peak at 0.25 kg/s, and then undergoes a sharp decline, indicating that the flow rate of 0.3 kg/s may nearly reach the practical upper limit under CFO mode, thus lacking in practical application value. Additionally, both the cycle maximum temperature lift and the cycle time exhibit decreasing trends as the HTF flow rate increases, due to the larger thermal capacity per unit time of HTF, effectively moderating the temperature fluctuation within adsorption bed. Moreover, when comparing CFO and CTO, it becomes evident that aside from the advantage of more stable heat output that facilitates easier utilization, CTO mode also shows a higher SHP, meaning more heat output per unit time. And the UAHR, COP and exergy efficiency closely approach the corresponding maximum values achievable under CFO mode.

Therefore, CTO mode demonstrates superior applicability and system performance, establishing itself as a more advanced mode of heat output. Incorporating advanced control technologies in practical design and applications could further elevate system performance by enhancing response speed and operational flexibility.

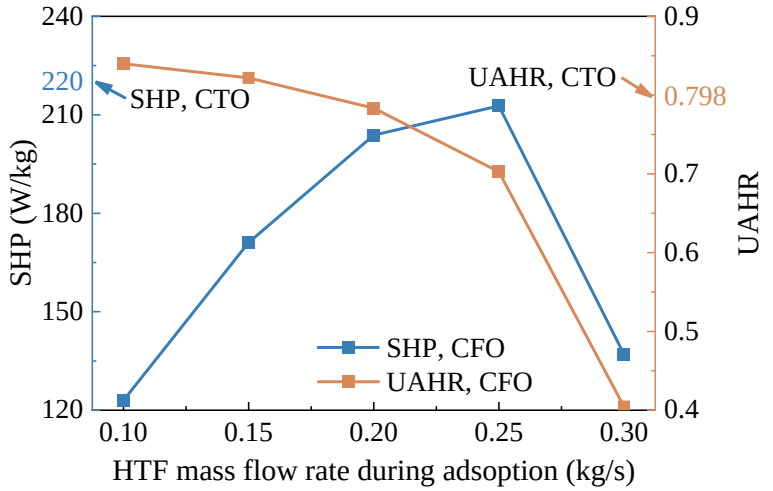
240
220
210
180
150
120
0.9
0.798
0.7
0.6
0.5
0.4
SHP (W/kg)
UAHR
SHP, CTO
UAHR, CTO
SHP, CFO
UAHR, CFO
0.10
0.15
0.20
0.25
0.30
HTF mass flow rate during adsoption (kg/s)

(a)

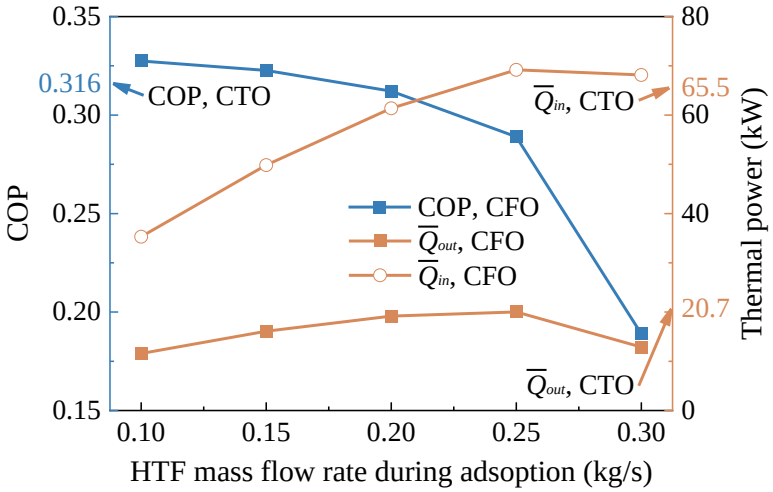
0.35
0.316
0.30
0.25
0.20
0.15
80
65.5
60
40
20.7
0
COP
Thermal power (kW)
COP, CTO
$\overline{Q}_{in}$, CTO
COP, CFO
$\overline{Q}_{out}$, CFO
$\overline{Q}_{in}$, CFO
$\overline{Q}_{out}$, CTO
0.10
0.15
0.20
0.25
0.30
HTF mass flow rate during adsoption (kg/s)

(b)

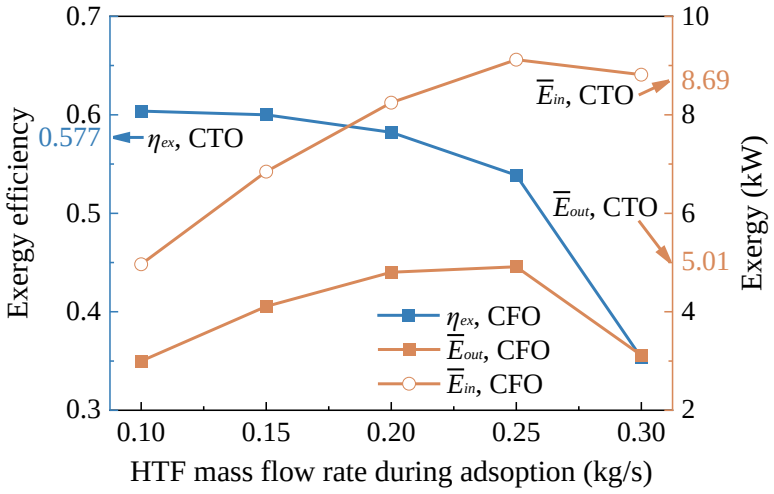

(c)

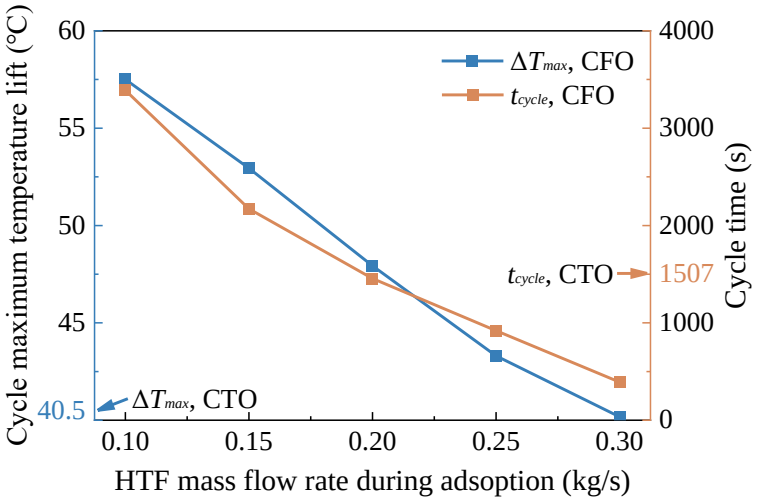

(d)

Fig. 2.11 System performance parameters versus HTF mass flow rate of beds during adsorption phase under CFO mode compared to CTO mode: (a) SHP and UAHR, (b) COP, (c) exergy efficiency, (d) cycle maximum temperature lift and cycle time.

2.4.4 Influence of different parameters under CTO mode

While investigating the dual-bed AHT system under CTO mode, various

condition parameters significantly influence its performance. This study further analyzes the influence of the diameter of adsorption connecting pipe, target temperature lift, ambient temperature, and waste heat temperature on different performance parameters. The objective is to deeply understand the underlying mechanisms and provide reliable suggestions for the design of AHT system.

Fig. 2.12 illustrates the impact of the length-to-diameter ratio of adsorption connecting pipe on various performance parameters of AHT system under CTO mode. In this study, we investigated the effect of length-diameter ratio by changing the diameter. As the diameter increases, both SHP and exergy efficiency rise, although the rate of increase gradually diminishes. The size of pipe diameter is positively correlated with the mass transfer rate driven by LPJ, further influencing the rate of adsorption and the generation of adsorption heat. Both UAHR and COP increase with the diameter, reaching their peak values of 0.822 and 0.322 respectively at a diameter of 12 mm, before beginning to decline. With the diameter smaller than 12 mm, due to the reduced adsorption rate leading to lower heat release, the corresponding HTF mass flow rate required to match the constant temperature heat output also decreases, approaching the minimal limit of 0.1 kg/s. When the mass flow rate is below this limit, the output heat is considered non-utilizable, resulting in a significant portion of adsorption heat not being released before the adsorption stage ends, thereby causing waste of adsorption heat. Consequently, the UAHR and COP for a pipe diameter of 10 mm are lower than for that of 12 mm. Notably, increasing the pipe diameter results in higher average input and output thermal powers. however, the relative increase in input thermal power is greater, associated with enhanced heat exchange of the evaporator. Moreover, the CTO mode maintains the stability of HTF outlet temperature during the adsorption stage,

while a slight increase in the cycle maximum temperature lift is still unavoidable. In application, considering SHP and COP, two performance metrics with engineering significance, choosing a diameter of 14-16 mm for the adsorption connecting pipe may be appropriate.

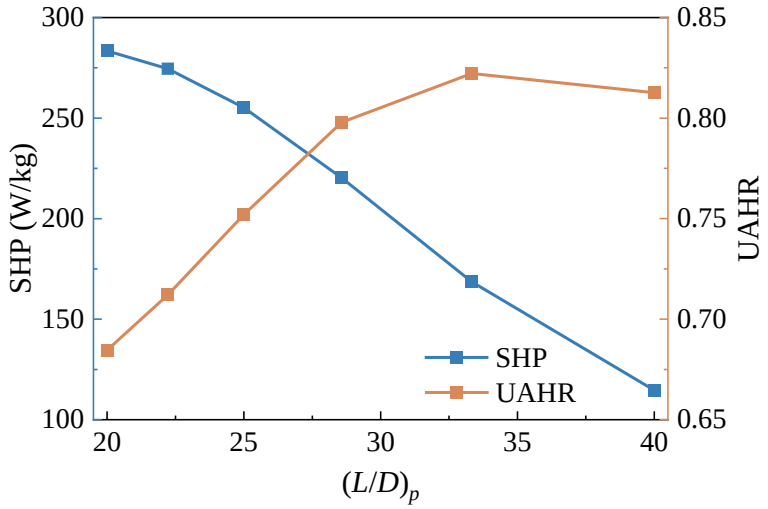

(a)

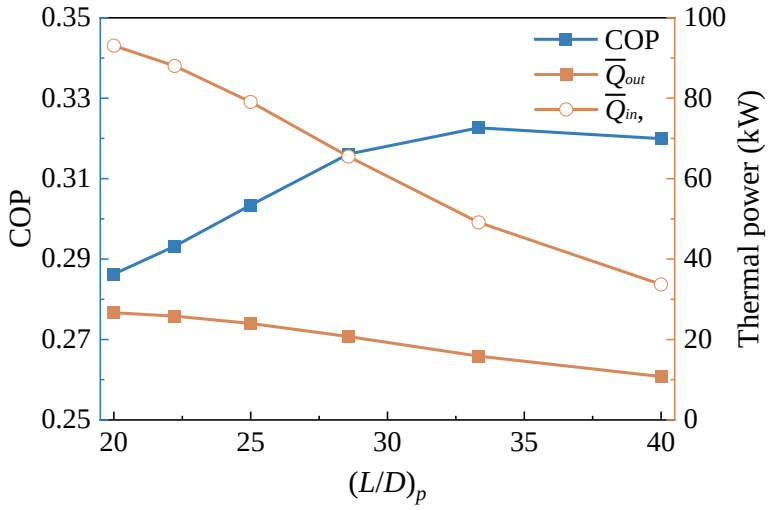

(b)

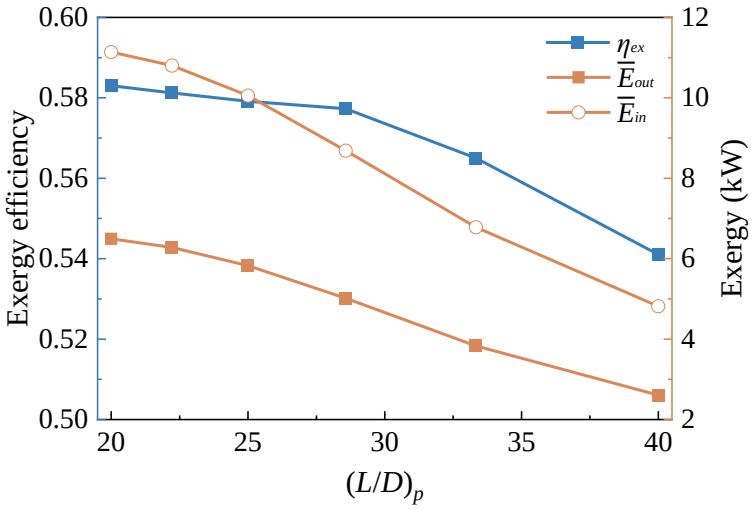

(c)

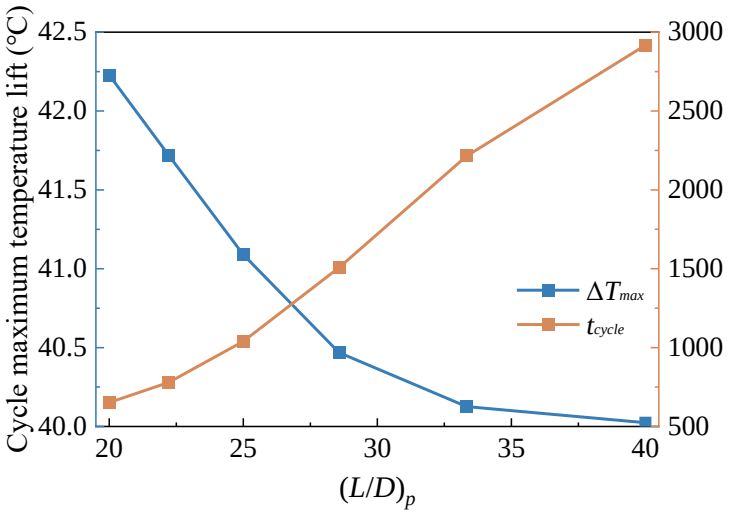

(d)

Fig. 2.12 System performance parameters versus diameter of adsorption connecting pipe under CTO mode: (a) SHP and UAHR, (b) COP, (c) exergy efficiency, (d) cycle maximum temperature lift and cycle time.

As mentioned in 2.4.2, by analyzing the maximum temperature lift potential from a theoretical perspective, the limit of temperature lift in adsorption bed starting from the minimum uptake point was explored. In the equilibrium cycle of AHT system, due

to the limitation of system performance, the target temperature lift should be below the maximum temperature lift potential. Fig. 2.13 shows the trends of COP and SHP with the variation in target temperature lift under the reference conditions (T_L = 25 °C and T_M = 80 °C). As the target temperature lift increases, both COP and SHP decrease, with the rate of decrease becoming more pronounced. At a temperature lift of 55 °C, both COP and SHP decay to the levels of no utilitarian value, at 0.048 and 26 W/kg, respectively. Based on the declining trend, it can be inferred that the target temperature lift where the performance parameters reach zero is between 55 °C and 60 °C, which is less than the maximum temperature lift potential of 63.15 °C under the same conditions. Therefore, in selecting the target temperature lift, it is crucial to consider whether the performance parameters meet the requirements of applications.

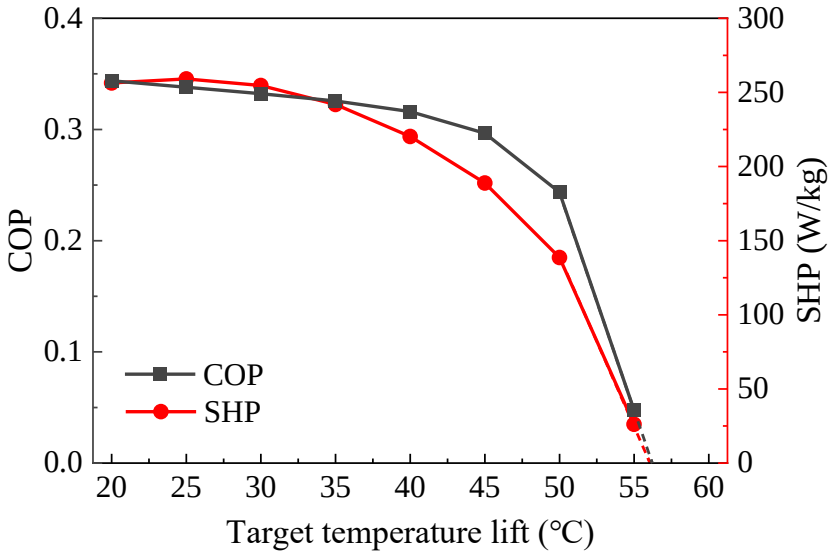

Fig. 2.13 COP and SHP versus target temperature lift under CTO mode.

Fig. 2.14 illustrates the trends of SHP, UAHR, COP and exergy efficiency as a

function of ambient temperature under different target temperature lifts, with the waste heat temperature of 80 ºC. Initially, as T_L increases, the SHP and UAHR remain nearly stable, and the COP slightly rises. However, all the three performance parameters begin to significantly decline once T_L exceeds 25 ºC. In the AHT system, T_L determines the evaporation pressure, thus setting the initial pressure for the adsorption process. As seen in Fig. A.1, the minimum equilibrium uptake point, i.e., the initial adsorption point, is situated just at the boundary of the low-pressure region of the 80 ºC isotherm (the uptake is approximately 0 kg/kg). When T_L exceeds 25 ºC, the minimum uptake noticeably increases, leading to the reduction in the net uptake of cycle, and consequently, a decline in system performance happens. Additionally, the exergy efficiency significantly increases as TL rises. In terms of equilibrium thermodynamics, the relationship between exergy efficiency and COP can be derived as follows:

$$\begin{aligned}\eta_{ex} &= \mathrm{COP}\frac{1-T_L/T_H}{1-T_L/T_M} \\ &= \mathrm{COP}\frac{T_M}{T_H}\left(1+\frac{T_H-T_M}{T_M-T_L}\right)\end{aligned} \tag{2.42}$$

Obviously, given that the COP remains relatively stable, Eq. (2.42) provides a reasonable explanation for the increase in exergy efficiency with T_L rising. Therefore, within an ambient temperature range of 0-30 ºC, analogous to climates like those of Shanghai and Fukuoka [21], this dual-bed AHT system can operate fairly stably.

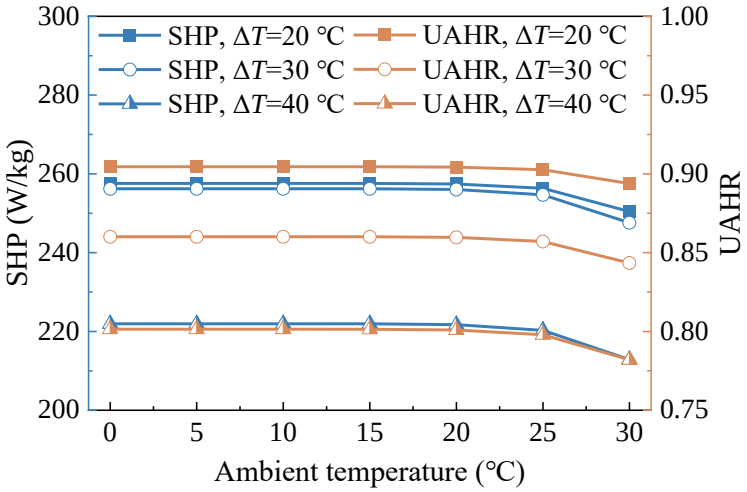
SHP, ΔT=20 ℃
SHP, ΔT=30 ℃
SHP, ΔT=40 ℃
UAHR, ΔT=20 ℃
UAHR, ΔT=30 ℃
UAHR, ΔT=40 ℃
SHP (W/kg)
UAHR
Ambient temperature (℃)
300
280
260
240
220
200
1.00
0.95
0.90
0.85
0.80
0.75
0
5
10
15
20
25
30

(a)

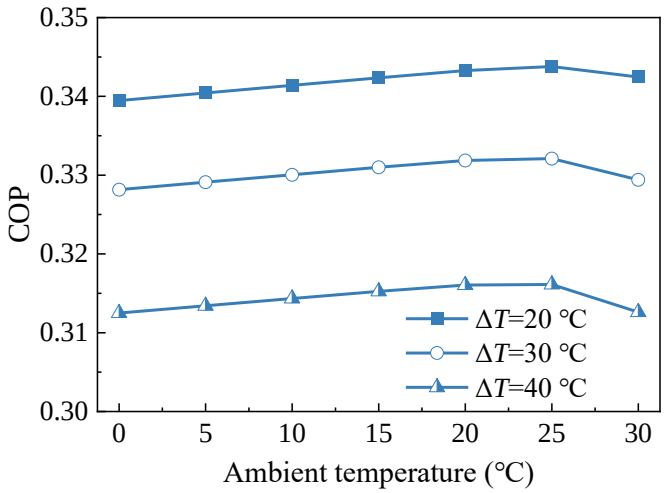
COP
Ambient temperature (℃)
ΔT=20 ℃
ΔT=30 ℃
ΔT=40 ℃
0.35
0.34
0.33
0.32
0.31
0.30
0
5
10
15
20
25
30

(b)

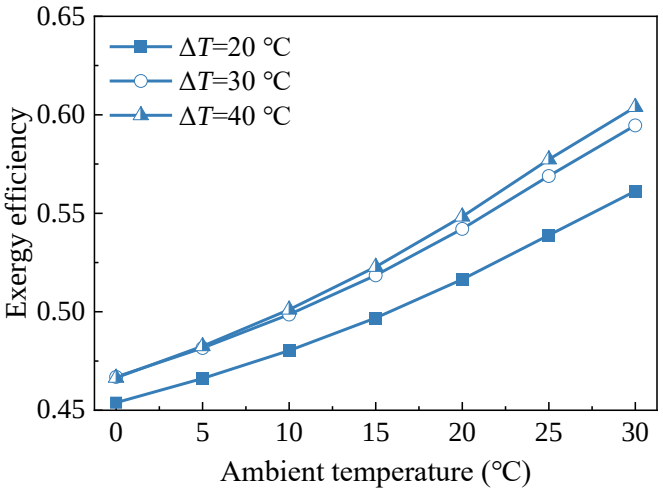

(c)

Fig. 2.14 System performance parameters versus ambient temperature under CTO mode: (a) SHP and UAHR, (b) COP, (c) exergy efficiency.

Fig. 2.15 illustrates the trends of SHP, UAHR, COP and exergy efficiency with waste heat temperature under different target temperature lifts, with the ambient temperature of 25 ºC. It is noteworthy that a target temperature lift of 40 ºC is unachievable at a T_M of 60 ºC and is therefore not considered in the results. As T_M increases, SHP significantly rises, while UAHR, COP and exergy efficiency initially increase sharply, and then gradually stabilize after 70 ºC. In the AHT system, T_M primarily dictates the initial adsorption temperature. As shown in Fig. A.1, at the same pressure of the minimum equilibrium uptake point, the initial uptakes at 60 ºC and above 80 ºC are distinctly different. The latter is in the low-pressure region, while the former is far removed with a considerably larger initial uptake over 0, leading to the reduction in the net uptake of cycle. This also explains why the system performance deteriorates significantly when T_M is below 70 ºC, and the greater the target

temperature lift, the more severe the performance deterioration. Therefore, considering an appropriate range of waste heat temperature used is crucial in the design of AHT system.

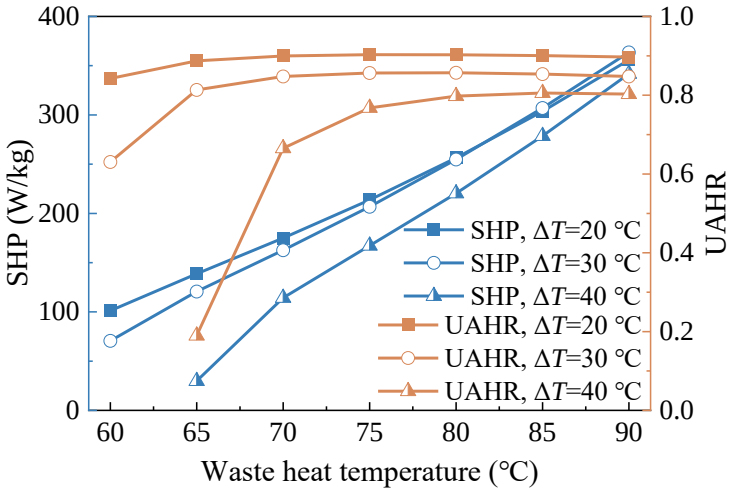

(a)

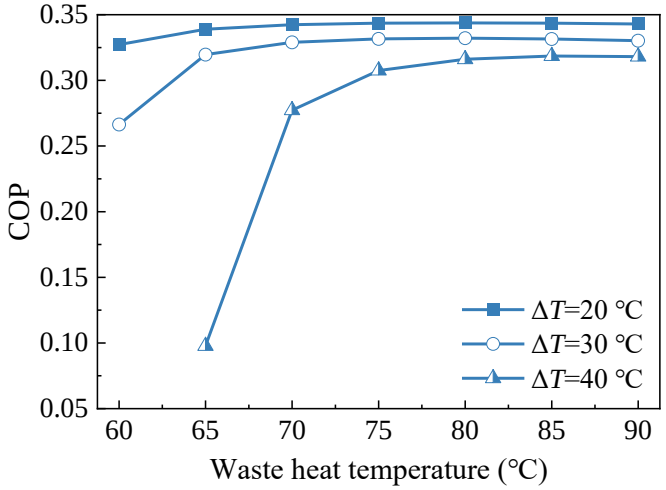

(b)

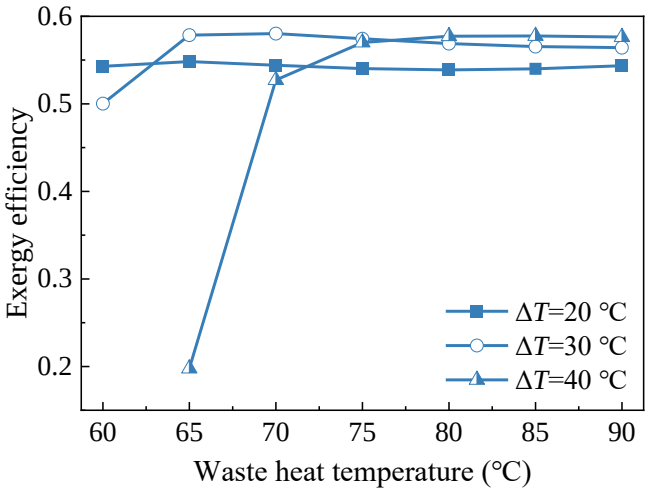

(c)

Fig. 2.15 System performance parameters versus waste heat temperature under CTO mode: (a) SHP and UAHR, (b) COP, (c) exergy efficiency.

Under CTO mode, the AHT system can achieve constant temperature heat output, meeting the thermal demands at different temperatures. However, due to the variation in HTF flow rate, it is difficult to directly apply it to the applications with specific heat load requirements. In practical engineering projects, it is recommended to add a heat storage tank after the AHT system, which allows excess heat to be stored during the period of high flow rate and released when needed [93]. Consequently, while maintaining constant temperature, a relatively constant flow rate output is also maintained, effectively mitigating the fluctuation of heat output caused by the adjustment of flow rate. Additionally, a monitoring and control system should be utilized for better stability of heat output. Apart from a real-time control of HTF flow rate, it is necessary to compute and predict the average output flow rate of the cycle to ensure that it matches the heat load demands of various applications.

2.5 Conclusions

A comprehensive dynamic performance analysis of an AQSOA-Z05/water based dual-bed adsorption heat transformer (AHT) system driven by large pressure jump (LPJ) for low-grade waste heat upgrade was conducted under two heat output modes: constant flow output (CFO) and constant temperature output (CTO). Besides, the maximum temperature lift potential, a crucial factor governing adsorbent material selection and operating conditions, was thoroughly investigated. Key conclusions are as follows:

1. An increase in waste heat temperature enhances the maximum temperature lift potential while reducing the required time. The ambient temperature exhibits a notable impact only at lower waste heat grade. The adsorption process driven by LPJ can be accelerated through enlarging the diameter of adsorption connecting pipe.

2. Under CFO mode, the SHP peaks at a HTF flow rate of 0.25 kg/s during adsorption before declining sharply, indicating the limitations in practical applications. In contrast, the CTO mode demonstrates superior applicability by enabling stable, controllable temperature output, which is utilizable across various applications. Moreover, it achieves higher SHP and the other performance parameters close to the corresponding maximums under CFO mode.

3. Under CTO mode, an increase in diameter of adsorption connecting pipe improves the SHP and exergy efficiency, while the UAHR and COP drop from 12 mm. Considering the practical engineering significance of SHP and COP, 14-16 mm is recommended. The target temperature lift requires judicious selection below the

maximum potential to ensure satisfactory performance. An ambient temperature range of 0-30 ^{o}C facilitates stable operation, whereas the waste heat temperature below 70 ^{o}C leads to significant deterioration in performance.

4. To bridge the CTO mode's variable flow output and heat load demands, incorporating a heat storage tank after the AHT system is recommended in practical engineering. This configuration enables storing excess heat during high flow and releasing it as needed, mitigating the fluctuation of output thermal power while maintaining constant temperature. A monitoring and control system is needed for real-time flow regulation and calculating and predicting cyclic average output flow rate, ensuring compatibility with the requirements of applications.

Overall, the findings regarding the characteristics of AHT system during dynamic operation, as well as the suggestions proposed for design and optimization, provide valuable reference for waste heat recovery and upgrade in various industrial fields, which is conducive to improving energy utilization efficiency and promoting sustainable development.

Chapter 3 Scaling and sensitivity analyses of open adsorption process for atmospheric CO_2 capture

3.1 Introduction

Of all the steps in open adsorption cycle, the adsorption process is the most important part, which determines the upper limit of the performance of adsorption system and deserves further analysis. Currently, most of the scaling analysis focuses on the close adsorption of single component such as water vapor or ethanol, while the scaling analysis for the adsorption of multi-component mixtures is noticeably rare in the literature, especially for the adsorption of CO_2 from a gas mixture. In previous researches on CO_2 capture, the comprehensive performance of adsorption cycles has been a central focus [23 – 25]. Most published works lack the detailed analysis on the scaling of the transfer mechanisms and their sensitivities for an open adsorption process to capture CO_2. By analyzing relevant governing equations and determining crucial scale parameters, scaling analysis can provide a valuable framework for understanding the mechanisms of open adsorption process and designing efficient CO_2 capture systems.

In this chapter, based on systems description, we conduct scaling and sensitivity analyses of the open adsorption process for capturing CO_2 from the simulated flue gas (CO_2/N_2) using zeolite 13X-APG. The mechanisms of heat and mass transfer in the

coupled fluid-solid interaction during different stages are discussed via comparing the results of scaling analysis and CFD simulation. Furthermore, a detailed sensitivity analysis is conducted to determine the critical input parameters that influencing the performance scale parameters. By adopting scaling analysis to compare the terms within the governing equations describing open CO_2 adsorption process, the primary factors impacting fluid flow and heat and mass transfer are identified, thereby making a deeper elucidation of the mechanisms of the behaviors. Additionally, the research results not only accurately predict the characteristics of the open adsorption process but also lead to a substantial reduction in computational costs.

3.2 Modeling

3.2.1 Physical model

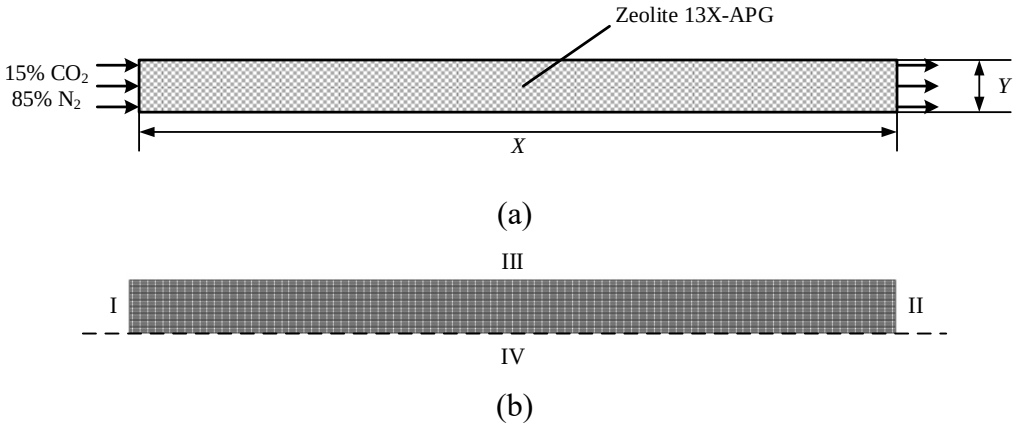

Fig. 3.1 Schematic diagrams of (a) geometric model and (b) meshing and boundary conditions (I velocity inlet; II pressure outlet; III wall; IV symmetry).

During the open CO_2 adsorption process in this study, a gas mixture containing

15% CO_2 and 85% N_2 enters the adsorption bed from the inlet, and the unadsorbed gas (mostly N_2) flows out. CO_2 is selectively adsorbed by the adsorbent during the process. Additionally, a small amount of N_2 is also adsorbed, but its adsorption time is much shorter compared to CO_2. For the simulation, a 2D geometric model is adopted as shown in Fig. 3.1 (a). The adsorption domain is considered as a rectangular region with a length of X and a width of Y. The meshing and boundary conditions are displayed in Fig. 3.1 (b). Referring to Fig. 3.1 (b), the inlet, I, is set as the velocity inlet with a fixed velocity value. The outlet, II, is set as the pressure outlet with a fixed pressure value, which is the standard atmospheric pressure for the adsorption process. The wall, III, is simplified as a constant temperature wall since the adsorption bed is usually placed in an air or water bath. To reduce the computation cost, the chain line, IV, is set as the axis of symmetry for the entire domain. In addition, it is assumed that the adsorption bed is filled with inert gas at normal temperature and pressure at the initial condition.

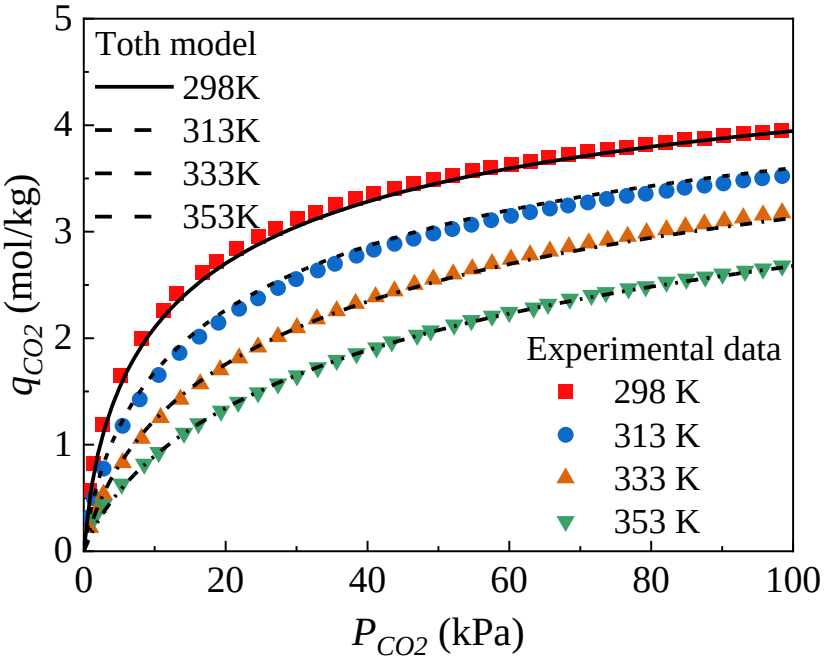

(a)

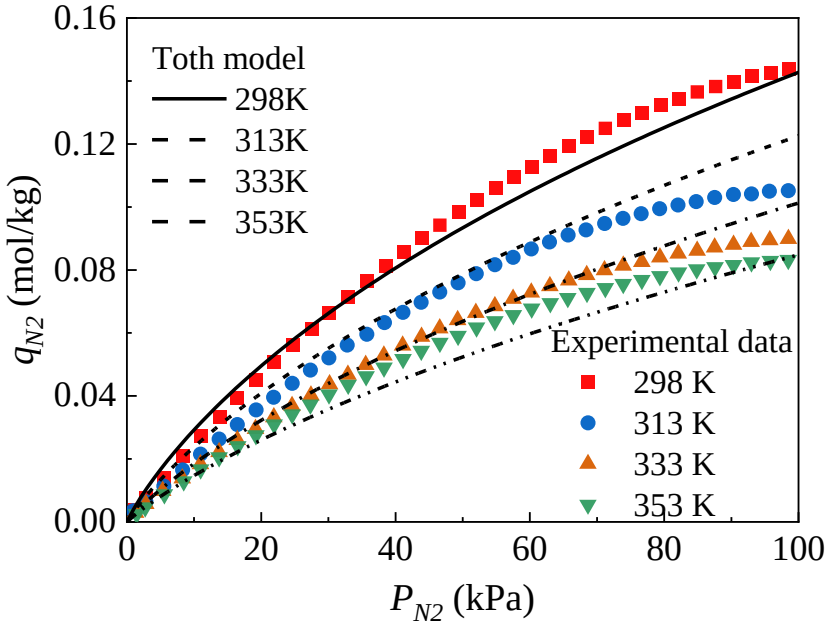

(b)

Fig. 3.2 Adsorption isotherms of zeolite 13X-APG at different temperatures for (a) CO_2 and (b) N_2 [65].

The adsorbent utilized in the study, zeolite 13X-APG, is typically applied to separate H_2O and CO_2 from gas mixtures. The alkali aluminosilicate adsorbent generally takes the form of spherical particles. Before the adsorption process, the adsorbents are often dried to remove H_2O and other impurities and activated for at least 12 hours at higher than 600 K [28]. Compared with other materials, the adsorbent material has a larger adsorption capacity of CO_2, whose CO_2 and N_2 adsorption isotherms from 0~100 kPa are shown in Fig. 3.2 [13]. It can be clearly seen that zeolite 13X-APG has a high adsorption selectivity for CO_2. Furthermore, zeolite 13X-APG exhibits good thermal and chemical stabilities, which are favorable for maintaining its adsorption performance at higher temperatures, making it a highly promising material for CO_2 capture. Existing research [29] has demonstrated that water vapor tends to

occupy adsorption sites within zeolite 13X, thereby reducing the CO_2 adsorption capacity. Additionally, water vapor may also affect the structure of zeolite [30]. Thus, water vapor in flue gas is considered removed before the CO_2 capture. It is assumed that the adsorbate is the binary mixture of N_2 and CO_2, rather than the wet air.

3.2.2 Mathematical models

The conservation equations of mass, momentum and energy are employed as mathematical models to explain and describe the transport phenomena in the adsorption process.

3.2.2.1 Model assumptions

To reasonably simplify the mathematical models for the open CO_2 adsorption process, the following assumptions are made:

(1) The CO_2/N_2 gas mixture is an ideal gas with no water vapor, and the fluid flow is laminar.

(2) The superficial velocity is adopted to model the flow in porous media [94,95].

(3) A homogeneous pore size distribution is considered, while the gas distribution is also uniform throughout.

(4) The adsorbent and adsorbate are assumed to be in thermal equilibrium.

(5) The adsorbed phase volume is considered negligible. The specific heat capacity of adsorbed phase is included to that of adsorbent [96]. Otherwise, the other physical properties of adsorbent are kept constant.

3.2.2.2 Mass equation

The mass balance to describe the mass variation of gas mixture can be expressed as follows:

$$\frac{\partial(\varepsilon\rho)}{\partial t}+\mathrm{div}(\rho\vec{v})=-(1-\varepsilon)\rho_s\sum_i M_i\frac{\partial q_i}{\partial t} \tag{3.1}$$

where i refers to the component of gas mixture (CO_2/N_2). $\partial q_i/\partial t$ is the adsorption rate, which represents adsorption kinetics and can be defined by the LDF model [97] as:

$$\frac{\partial q_i}{\partial t}=k_{L,i}\left(q_i^*-q_i\right) \tag{3.2}$$

where q_i is the actual adsorption uptake. $k_{L,i}$ is the adsorption time constant, which is calculated from the film, micro-porous and macro-porous resistance [98]. The relevant models and parameters for $k_{L,i}$ is displayed in Appendix B. q_i^* is the equilibrium adsorption uptake at the given operating condition. For zeolite 13X-APG, the equilibrium adsorption uptake can be calculated by the Toth model [99]:

$$q_i^*=\frac{q_{m,i}K_{eq,i}P_i}{\left(1+\left(K_{eq,i}P_i\right)^{n_i}\right)^{\left(\frac{1}{n_i}\right)}} \tag{3.3}$$

where $q_{m,i}$ is the maximum capacity of adsorption uptake and n_i is the heterogeneity constant. $K_{eq,i}$ is the equilibrium adsorption constant, which can be calculated according to the Vant Hoff equation:

$$K_{eq,i}=K_{0,i}\mathrm{e}^{-\left(\frac{\Delta H_i}{RT}\right)} \tag{3.4}$$

where $K_{0,i}$ is the adsorption constant at infinite dilution and ΔH_i is the molar adsorption heat. The related parameters of zeolite 13X-APG for the Toth model are listed in Table 3.1. Compared with the experimental data in Fig. 3.2, the Toth model for CO_2

adsorption illustrates a good accuracy.

In addition, the mass transfer model for each component of gas mixture is as follows:

$$\frac{\partial(\varepsilon\rho Y_i)}{\partial t} + \mathrm{div}(\rho\vec{v}Y_i) = \mathrm{div}(\varepsilon\rho D_{disp,i}\mathrm{grad}Y_i) - (1-\varepsilon)\rho_s M_i \frac{\partial q_i}{\partial t} \quad (3.5)$$

where Y_i is the mass fraction of component i and $D_{disp,i}$ is the mass dispersion coefficient [100].

Table 3.1 Equilibrium adsorption parameters of zeolite 13X-APG for Toth model [65].

	q_m (mol/kg)	n	K_0 (1/Pa)	ΔH (J/mol)
CO_2	5.445	0.5506	5.33e-9	-26050
N_2	1.014	0.4376	2.26e-8	-13360

3.2.2.3 Momentum equation

In porous medium, the momentum equation is expressed as follows:

$$\frac{\partial(\rho\vec{v}/\varepsilon)}{\partial t} + \mathrm{div}(\rho\vec{v}\vec{v}/\varepsilon^2) = -\mathrm{grad}P + \mathrm{div}(\vec{\tau}) - \left[A\frac{(1-\varepsilon)^2\mu}{\varepsilon^3 d_p^2}\vec{v} + B\frac{1-\varepsilon}{\varepsilon^3 d_p}\rho|\vec{v}|\vec{v} \right] \quad (3.6)$$

where τ is the stress tensor, and d_p is the particle diameter of adsorption material. Based on the superficial velocity, the momentum source term can be obtained by the Ergun equation [101,102], which takes into account both the viscous and inertial resistances. The empirical factors A and B are 150 and 1.75, respectively.

3.2.2.4 Energy equation

Based on the model assumptions, the thermal equilibrium model is adopted for the energy equation. Thus, the energy variation of the solid and porous fluid zones can be governed by one equation:

$$\frac{\partial\left(\varepsilon\rho E+(1-\varepsilon)\rho_s E_s\right)}{\partial t}+\operatorname{div}\left(\vec{v}(\rho E+P)\right)$$
$$=\operatorname{div}\left[k_{eff}\operatorname{grad}T-\sum_i h_i\vec{J}_i+\tau\vec{v}\right]+(1-\varepsilon)\rho_s\sum_i-\Delta H_i\frac{\partial q_i}{\partial t} \tag{3.7}$$

where E and E_s are the total energy for the fluid and solid, respectively. h_i and J_i are the sensible enthalpy and the diffusion flux of component, i. k_{eff} is the effective thermal conductivity, which is defined as the volume-weighted average of the fluid and solid thermal conductivities:

$$k_{eff}=\varepsilon k+(1-\varepsilon)k_s \tag{3.8}$$

The simulation of this process is realized by compiling the user defined function (UDF) for the source terms and other related parameters into the CFD software, Ansys Fluent [103].

3.3 Scaling analysis

Scaling analysis can provide appropriate simplification of research problem by transforming it into a certain scale and ignoring insignificant effects to obtain a simpler model that describes the macroscopic phenomena. By utilizing known parameters and conducting scaling analysis for entire adsorption domain, some meaningful

characteristic results can be obtained for open adsorption process.

3.3.1 Open adsorption process

3.3.1.1 Process analysis

In this section, the entire process will be analyzed in detail by dividing into different phases. The detailed parameters of the adsorption bed and adsorption material are listed in Table 3.2. Previous studies have indicated that the length-to-diameter ratio of the adsorption bed should be adopted between 4-40 based on the adsorbent characteristics, system stability, and economics [75,104–106]. Therefore, a length of X=0.15 m and a width of Y=0.01 m (length-to-diameter ratio of 7.5) are employed for the physical geometry model.

Throughout the process, it is assumed that a gas mixture of 15% CO_2 and 85% N_2 is continuously supplied to the adsorption bed at a steady flow rate. Due to the small N_2 uptake, N_2 is adsorbed throughout the bed for only a short time, releasing a small amount of adsorption heat. The adsorption process of CO_2 is relatively slow from the inlet to the entire bed, releasing a large amount of adsorption heat during this process, resulting in a significant temperature rise. From a macroscopic scale, the CO_2 adsorption process can be divided into two phases.

The first phase is the feeding phase, as shown in Fig. 3.3 (a). Instead of adsorbing adsorbates almost uniformly in the space as a closed adsorption bed [78], an open adsorption bed reaches the equilibrium uptake sequentially from the inlet to the outlet over time. Thus, the entire adsorption bed can be divided into the CO_2 adsorption region and the CO_2 non-adsorption region. CO_2 fluid keeps on flowing forward towards the outlet only when the local CO_2 actual uptake almost reaches the

equilibrium. Therefore, the CO_2 adsorption region is filled with CO_2 and N_2, while the CO_2 non-adsorption region contains almost only N_2. There exists a transition region between two regions where the actual uptake is between 0 and the equilibrium uptake. Considering the efficiency of CO_2 adsorption, the velocity of the supplied gas in the open adsorption bed should be slow [107], and the local adsorption is mainly influenced by CO_2 concentration rather than adsorption time constant. Consequently, the time scale of the feeding stage is much larger than that of the local adsorption kinetics. The length of transition region is very short and can be ignored in the scaling analysis, simplified as a transition boundary line. This boundary gradually moves towards the outlet as time progresses. Furthermore, the maximum temperature rise occurs at the transition boundary due to the fastest adsorption rate. Towards the external environment, only the heat conduction exists during this phase (mostly in the CO_2 adsorption region), while the heat convection is considered negligible. As the adsorption heat generation surpasses the heat dissipation via heat conduction, the temperature continues to rise until the CO_2 adsorption region occupies the entire adsorption bed.

The second phase is the heat-removing phase, as shown in Fig. 3.3 (b). When CO_2 is adsorbed throughout the region, the entire adsorption bed is filled with CO_2, and it begins to flow out from the outlet. A heat convection effect for removing the heat is generated by the high temperature fluid flowing out. Based on the temperature rise in the previous phase, the excess heat is removed up via both heat conduction and convection in this phase. Moreover, due to the temperature drop, the CO_2 equilibrium uptake increases, resulting in further CO_2 adsorption until the temperature restores to the ambient temperature. Therefore, the heat-removing capacity of the adsorption bed

will have a significant impact on the duration of this phase. Eventually, the gas mixture flows through the adsorption bed in a steady state.

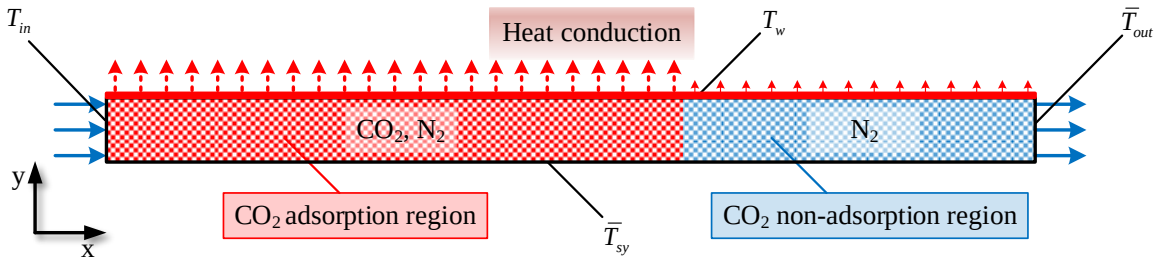

(a)

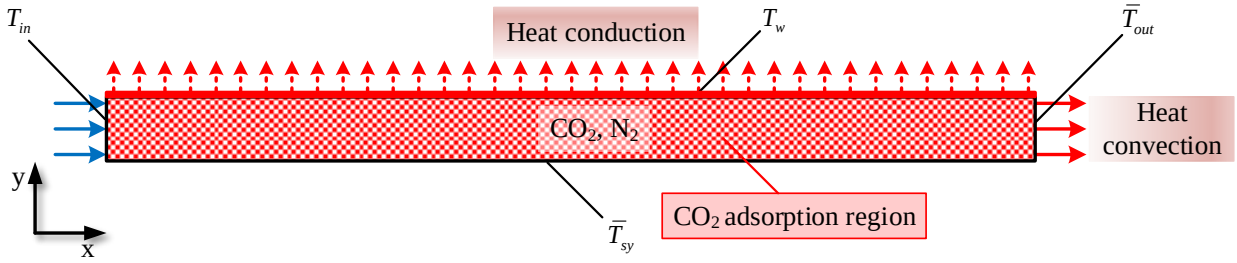

(b)

Fig. 3.3 Process schematic diagrams of open CO_2 adsorption during (a) feeding phase and (b) heat-removing phase.

Table 3.2 Parameters of adsorption bed and thermophysical properties of the adsorbent material.

Parameter	Value
X (m)	0.15
Y (m)	0.01
v_{in} (m/s)	0.05
T_{in} (K)	298

T_w (K)	298
P (Pa)	101325
ε	0.565
d_p (m)	0.001
ρ_s (kg/m^3)	1100
$C_{p,s}$ (J/(kg·K))	920
k_s (W/(m·K))	0.2

3.3.1.2 Scaling analysis assumptions

Scaling analysis obtains simple algebraic quantities from the partial differential governing equations by assuming the following:

(1) The complexity of fluid flow in the porous medium is disregarded, and the velocity of the fluid in the y direction is ignored, i.e., v_y=0.

(2) In the feeding phase, the transition region is simplified as a transition boundary line, where the temperature is maximum in the entire adsorption bed.

(3) At the end of the feeding phase, the CO_2 adsorption region occupies the entire adsorption bed, and the average temperature in the adsorption bed reaches the maximum value throughout the process. In Fig. 3.3, the temperature scales of inlet, outlet, wall, and symmetry axis are marked. For the feeding phase, the relationships between all temperature scales are simplified as follows:

$$\begin{aligned} \bar{T}_{out} &= T_{in} \\ \bar{T} &= \frac{T_w + \bar{T}_{sy}}{2} \end{aligned} \tag{3.9}$$

For the heat-removing phase, the relationships between all temperature scales are simplified as follows:

$$\bar{T} = \frac{T_{in} + \bar{T}_{out}}{2} = \frac{T_w + \bar{T}_{sy}}{2} \tag{3.10}$$

(4) Throughout the process, the influence of the temperature variation on N_2 adsorption is negligible, and its equilibrium uptake remains constant.

(5) The effect of pressure drop, mass diffusion and viscous dissipation on the energy transfer is far less than that of heat conduction and convection, which can be ignored.

3.3.2 Scaling analysis of feeding phase

3.3.2.1 Mass equation

In the mass balance, the dynamic adsorption is represented by the mass sink term. For the two-dimensional model, it has been assumed that the fluid velocity in the y direction is 0, so the mass convective term in the y direction can be ignored. Since the mass variation is mainly on the x direction and the difference of component concentration in the y direction is very small, the mass diffusive term in the y direction can also be ignored. Therefore, the mass balance for component *i* can be transformed from Eq. (3.5) to the following form:

$$\overbrace{\varepsilon \frac{\partial(\rho Y_i)}{\partial t}}^{\text{Usteady}} + \overbrace{\frac{\partial(\rho v_x Y_i)}{\partial x} + \cancel{\frac{\partial(\rho v_y Y_i)}{\partial y}}}^{\text{Convective}} = \overbrace{\varepsilon D_{disp,i} \left(\frac{\partial^2(\rho Y_i)}{\partial x^2} + \cancel{\frac{\partial^2(\rho Y_i)}{\partial y^2}} \right)}^{\text{Diffusive}} \overbrace{-(1-\varepsilon)\rho_s M_i \frac{\partial q_i}{\partial t}}^{\text{Component source}} \tag{3.11}$$

In scaling analysis, the orders of magnitude of different terms are compared at macroscopic scales, and insignificant terms are ignored to simplify the models. In the space, the length X and width Y of the geometric model of fluid domain are used as

the macroscopic scale. In the time, the duration of different phases is adopted as the macroscopic scale. Therefore, the various terms in the mass equation for each component can be derived to the macroscopic scale as follows:

$$\underbrace{\varepsilon\frac{\partial(\rho Y_i)}{\partial t}}_{\substack{\frac{\varepsilon\rho Y_i}{t_{feed,i}} \\ \Downarrow \\ \frac{\varepsilon\rho_i X_i}{t_{feed,i}}}} + \underbrace{\frac{\partial(\rho v_x Y_i)}{\partial x}}_{\substack{\frac{v_{in}\rho Y_i}{X} \\ \Downarrow \\ \frac{v_{in}\rho_i X_i}{X}}} = \underbrace{\varepsilon D_{disp,i}\frac{\partial^2(\rho Y_i)}{\partial x^2}}_{\cancel{\frac{\varepsilon D_{disp,i}\rho Y_i}{X^2}}} - \underbrace{(1-\varepsilon)\rho_s M_i\frac{\partial q_i}{\partial t}}_{\frac{(1-\varepsilon)\rho_s M_i q_{feed,i}}{t_{feed,i}}} \tag{3.12}$$

where $q_{feed,i}$ is the adsorption uptake scale for feeding phase, and X_i is the molar fraction of component i, 15% for CO_2 and 85% for N_2. Driven by forced convection, the diffusive term can be ignored by comparing the orders of magnitude of the convective term and diffusive term. The comparison is shown as follows:

$$\frac{\text{Convective}}{\text{Diffusive}} \sim \frac{\frac{v_{in}\rho Y_i}{X}}{\frac{\varepsilon D_{m,i}\rho Y_i}{X^2}} = \frac{v_{in}X}{\varepsilon D_{m,i}} \sim O(10^3) \tag{3.13}$$

For N_2 adsorption, due to its short time and the negligible influence of the temperature variation, the following relation can be derived:

$$q_{feed,N2} \sim q^*_{N2} \tag{3.14}$$

Therefore, by rearranging Eq. (3.12), the feeding time scale for N_2 adsorption can be expressed as:

$$t_{feed,N2} \sim \frac{\left((1-\varepsilon)\rho_s M_{N2} q^*_{N2} + \varepsilon\rho_{N2} X_{N2}\right)X}{v_{in}\rho_{N2} X_{N2}} \tag{3.15}$$

For CO_2 adsorption, the amount of CO_2 replenished into the fluid domain from the inlet is much less than that is adsorbed. By comparing the unsteady term and source term for CO_2 in Eq. (3.12), the following can be obtained:

$$\frac{\text{Unsteady}}{\text{CO}_2\ \text{Source}} \sim \frac{\dfrac{\varepsilon\rho_{CO2}X_{CO2}}{t_{feed,CO2}}}{\dfrac{(1-\varepsilon)\rho_s M_{CO2} q_{feed,CO2}}{t_{feed,CO2}}} = \frac{\varepsilon\rho_{CO2}X_{CO2}}{(1-\varepsilon)\rho_s M_{CO2} q_{feed,CO2}} \sim O(10^{-3}) \tag{3.16}$$

In Eq. (3.16), $q_{feed,CO2}$ is considered as the equilibrium uptake $q^*_{CO_2}$. According to Eq. (3.16), the unsteady term can be ignored. Therefore, the feeding time scale for CO_2 adsorption can be expressed as follows:

$$t_{feed,CO2} \sim \frac{(1-\varepsilon)\rho_s M_{CO2} q_{feed,CO2} X}{v_{in}\rho_{CO2}X_{CO2}} \tag{3.17}$$

3.3.2.2 Energy equation

The adsorption heat released during the open adsorption process increases the temperature in the adsorption bed. The adsorption heat generation is represented by the energy source term in the energy equation. Since the density of the fluid is much smaller than that of the solid adsorbent, the internal energy variation of the fluid in the unsteady term is negligible. In the energy diffusive term, the heat conduction effect is inversely proportional to the length of bed. Thus, the heat transfer in the x direction can be neglected. Therefore, the energy equation can be transformed into the following form:

$$\overbrace{\cancel{\varepsilon\frac{\partial(\rho C_p T)}{\partial t}} + (1-\varepsilon)\frac{\partial(\rho_s C_{p,s} T)}{\partial t}}^{\text{Usteady}} + \overbrace{\frac{\partial(v_x \rho C_p T)}{\partial x}}^{\text{Convective}} = \overbrace{k_{eff}\left(\cancel{\frac{\partial^2 T}{\partial x^2}} + \frac{\partial^2 T}{\partial y^2}\right)}^{\text{Diffusive}} + \overbrace{(1-\varepsilon)\rho_s \sum_i -\Delta H_i \frac{\partial q_i}{\partial t}}^{\text{Energy source}} \tag{3.18}$$

During the feeding phase, the temperature rise at the outlet of adsorption bed is negligible, allowing the effect of the heat convection to be disregarded. With this premise, various terms can be expressed at a macroscopic scale, as follows:

$$\underbrace{(1-\varepsilon)\frac{\partial(\rho_s C_{p,s} T)}{\partial t}}_{\frac{(1-\varepsilon)\rho_s\left(C_{p,s}^{feed}\Delta\bar{T}_{max}+\Delta C_{p,s}^{feed}T_{in}\right)}{t_{feed,CO2}}} + \cancel{\frac{\partial(v_x \rho C_p T)}{\partial x}} = \underbrace{k_{eff}\frac{\partial^2 T}{\partial y^2}}_{\substack{\frac{k_{eff}\left(\Delta T_w-\Delta\bar{T}_{sy}\right)}{2Y^2} \\ \Downarrow \\ \frac{k_{eff}\Delta\bar{T}_{max}}{Y^2}}} + \underbrace{(1-\varepsilon)\rho_s\sum_i -\Delta H_i\frac{\partial q_i}{\partial t}}_{\frac{(1-\varepsilon)\rho_s\sum_i -\Delta H_i q_{feed,i}}{t_{feed,CO2}}} \tag{3.19}$$

where ΔT represents the temperature difference between various temperature scales and the inlet temperature. $C_{p,s}^{feed}$ is the specific heat of the solid adsorbent with adsorbed CO_2 (ignoring N_2) at the end of feeding phase, which is defined as:

$$\begin{aligned} C_{p,s}^{feed} &= C_{p,s} + C_{p,CO2} M_{CO2} q_{feed,CO2} \\ \Delta C_{p,s}^{feed} &= C_{p,CO2} M_{CO2} q_{feed,CO2} \end{aligned} \tag{3.20}$$

where $q_{feed,CO2}$ will be given next.

According to Eq. (3.19), the maximum average temperature rise scale in the adsorption bed at the end of feeding phase can be expressed as:

$$\Delta\bar{T}_{max} \sim \frac{(1-\varepsilon)\rho_s Y^2\left(\sum_i -\Delta H_i q_{feed,i} - \Delta C_{p,s}^{feed} T_{in}\right)}{(1-\varepsilon)\rho_s C_{p,s}^{feed} Y^2 + k_{eff} t_{feed,CO2}} \tag{3.21}$$

At the end of the feeding phase, the entire adsorption domain has almost reached a state of equilibrium adsorption at this temperature scale. At this moment, the CO_2 adsorption uptake scale is:

$$q_{feed,CO2} \sim \frac{q_{m,CO2} P_{CO2} K_{0,CO2} e^{-\left(\frac{\Delta H_{CO2}}{R\bar{T}_{max}}\right)}}{\left(1+\left(P_{CO2} K_{0,CO2} e^{-\left(\frac{\Delta H_{CO2}}{R\bar{T}_{max}}\right)}\right)^{n_{CO2}}\right)^{\left(\frac{1}{n_{CO2}}\right)}} \tag{3.22}$$

The scales of relevant physical quantities in the feeding phase can be obtained by combining Eq. (3.14), (3.17), (3.21) and (3.22) as a system of equations, as follows:

$$\begin{cases} \Delta\bar{T}_{max} \sim \dfrac{(1-\varepsilon)\rho_s Y^2 \left(\sum_i -\Delta H_i q_{feed,i} - \Delta C_{p,s}^{feed} T_{in}\right)}{(1-\varepsilon)\rho_s C_{p,s}^{feed} Y^2 + k_{eff} t_{feed,CO2}} \\ t_{feed,CO2} \sim \dfrac{(1-\varepsilon)\rho_s M_{CO2} q_{feed,CO2} X}{v_{in} \rho_{CO2} X_{CO2}} \\ q_{feed,CO2} \sim \dfrac{q_{m,CO2} P_{CO2} K_{0,CO2} e^{-\left(\frac{\Delta H_{CO2}}{R\bar{T}_{max}}\right)}}{\left(1+\left(P_{CO2} K_{0,CO2} e^{-\left(\frac{\Delta H_{CO2}}{R\bar{T}_{max}}\right)}\right)^{n_{CO2}}\right)^{\left(\frac{1}{n_{CO2}}\right)}} \\ q_{feed,N2} \sim q_{N2}^{*} \end{cases} \tag{3.23}$$

In addition, by solving this system of equations, it can be found that $q_{feed,CO2} / q_{CO2}^{*} \sim O(10^0)$, which proves the validity of Eq. (3.16).

3.3.3 Scaling analysis of heat-removing phase

3.3.3.1 Energy equation

During the heat-removing phase, besides the heat conduction, a portion of the adsorption heat is discharged to the atmosphere with the high temperature fluid by the heat convection. Moreover, as the temperature in the adsorption bed decreases, the equilibrium adsorption uptake of CO_2 increases. While the heat in the adsorption bed is being removed, further adsorption of CO_2 happens, and this process releases the

additional heat. In this phase, the scales of various terms are transformed as follows:

$$\underbrace{(1-\varepsilon)\frac{\partial(\rho_s C_{p,s}^{*} T)}{\partial t}}_{\frac{(1-\varepsilon)\rho_s\left(\Delta C_{p,s}^{HR} T_{in} - C_{p,s}^{feed}\Delta\bar{T}_{max}\right)}{t_{HR}}} + \underbrace{\frac{\partial(v_x \rho C_p T)}{\partial x}}_{\frac{v_{in}\rho C_p \Delta\bar{T}_{out}}{2X} \Downarrow \frac{v_{in}\rho C_p \Delta\bar{T}_{max}}{X}} = \underbrace{k_{eff}\frac{\partial^2 T}{\partial y^2}}_{\frac{k_{eff}\left(\Delta T_w - \Delta\bar{T}_{sy}\right)}{2Y^2} \Downarrow \frac{k_{eff}\Delta\bar{T}_{max}}{Y^2}} + \underbrace{(1-\varepsilon)\rho_s\sum_i -\Delta H_i \frac{\partial q_i}{\partial t}}_{\frac{(1-\varepsilon)\rho_s\left(-\Delta H_{CO2} q_{HR}\right)}{t_{HR}}} \tag{3.24}$$

Where q_{HR} is the adsorption uptake in the heat-removing phase, assumed only for CO_2, which is expressed as:

$$q_{HR} = q_{CO2}^{*} - q_{feed,CO2} \tag{3.25}$$

$C_{p,s}^{HR}$ is the specific heat of the solid adsorbent with the adsorbed CO_2 at the end of heat-removing phase, which is defined as:

$$\begin{aligned} C_{p,s}^{HR} &= C_{p,s}^{feed} + C_{p,CO2} M_{CO2} q_{HR} \\ \Delta C_{p,s}^{HR} &= C_{p,CO2} M_{CO2} q_{HR} \end{aligned} \tag{3.26}$$

According to Eq. (3.24), the time scale of the heat-removing phase can be computed by the following equation:

$$t_{HR} \sim \frac{(1-\varepsilon)\rho_s X Y^2\left(-\Delta H_{CO2} q_{HR} + C_{p,s}^{feed}\Delta\bar{T}_{max} - \Delta C_{p,s}^{HR} T_{in}\right)}{\left(v_{in}\rho C_p Y^2 + k_{eff} X\right)\Delta\bar{T}_{max}} \tag{3.27}$$

Furthermore, the total time scale is obtained by summing those of feeding phase and heat-removing phase, which represent the end time of adsorption process. This is expressed as follows:

$$t_{ad} = t_{feed,CO2} + t_{HR} \tag{3.28}$$

The CO_2 removal rate is represented by the ratio of adsorbed CO_2 to supplied CO_2 at the end of adsorption [108], defined as:

$$R_{re,CO2}=\frac{(1-\varepsilon)X\rho_s q^*_{CO2}M_{CO2}}{\rho_{CO2}X_{CO2}v_{in}t_{ad}} \tag{3.29}$$

This quantity effectively represents the adsorption efficiency for CO_2 in the open adsorption process.

3.3.3.2 Momentum equation

The viscous and inertial resistances in the porous medium are used as the source terms in the momentum equation. Since v_y=0, only the momentum equation in the x direction is analyzed. Based on the above assumptions, Eq. (3.6) can be further simplified as follows:

$$\overbrace{\frac{1}{\varepsilon}\frac{\partial(\rho v_x)}{\partial t}}^{\text{Usteady}}+\overbrace{\frac{1}{\varepsilon^2}\frac{\partial(\rho v_x^2)}{\partial x}}^{\text{Inertial}}=\overbrace{-\frac{\partial P}{\partial x}}^{\text{Pressure}}+\overbrace{\frac{\mu}{\varepsilon}\frac{\partial^2 v_x}{\partial y^2}}^{\text{Viscous}}\overbrace{-A\frac{(1-\varepsilon)^2}{\varepsilon^3 d_p^2}\mu v_x}^{\text{Inertial resistance}}\overbrace{-B\frac{1-\varepsilon}{\varepsilon^3 d_p}\rho v_x^2}^{\text{Viscous resistance}} \tag{3.30}$$

Throughout the open CO_2 adsorption process, during the feeding phase, the flow pressure drop increases gradually. After reaching the adsorption equilibrium in the heat-removing phase, it tends to stabilize. For the fluid domain that reaches the adsorption equilibrium, the following scaling analysis can be conducted:

$$\cancel{\frac{1}{\varepsilon}\frac{\partial(\rho v_x)}{\partial t}}+\underbrace{\frac{1}{\varepsilon^2}\frac{\partial(\rho v_x^2)}{\partial x}}_{\cancel{\frac{\rho v_{in}^2}{\varepsilon^2 X}}}=\underbrace{-\frac{\partial P}{\partial x}}_{\frac{\Delta P_{eq}}{X}}+\underbrace{\frac{\mu}{\varepsilon}\frac{\partial^2 v_x}{\partial y^2}}_{\cancel{\frac{\mu v_{in}}{\varepsilon Y^2}}}\underbrace{-A\frac{(1-\varepsilon)^2}{\varepsilon^3 d_p^2}\mu v_x}_{\frac{A(1-\varepsilon)^2\mu v_{in}}{\varepsilon^3 d_p^2}}\underbrace{-B\frac{1-\varepsilon}{\varepsilon^3 d_p}\rho v_x^2}_{\frac{B(1-\varepsilon)\rho v_{in}^2}{\varepsilon^3 d_p}} \tag{3.31}$$

where ΔP_{eq} is the pressure drop scale from the inlet to the outlet at equilibrium

adsorption state. To explain the analysis process in detail, we evaluate the scale of each item one by one:

(1) After adsorption equilibrium, the flow can be considered to be in a quasi-steady state, so the unsteady term can be ignored.

(2) Compare the orders of magnitude of the inertial term and inertial resistance term:

$$\frac{\text{Inertial}}{\text{Inertial resistance}} \sim \frac{\frac{\rho v_{in}^2}{\varepsilon^2 X}}{\frac{B(1-\varepsilon)\rho v_{in}^2}{\varepsilon^3 d_p}} = \frac{\varepsilon d_p}{B(1-\varepsilon)X} \sim O(10^{-2}) \tag{3.32}$$

Thus, the inertial term is insignificant compared with the inertial resistance term.

(3) Compare the orders of magnitude of the viscous term and viscous resistance term:

$$\frac{\text{Viscous}}{\text{Viscous resistance}} \sim \frac{\frac{\mu v_{in}}{\varepsilon Y^2}}{\frac{A(1-\varepsilon)^2 \mu v_{in}}{\varepsilon^3 d_p^2}} = \frac{\varepsilon^2 d_p^2}{A(1-\varepsilon)^2 Y^2} \sim O(10^{-4}) \tag{3.33}$$

It is clear that the viscous term is also insignificant and can be ignored.

Therefore, by reorganizing the relationship between the scales of different terms in Eq. (3.31), the flow pressure drop scale in the bed at equilibrium adsorption can be expressed as:

$$\Delta P_{eq} \sim \left(\frac{A(1-\varepsilon)^2 \mu v_{in}}{\varepsilon^3 d_p^2} + \frac{B(1-\varepsilon)\rho v_{in}^2}{\varepsilon^3 d_p} \right) X \tag{3.34}$$

The flow pressure drop inside the adsorption bed is related to the pumping cost

[109] and should be kept as small as possible. It can be found that the pressure drop in the bed can be decreased by decreasing the gas flow velocity, increasing the porosity or increasing the particle diameter.

Table 3.3 Summary of scale parameters and their physical significance for open CO_2 adsorption process.

Parameter	Physical significance	Scaling expression
$t_{feed,N2}$	Feeding time scale for N_2 adsorption, short due to the small N_2 uptake	Eq. (3.15)
$t_{feed,CO2}$	Feeding time scale for CO_2 adsorption, also representing the time scale of feeding phase	Eq. (3.17)
$\bar{T}_{max}$	Maximum average temperature scale, occurring at the end of feeding phase	Eq. (3.21)
$q_{feed,CO2}$	CO_2 uptake scale for feeding phase, similar to the equilibrium uptake at the maximum average temperature rise scale	Eq. (3.22)
t_{HR}	Time scale of heat-removing phase, depending on the capacity of heat conduction and heat convection of adsorption bed	Eq. (3.27)
t_{ad}	Total time scale of open CO_2 adsorption process, expressed as the sum of the time scales of feeding phase and heat-removing phase	Eq. (3.28)
$R_{re,CO2}$	CO_2 removal rate, formulated as the amount ratio of adsorbed CO_2 to supplied CO_2 at the total time scale	Eq. (3.29)
ΔP_{eq}	Equilibrium pressure drop scale from inlet to outlet, reflecting the magnitude of flow resistance inside adsorption bed	Eq. (3.34)

3.4 Results and discussion

3.4.1 CFD validation

The CFD simulation is carried out for the open adsorption process for the adsorption domain illustrated in Fig. 3.1. For establishing the accuracy of the CFD model, the grid independence test is performed by comparing the CO_2 uptakes and average temperatures at 400 s, as shown in Fig. 3.4. As the grid number increases, both parameters gradually decrease and tend to stabilize. The relative errors for different grid numbers compared to 121,500 are listed in Table 3.4. To improve the computational efficiency while ensuring the simulation accuracy, a grid number of 73,500 is chosen as the balance point in this study.

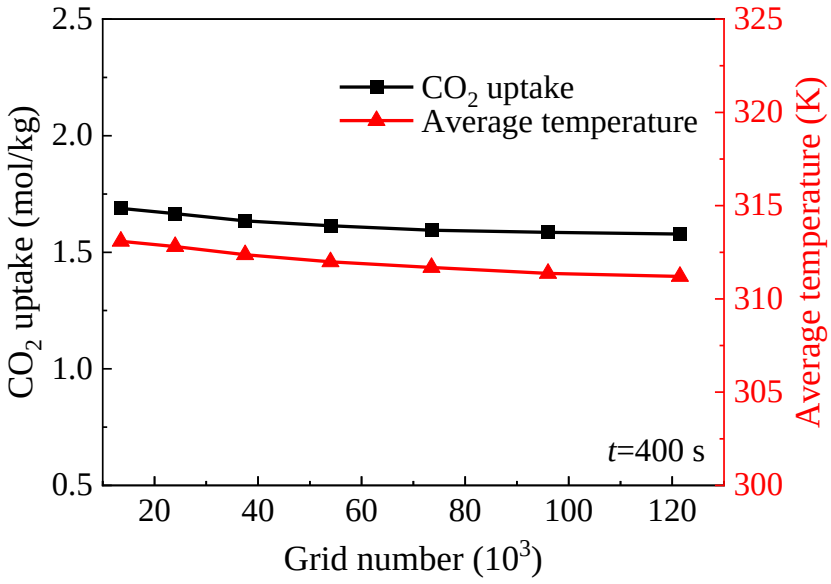

Fig. 3.4 Variation of CO_2 uptake and average temperature with grid number.

Table 3.4 Relative errors for different grid numbers compared to 121,500.

Grid number (10^3)		13.5	24	37.5	54	73.5	90
Relative error (%)	CO_2 uptake	6.98	5.54	3.57	2.24	1.03	0.46
	Average temperature	0.61	0.52	0.37	0.25	0.15	0.05

The breakthrough curve represents the variation of the ratio of the gas concentration at the outlet to the initial concentration with time during the adsorption process. In order to verify the credibility of the models, the simulated results of the breakthrough curve are compared with the corresponding experimental data under the same operating conditions, as shown in Fig. 3.5 [67]. Consistent with the scaling analysis, when the breakthrough curve appears, the adsorption process enters the heat-removing stage until the concentration ratio reaches 1, marking the end of the CO_2 adsorption. The results indicate that the relative error in time is between 2.73% and 16.42% when the same CO_2 concentration ratio is reached at the outlet, which is mainly related to the inevitable model error of adsorption kinetics. Nevertheless, the simulation models demonstrate good accuracy and are rational for this study.

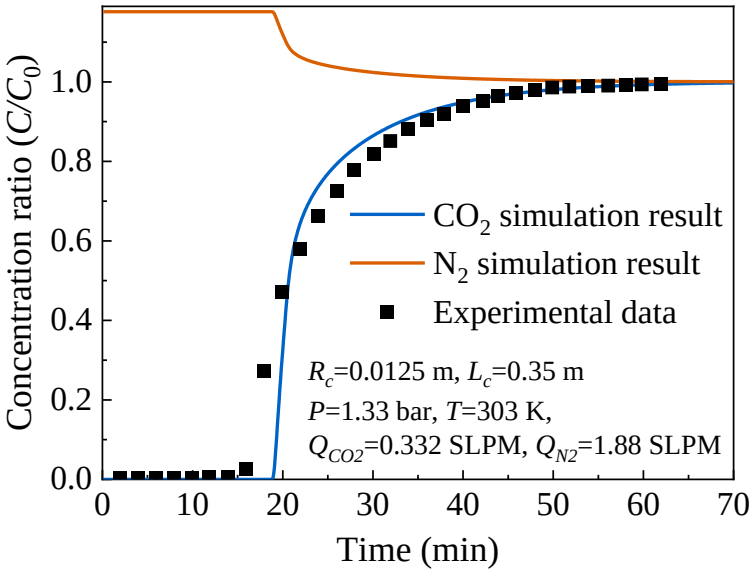

Fig. 3.5 Comparison of simulated and experimental results for breakthrough curves.

3.4.2 Comparison of CFD and scaling results

Fig. 3.6 shows the variation of the average temperature with time during the open CO_2 adsorption process compared with relevant scale parameters. Table 3.3 lists the scale parameters and their physical significance. Consistent with the scaling analysis, the average temperature in the adsorption bed rises to 312.2 K at 450 s, and then gradually returns to the initial temperature with time. Additionally, the variation of the average temperature at the symmetry axis and outlet indicates the rationality of the scaling analysis for the convective and diffusive terms in the energy equation in different stages. $t_{feed,CO2}$ predicts the duration of the feeding stage with an impressive accuracy, at the end of which the maximum average temperature in adsorption bed is reached. $\overline{T}_{max}$ is just 0.66% higher than the maximum average temperature during the adsorption process. When the time reaches t_{ad}, the average temperature in the bed decreases by 90.16% of the total temperature drop. Analyzing Eq. (3.27), the main

cause of the underestimation is the slightly higher prediction of the maximum average temperature rise scale.

The temperature contour plots at different times are displayed in Fig. 3.7 to delineate the heat transfer phenomenon in the adsorption bed. A local temperature rise area is observed, which gradually moves from the inlet to the outlet over time, representing the transition from the feeding phase to the heat-removing phase. This occurrence is attributed to the simultaneous adsorption heat generation and heat conduction/convection phenomena inside the bed. The scaling analysis presented in this study reasonably simplifies the given heat transfer behavior during the adsorption process by obtaining characteristic average temperature scales in the adsorption and non-adsorption regions.

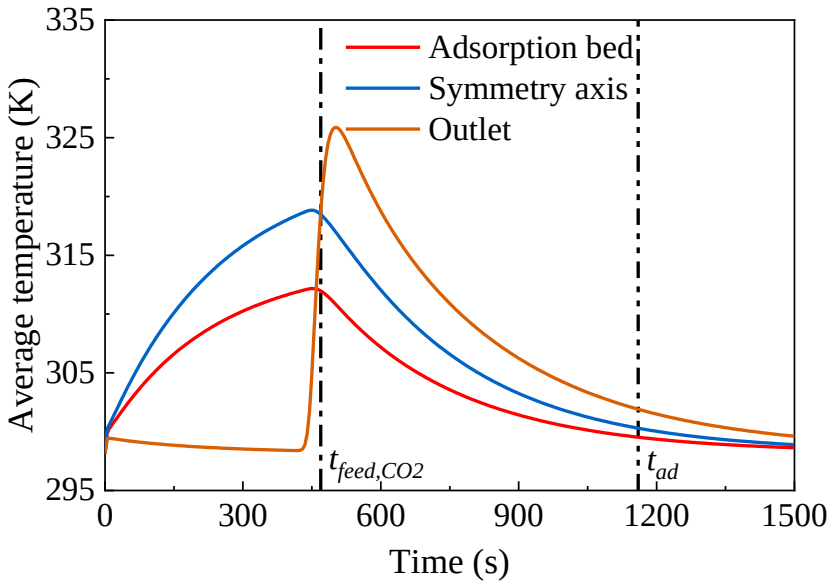

(a)

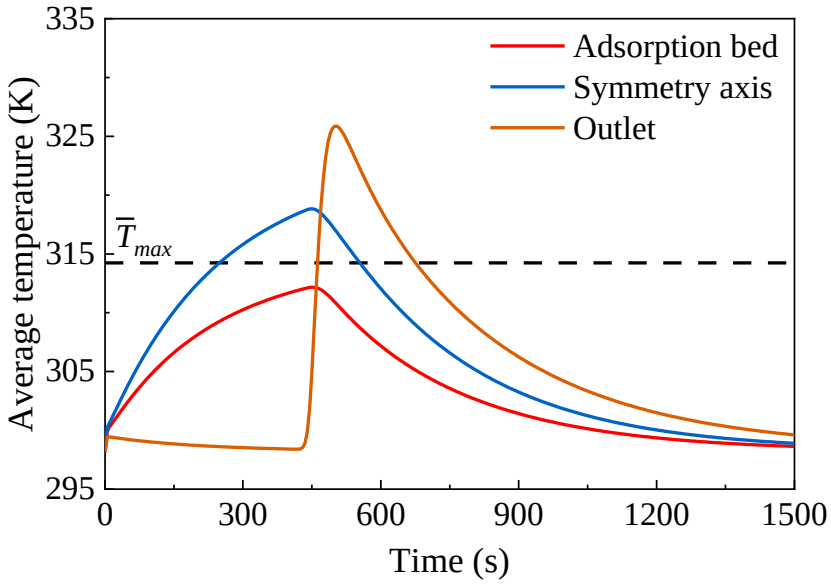

(b)

Fig. 3.6 Variation of average temperature with time in CFD simulation and relevant scale parameters: (a) feeding time and total time for CO_2 adsorption, (b) maximum average temperature.

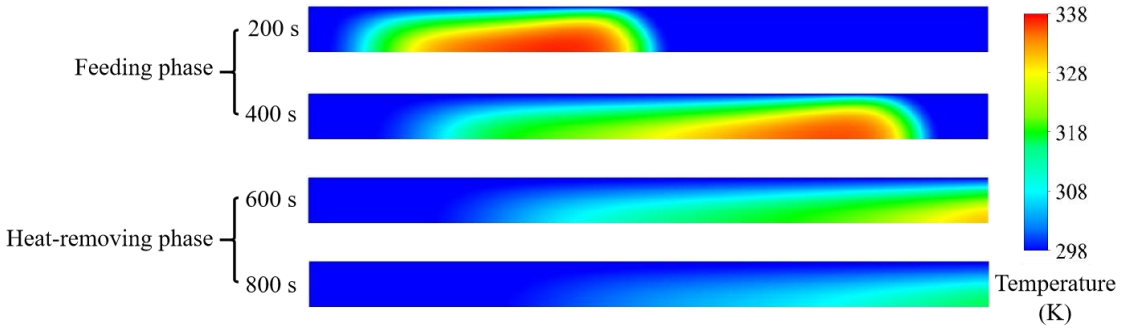

Fig. 3.7 Contour plots of temperature at different times.

Fig. 3.8 shows the variation of CO_2 uptake with time and compares it with relevant scale parameters. During the feeding stage, the supplied CO_2 at a stable flow

rate from the inlet is almost entirely adsorbed, resulting in a linear rise of CO_2 uptake with time. During the subsequent heat-removing stage, the CO_2 adsorption reaches equilibrium, but due to the gradual decrease of temperature, the equilibrium uptake further increases, and a portion of CO_2 continues to be adsorbed until the adsorption bed reaches the thermal equilibrium with the environment. Comparing the CFD results with the relevant scale parameters, $q_{feed,CO2}$ is 6.86% higher than the CO_2 uptake at the maximum average temperature rise (Fig. 3.8 (b)). When the adsorption time reaches t_{ad}, the CO_2 uptake is 98.10% of the equilibrium uptake. Therefore, the scale parameters exhibit high accuracy in predicting the mass transfer involved in the adsorption process.

Fig. 3.9 presents the contour plots of CO_2 uptake at various times. In the CO_2 adsorption region, almost all areas achieve equilibrium uptake. However, owing to the temperature distribution characteristics in the adsorption bed, the CO_2 uptake at the local temperature rise area, as shown in Fig. 3.7, cannot attain the maximum equilibrium value. In contrast, the CO_2 uptake in the low temperature area at the junction of the adsorption and non-adsorption regions is minimal due to the incomplete local adsorption attributed to adsorption kinetics, which corresponds to the transition region simplified in the previous scaling analysis.

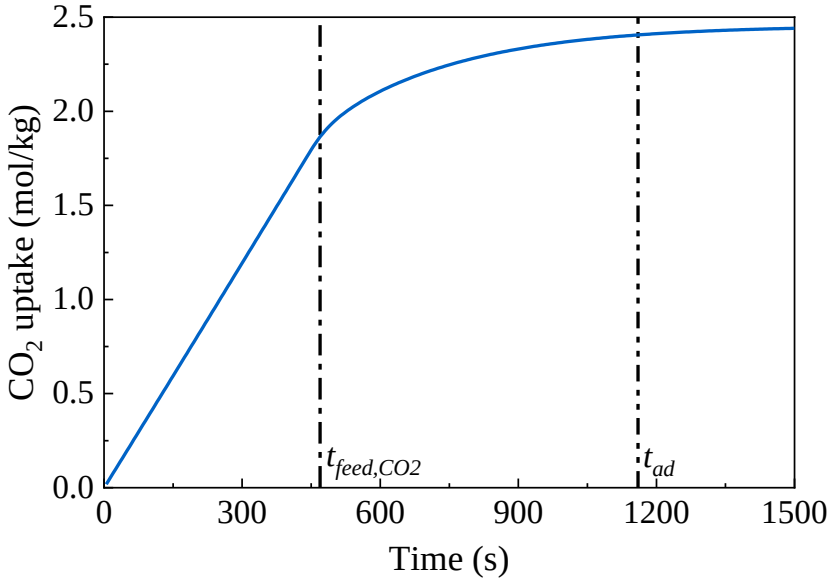

(a)

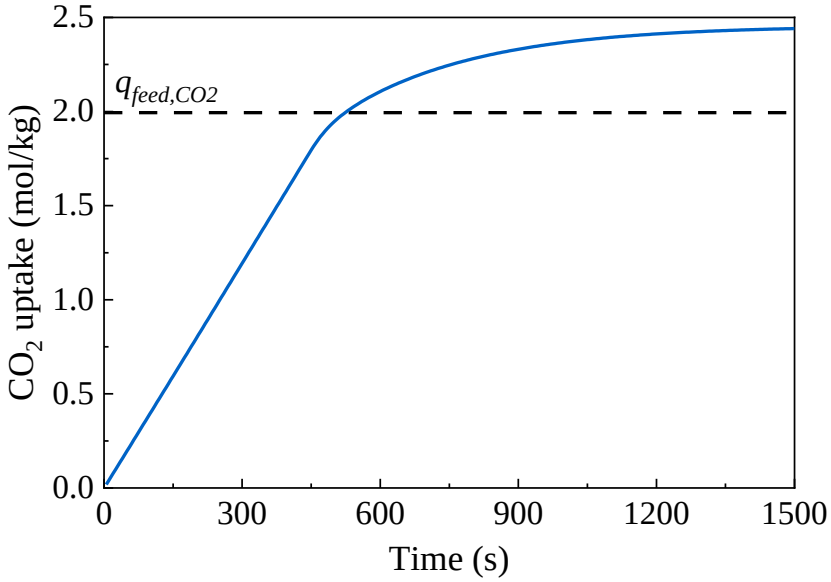

(b)

Fig. 3.8 Variation of CO_2 uptake with time in CFD simulation and relevant scale parameters: (a) feeding time and total time for CO_2 adsorption, (b) CO_2 uptake for feeding phase.

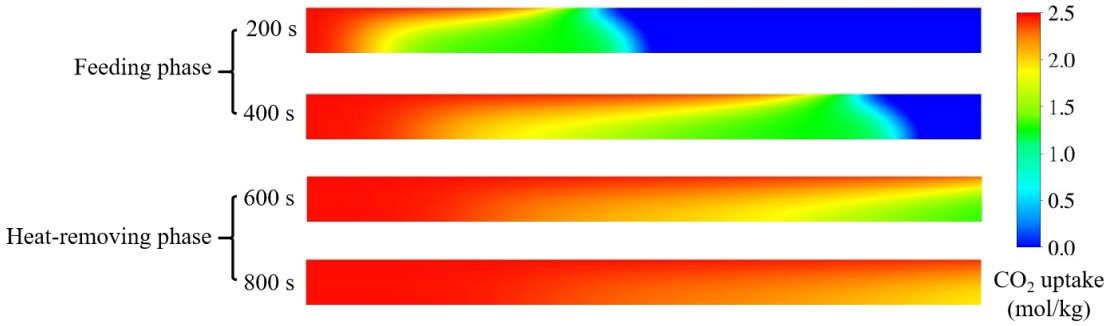

Fig. 3.9 Contour plots of CO_2 uptake at different times.

Fig. 3.10 illustrates the variation of N_2 uptake with time and the predicted scale parameter. For the zeolite 13X-APG under the studied conditions, the N_2 equilibrium uptake is approximately 1/20 of that of CO_2. Thus, compared to the CO_2 adsorption, the N_2 adsorption reaches equilibrium rather quickly. As the bed heats up due to adsorption, the N_2 equilibrium uptake decreases, and N_2 starts desorbing. It can be inferred that the N_2 uptake recovers while the bed temperature is returning to the initial temperature. At $t_{feed,N2}$, the actual N_2 uptake is 93.14% of the equilibrium adsorption. $t_{feed,N2}$ can also be considered as the time scale when the gas begins to flow out of the outlet.

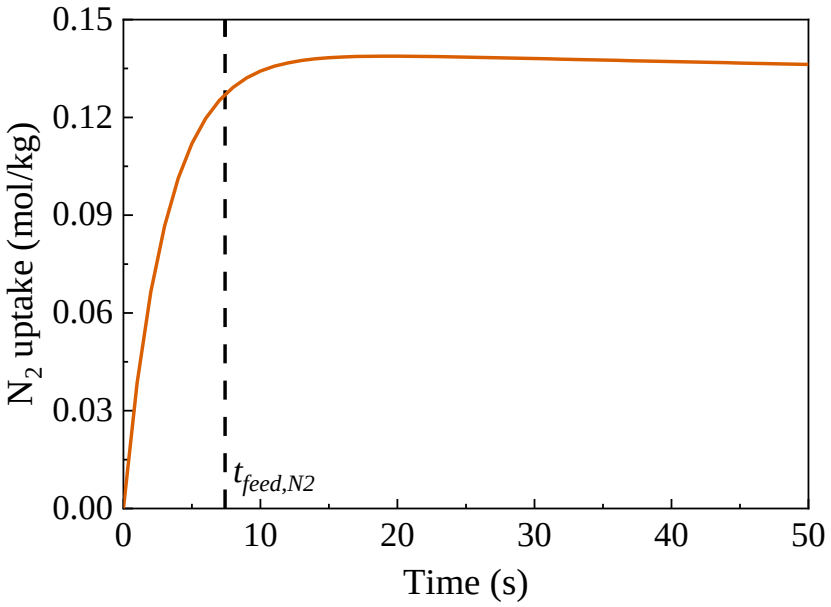

Fig. 3.10 Variation of N_2 uptake with time in CFD simulation and relevant scale parameter.

Fig. 3.11 displays the variation of the pressure drop in open adsorption bed with time and the equilibrium pressure drop scale ΔP_{eq}. The sharp increase in the flow pressure drop is attributed to the faster breakthrough of the N_2 gas. Subsequently, during the feeding stage, the flow pressure drop steadily increases as the area of CO_2 adsorption region increases. During the heat-removing stage, the CO_2 adsorption reaches equilibrium and the flow pressure drop gradually stabilizes. The scale parameter ΔP_{eq} predicts the pressure drop in the bed after CO_2 adsorption equilibrium, with an error of only 0.42%.

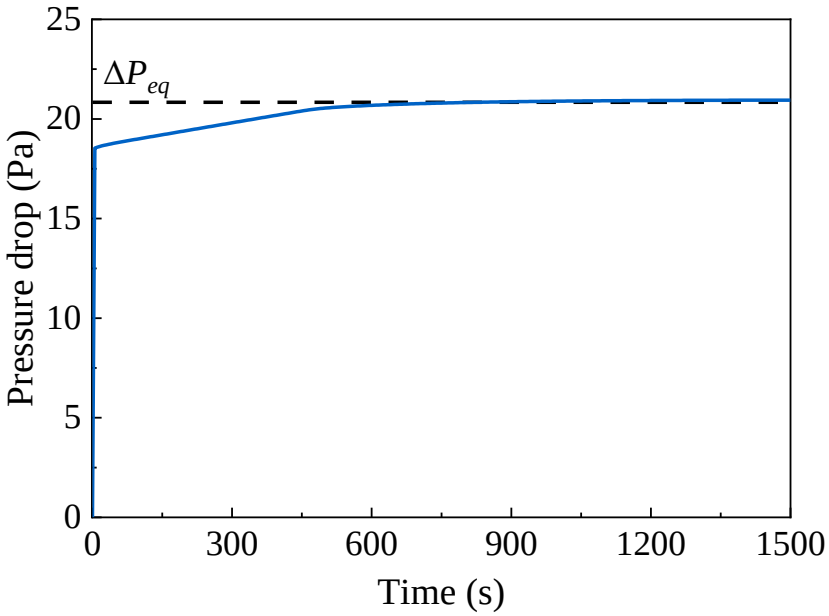

Fig. 3.11 Variation of pressure drop with time in CFD simulation and relevant scale parameter.

3.4.3 Effect of different parameters on scaling results

The comparison between the scaling analysis and numerical study demonstrates the efficacy of scaling analysis for the thermal design and management of open adsorption process. In practice, multiple parameters are simultaneously adjusted to optimize the performance of adsorption process. In this section, the effect of thermal conductivity of the adsorbent, porosity, inlet velocity and length-diameter ratio of the adsorption bed on scale parameters are investigated. By comprehensively considering their impacts, rational suggestions are proposed for open CO_2 adsorption design.

Fig. 3.12 shows the effect of thermal conductivity of adsorbent on different scale parameters. The increase of thermal conductivity promotes the heat dissipation throughout the process, consequently decreasing t_{ad} and $\overline{T}_{max}$. The decrease of $\overline{T}_{max}$

affects the equilibrium adsorption and increases $q_{feed,CO2}$. $t_{feed,CO2}$ also increases accordingly due to the linear relationship between $t_{feed,CO2}$ and $q_{feed,CO2}$. With reduced t_{ad} while other conditions unchanged, $R_{re,CO2}$ increases. The change of thermal conductivity has no effect on the flow characteristics, hence the pressure drop scale is not discussed here. Additionally, Fig. 3.12 (a) compares the extreme cases where the thermal conductivity of adsorbent is 0 and infinite, with t_{ad} being 2022 s and 579 s, respectively. The case with infinite thermal conductivity can be regarded with no temperature rise, and the adsorption process all belongs to the feeding phase.

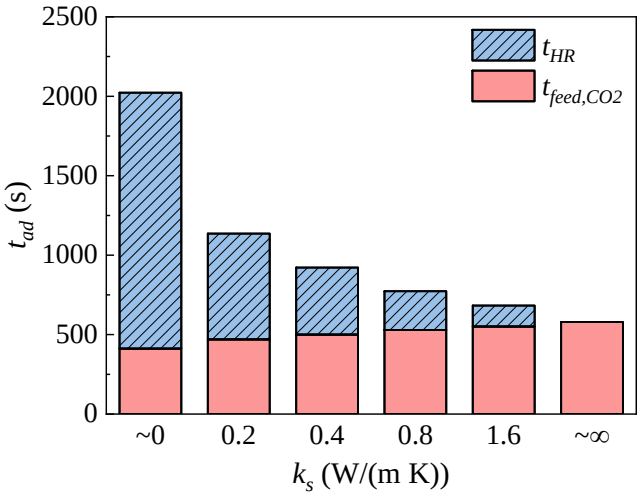

(a)

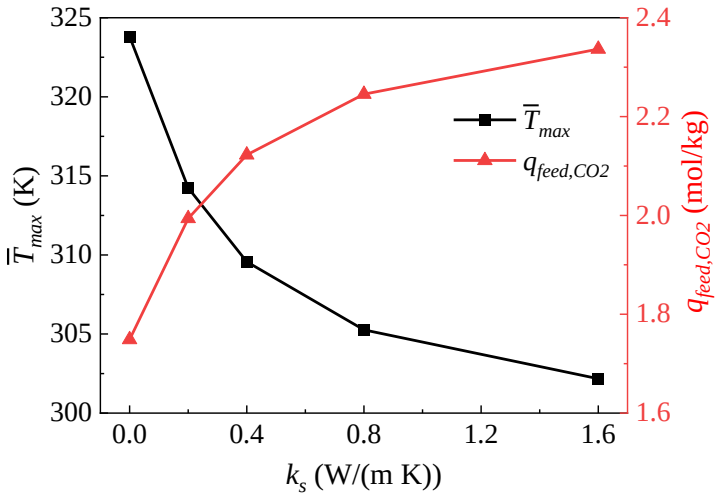

(b)

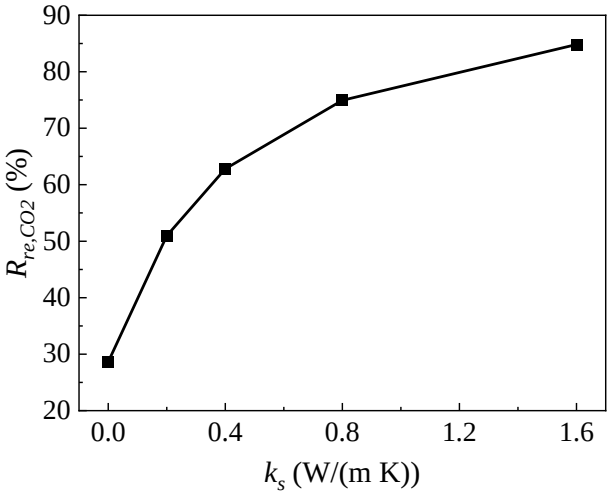

(c)

Fig. 3.12 Different scale parameters versus thermal conductivity of adsorbent: (a) time, (b) maximum average temperature and CO_2 uptake for feeding phase, (c) CO_2 removal rate.

Fig. 3.13 shows the effect of the variation in porosity ranging from 0.365 to 0.765 on scale parameters. As the porosity increases, the proportion of adsorbent in the same space decreases, leading to a reduction of the total uptake, so both time scales decrease. Likewise, as the volume fraction of the fluid domain increases, the effective thermal conductivity decreases due to the much smaller thermal conductivity of gas than that of the solid adsorbent. Therefore, $\overline{T}_{max}$ increases, and $q_{feed,CO2}$ decreases. The decrease of $R_{re,CO2}$ indicates that the increase in porosity reduces the role of heat conduction and thus lowers the overall CO_2 adsorption efficiency. However, the decrease of ΔP_{eq} reflects the advantage of increasing porosity, which needs to be comprehensively considered based on the actual requirements in the design of adsorption beds.

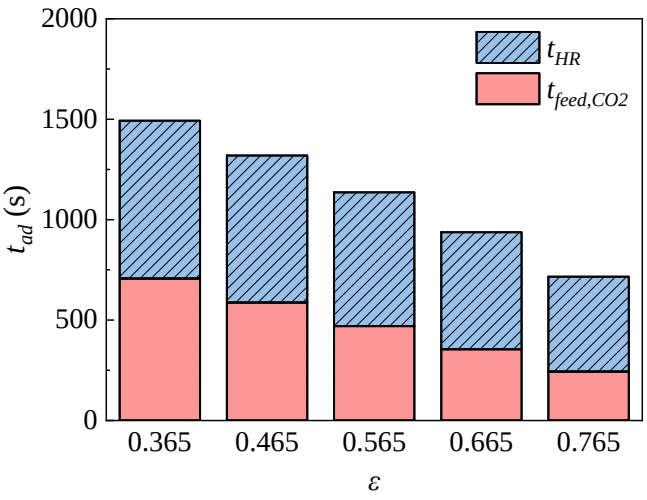
2000
1500
1000
500
0
t_{ad} (s)
t_{HR}
$t_{feed,CO2}$
0.365
0.465
0.565
0.665
0.765
ε

(a)

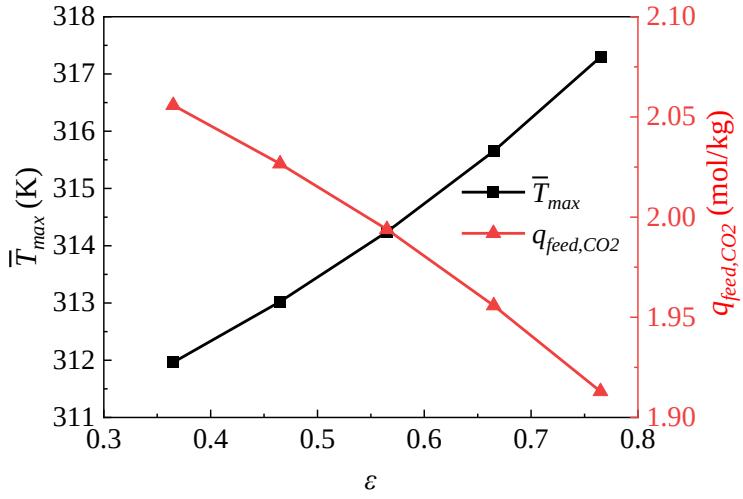
318
317
316
315
314
313
312
311
$\overline{T}_{max}$ (K)
2.10
2.05
2.00
1.95
1.90
$q_{feed,CO2}$ (mol/kg)
$\overline{T}_{max}$
$q_{feed,CO2}$
0.3
0.4
0.5
0.6
0.7
0.8
ε

(b)

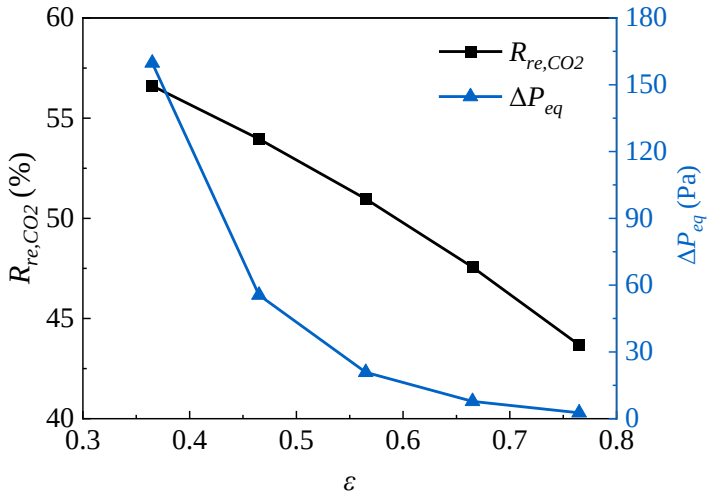
60
55
50
45
40
$R_{re,CO2}$ (%)
180
150
120
90
60
30
0
ΔP_{eq} (Pa)
$R_{re,CO2}$
ΔP_{eq}
0.3
0.4
0.5
0.6
0.7
0.8
ε

(c)

Fig. 3.13 Different scale parameters versus porosity: (a) time, (b) maximum average temperature and CO_2 uptake for feeding phase, (c) CO_2 removal rate and equilibrium pressure drop.

Fig. 3.14 shows the effect of the gas inlet velocity on various scale parameters. A higher inlet velocity improves the overall adsorption rate. When the inlet velocity increases from 0.025 m/s to 0.125 m/s, $t_{feed,CO2}$ decreases by 82.73%, while t_{HR} decreases by 44.53%. The inlet velocity is found to have a greater impact on the feeding stage than on the heat-removing stage. However, with faster adsorption rates in the feeding stage, $\overline{T}_{max}$ increases at the constant thermal conductivity. Additionally, the resultant decrease of $R_{re,CO2}$ and the increase of ΔP_{eq} is detrimental to the performance of open adsorption system.

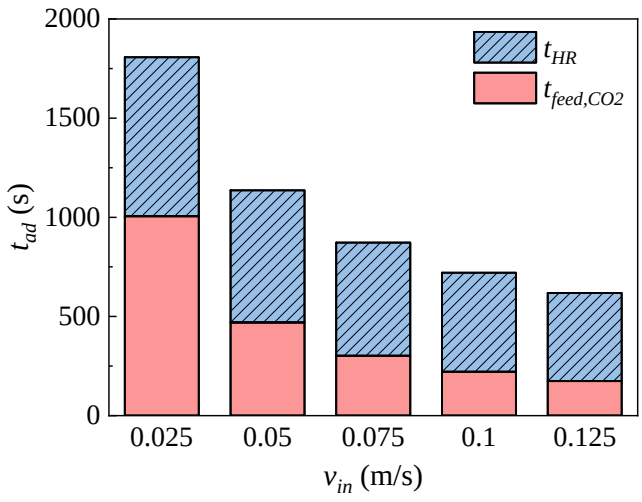

(a)

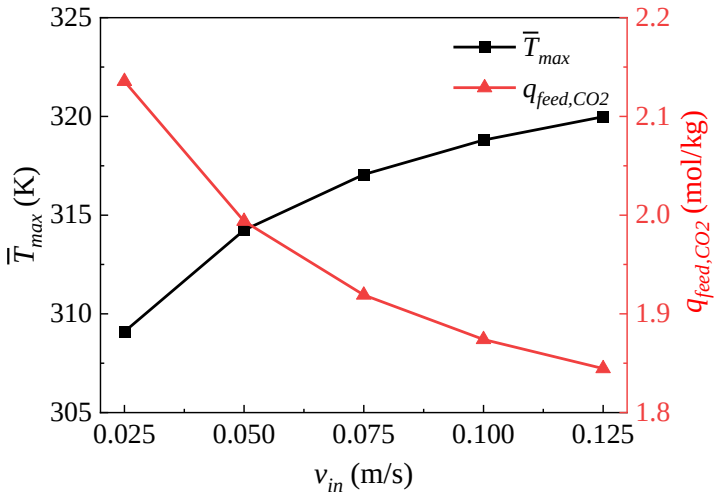

(b)

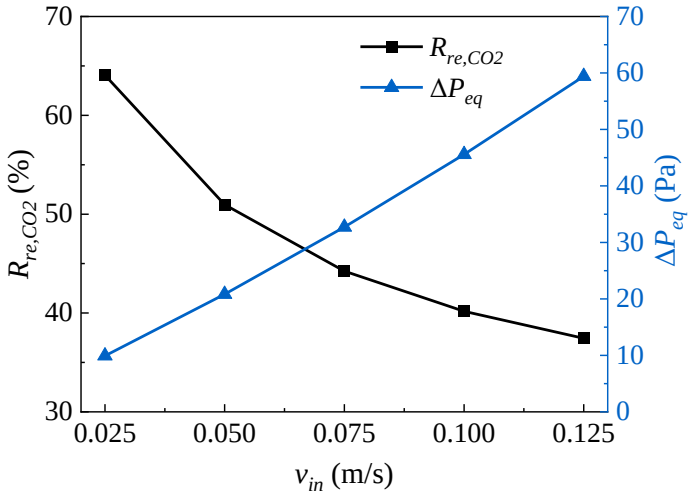

(c)

Fig. 3.14 Different scale parameters versus inlet velocity: (a) time, (b) maximum average temperature and CO_2 uptake for feeding phase, (c) CO_2 removal rate and equilibrium pressure drop.

Fig. 3.15 shows the effect of the length-diameter (L/D) ratio of adsorption bed with constant volume on various scale parameters. As the L/D ratio increases, the decrease of Y makes it easier for the adsorption heat to be conducted to the wall. A higher L/D ratio improves the adsorption heat conduction through the walls due to the

reduced value of *Y* in Fig. 3.1 (a). As a result, $\overline{T}_{max}$ decreases, $q_{feed,CO2}$ increases, and $t_{feed,CO2}$ also slightly increases. Moreover, the better heat-removing effect significantly reduces t_{HR}, resulting in a decreasing trend in t_{ad} and an increasing trend in $R_{re,CO2}$. But the faster gas velocity and longer flow path (*X*) cause a sharp increase of ΔP_{eq}.

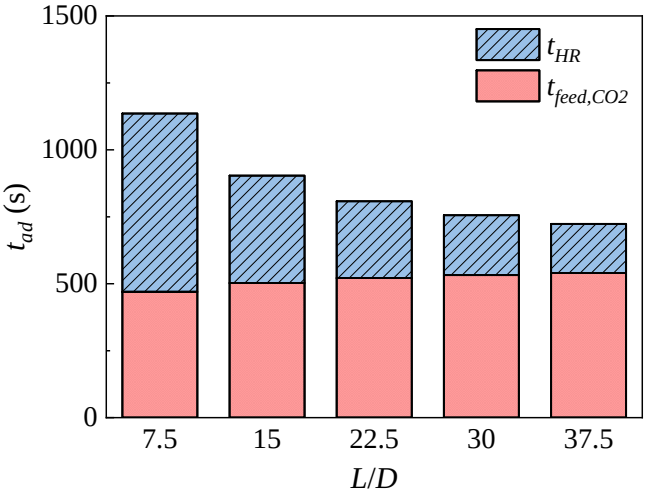

(a)

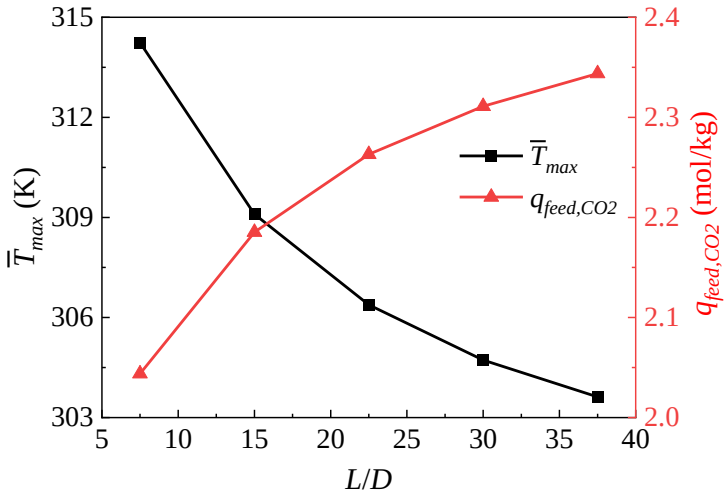

(b)

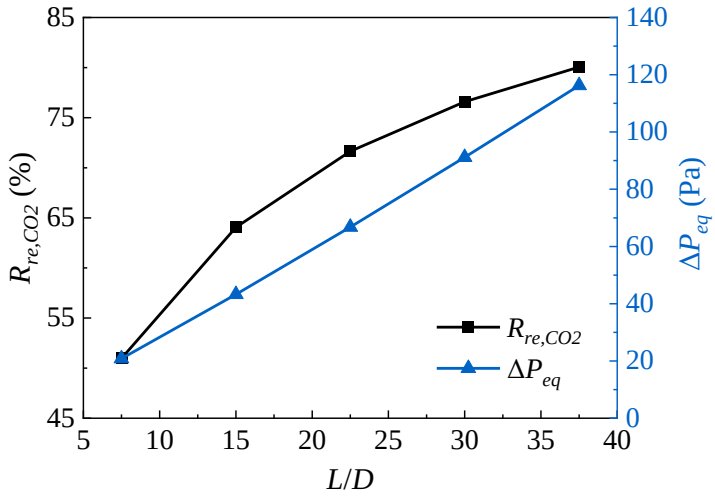

(c)

Fig. 3.15 Different scale parameters versus length-diameter ratio of adsorption bed: (a) time, (b) maximum average temperature and CO_2 uptake for feeding phase, (c) CO_2 removal rate and equilibrium pressure drop.

3.4.4 Parameter sensitivity analysis

A parameter sensitivity analysis is performed to further investigate the degree of influence of the adsorption bed parameters on the scale parameters. Among the scale parameters listed in Table 3.3, total time scale, maximum average temperature scale, CO_2 removal rate and equilibrium pressure drop scale are selected as the performance metrics. In Section 3.4.3, the thermal conductivity of adsorbent, porosity, inlet velocity and length-diameter ratio of adsorption bed are used as input variables. The input and output variables are shown below:

$$x_i \in \{k_s, \varepsilon, v_{in}, L/D\};\ y_j \in \{t_{ad}, \bar{T}_{max}, R_{re,CO2}, \Delta P_{eq}\} \tag{3.35}$$

With the operating parameters listed in Table 3.2 as the reference conditions, the absolute sensitivity of the output variables is defined as its partial derivative with

respect to each input variable at the current conditions. This will result in a Jacobian matrix, where the elements in each row and column can be expressed as [110]:

$$S_{ij} = \frac{\partial y_j}{\partial x_i} \tag{3.36}$$

In practice, absolute sensitivity characterizes the actual change of output variable resulting from a unit change of input variable. It is difficult to compare the absolute sensitivity for the physical quantities with different dimensions and meanings. To address this problem, relative sensitivity is used to represent the relative degree of change in each variable instead of the absolute changes, which can be expressed as follows [111,112]:

$$S_{ij}^{'} = \frac{\partial y_j / y_j}{\partial x_i / x_i} = \frac{\partial \ln y_j}{\partial \ln x_i} \tag{3.37}$$

The sensitivity analysis on various scale parameters generates the critical values of input parameters. Considering a 1% range of variation, the absolute and relative sensitivities of output variables to input variables are shown in Table 3.5. The symbol (+/-) for each sensitivity indicates the positive or negative impact of changes in the input parameters of adsorption bed on the output scaling results. Based on the absolute sensitivity, the inlet velocity has a significant impact on each output variable because of its small magnitude. The porosity is determined as the dominant factor affecting the four performance scale parameters, with relative sensitivities of -0.945, 0.0235, -0.357 and -5.33, respectively. The increase of porosity has positive effects on t_{ad} and ΔP_{eq}, while it negatively impacts $\overline{T}_{max}$ and $R_{re,CO2}$, which has to be considered from actual demands in the design of adsorption bed. Besides, increasing the thermal conductivity of adsorbent improves all three scale parameters except for constant ΔP_{eq}. Thus,

development of modified adsorbent to increase its thermal conductivity is envisaged as a focal point for future relevant research.

Table 3.5 Sensitivity analysis results of performance scale parameters for open CO_2 adsorption.

	S_{ij}				$S_{ij}^{'}$			
y / x	t_{ad}	$\bar{T}_{max}$	$R_{re,CO2}$	ΔP_{eq}	t_{ad}	$\bar{T}_{max}$	$R_{re,CO2}$	ΔP_{eq}
k_s	-1721	-31.9	77.5	–	-0.303	-0.0203	0.304	–
ε	-1898	13	-32.2	-196	-0.945	0.0235	-0.357	-5.33
v_{in}	-14664	146	-353	456	-0.646	0.0232	-0.347	1.09
L/D	-51.7	-0.984	2.33	2.91	-0.342	-0.0235	0.343	1.05

3.5 Conclusions

Analyses on the scaling of the transfer mechanisms and their sensitivities for an open adsorption system to capture CO_2 were conducted. The adsorption process is divided into two stages: feeding stage and heat-removing stage. Through macroscopic simplifications and order-of-magnitude comparisons for different terms in balance equations, the scale parameters characterizing the adsorption process were obtained. A

CFD simulation for the same adsorption domain was performed, which validated the reliability of scaling analysis of the open adsorption process. Key conclusions are:

1. During the feeding stage, the CO_2 adsorption region gradually occupies the entire adsorption bed, raising the bed temperature significantly due to higher adsorption heat release. Heat conduction substantially dominates the heat transfer during this stage.

2. During the heat-removing stage, the high-temperature fluid can be observed to flow out of the outlet, and the adsorption heat is removed synchronously by both heat conduction and heat convection. The heat dissipation capacity of adsorption bed has an important impact on the duration of this stage.

3. The four performance scale parameters, t_{ad}, $\overline{\mathrm{T}}_{\max}$, $R_{re,CO2}$ and ΔP_{eq}, have maximum relative sensitivity to porosity (ε), with -0.945, 0.0235, -0.357 and -5.33, respectively. Due to this trade-off effects, an optimum value of ε should be considered based on practical design requirements.

4. Increasing the thermal conductivity of adsorbent has a positive effect on t_{ad}, $\overline{T}_{max}$, and $R_{re,CO2}$ except for ΔP_{eq}, which deserves attention in future related research.

Overall, the scaling and sensitivity results provide an accurate depiction of the characteristics of open adsorption process for CO_2 capture which can be useful in design and analysis procedures.

Chapter 4 Analysis of CO_2 temperature swing adsorption system integrated with adsorption heat transformer

4.1 Introduction

Besides solar and wind energy, waste heat dissipated in various industries can also be utilized to reduce the energy consumption of carbon capture systems [113]. Approximately 15% to 50% of the energy supply in different industries is dissipated as waste heat in the form of cooling water, exhaust gases, etc [114]. The current research has not yet considered the feasibility of integrating the AHT system with adsorption-based carbon capture system. Additionally, scaling analysis, as an effective process analysis method, has not been applied to the analysis of cycle.

In this chapter, scaling analysis based on the cycle description is performed for the three-step CO_2 temperature swing adsorption (TSA) cycle, and the characteristic scales of each process are identified. By referencing parameters that characterize different properties, detailed performance analyses are conducted for both the single TSA system and the AHT-TSA system. The research findings contribute to the optimization of related integrated systems.

4.2 Scaling analysis of TSA cycle

4.2.1 Cycle description

In this chapter, the open CO_2 adsorption cycle studied is the three-step TSA cycle, in which the steps are given in Fig. 4.1.

Step 1: The simulated flue gas (CO_2/N_2) enters the adsorption bed, and at ambient temperature, CO_2 is adsorbed by the adsorbent. When adsorption reaches equilibrium, the adsorption process ends and the outlet is sealed.

Step 2: High temperature heat transfer oil carries heat and flows to exchange heat with the adsorption bed, causing the bed temperature to rise and desorption to begin. The CO_2 adsorbed by the adsorbent is released and flows out from the bottom of the bed to be captured. When the CO_2 uptake reaches a minimum, i.e. equilibrium adsorption at high temperature, the desorption process is complete. The adsorption bed is completely sealed.

Step 3: The heat transfer medium at ambient temperature removes the heat from the adsorption bed from the previous step. Until the bed temperature drops to thermal equilibrium with the environment. During this process, no gas enters or exits the adsorption bed. Then Step 1 is repeated for the next TSA cycle.

For this study, the adsorption bed parameters and condition range for the TSA cycle are shown in Table 4.1. During the desorption process, the adsorption bed undergoes heat exchange with external HTF at a certain flow rate. While in the adsorption and cooling processes, the wall temperature is set to remain constant at the ambient temperature.

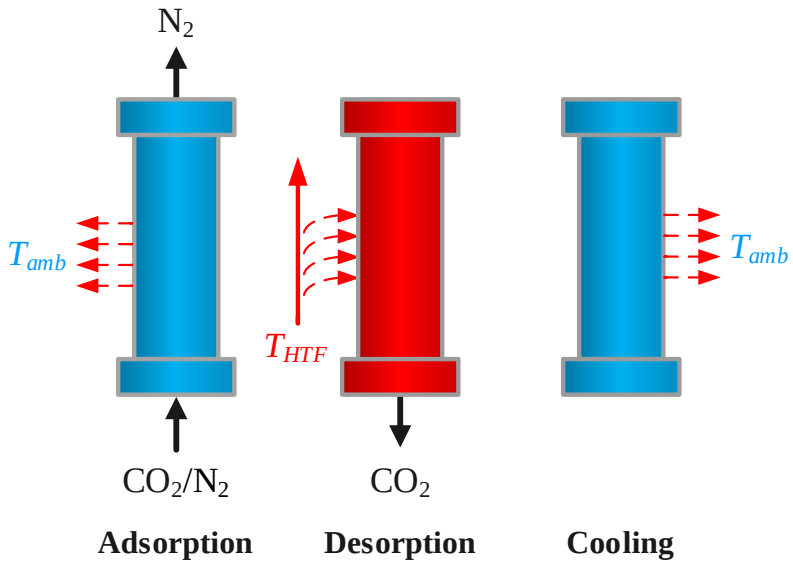

Fig. 4.1 Schematic diagram of three-step TSA cycle

Table 4.1 Parameters of adsorption bed and operating conditions.

Parameter	Value
X (m)	0.5
Y (m)	0.015
v_{in} (m/s)	0.025~0.125 (0.05) [a]
$\dot{m}_{HTF}$ (kg/s)	0.1~0.3 (0.2) [a]
T_{amb} (°C)	0~30 (25) [a]
T_{HTF} (°C)	100~130 (120) [a]

a: The content in the parentheses represents the reference condition.

4.2.2 Adsorption process

According to the description in Chapter 3, the adsorption process is divided into a feeding phase and a heat-removing phase. Similarly, this chapter continues this idea by dividing the adsorption process into two stages. The difference, however, is that since the cycle being considered is in dynamic equilibrium, the initial minimum adsorption uptake is the equilibrium uptake at ambient temperature, rather than 0. The detailed scaling analysis for feeding phase is as follows:

$$\underbrace{\varepsilon\frac{\partial(\rho Y_i)}{\partial t}}_{\frac{\varepsilon\rho Y_{CO2}}{t_{feed}}} + \underbrace{\frac{\partial(\rho v_x Y_i)}{\partial x}}_{\frac{v_{in}\rho Y_{CO2}}{X}} = \underbrace{(1-\varepsilon)\rho_s M_i\frac{\partial q_i}{\partial t}}_{\frac{(1-\varepsilon)\rho_s M_{CO2}\Delta q_{feed}}{t_{feed}}} \tag{4.1}$$

$$\frac{\varepsilon\rho_{CO2}X_{CO2}}{t_{feed}} \qquad \frac{v_{in}\rho_{CO2}X_{CO2}}{X}$$

$$\Delta q_{feed} = q_{feed} - q_{min} \tag{4.2}$$

The feeding time scale for CO_2 adsorption can be expressed as follows:

$$t_{feed} \sim \frac{(1-\varepsilon)\rho_s M_{CO2}\Delta q_{feed} X}{v_{in}\rho_{CO2}X_{CO2}} \tag{4.3}$$

The energy scaling analysis during the feeding phase is given:

$$\underbrace{(1-\varepsilon)\frac{\partial(\rho_s C_{p,s}T)}{\partial t}}_{\frac{(1-\varepsilon)\rho_s\Delta(C_{p,s}T)_{feed}}{t_{feed}}} + \cancel{\frac{\partial(v_x\rho C_p T)}{\partial x}} = \underbrace{k_{eff}\frac{\partial^2 T}{\partial y^2}}_{\frac{k_{eff}\Delta\bar{T}_{max}}{Y^2}} + \underbrace{(1-\varepsilon)\rho_s\sum_i -\Delta H_i\frac{\partial q_i}{\partial t}}_{\frac{(1-\varepsilon)\rho_s(-\Delta H_{CO2}\Delta q_{feed})}{t_{feed}}} \tag{4.4}$$

$$\Delta(C_{p,s}T)_{feed} = C_{p,s}^{feed}\Delta\bar{T}_{max} + \Delta C_{p,s}^{feed}T_{amb} \tag{4.5}$$

$$\Delta\bar{T}_{max} \sim \frac{(1-\varepsilon)\rho_s Y^2\left(-\Delta H_{CO2}\Delta q_{feed} - \Delta C_{p,s}^{feed} T_{amb}\right)}{(1-\varepsilon)\rho_s C_{p,s}^{feed} Y^2 + k_{eff} t_{feed}} \tag{4.6}$$

At the end of the feeding phase, the entire adsorption domain has almost reached a state of equilibrium adsorption at this temperature scale. At this moment, the CO_2 adsorption uptake scale is:

$$q_{feed} \sim \frac{q_{m,CO2} P_{CO2} K_{0,CO2} e^{\left(\frac{-\Delta H_{CO2}}{R\bar{T}_{max}}\right)}}{\left(1+\left(P_{CO2} K_{0,CO2} e^{\left(\frac{-\Delta H_{CO2}}{R\bar{T}_{max}}\right)}\right)^{n_{CO2}}\right)^{\left(\frac{1}{n_{CO2}}\right)}} \tag{4.7}$$

By solving the system of equations formed by Eq. (4.3), (4.6) and (4.7), the scaling parameters for the feeding stage can be obtained:

$$\begin{cases} t_{feed} \sim \dfrac{(1-\varepsilon)\rho_s M_{CO2}\Delta q_{feed} X}{v_{in}\rho_{CO2} X_{CO2}} \\ \Delta\bar{T}_{max} \sim \dfrac{(1-\varepsilon)\rho_s Y^2\left((-\Delta H_{CO2}\Delta q_{feed}) - \Delta C_{p,s}^{feed} T_{amb}\right)}{(1-\varepsilon)\rho_s C_{p,s}^{feed} Y^2 + k_{eff} t_{feed}} \\ q_{feed} \sim \dfrac{q_{m,CO2} P_{CO2} K_{0,CO2} e^{\left(\frac{-\Delta H_{CO2}}{R\bar{T}_{max}}\right)}}{\left(1+\left(P_{CO2} K_{0,CO2} e^{\left(\frac{-\Delta H_{CO2}}{R\bar{T}_{max}}\right)}\right)^{n_{CO2}}\right)^{\left(\frac{1}{n_{CO2}}\right)}} \end{cases} \tag{4.8}$$

During heat-removing phase, when the heat in the adsorption bed is removed, CO_2 will be further adsorbed, the process will release additional heat. In this stage, the scaling transformations for each term are as follows:

$$\underbrace{(1-\varepsilon)\frac{\partial(\rho_s C_{p,s}T)}{\partial t}}_{\frac{(1-\varepsilon)\rho_s\Delta(C_{p,s}T)_{HR}}{t_{HR}}}+\underbrace{\frac{\partial(v_x\rho C_pT)}{\partial x}}_{\frac{v_{in}\rho C_p\Delta\bar{T}_{max}}{X}}=\underbrace{k_{eff}\frac{\partial^2T}{\partial y^2}}_{\frac{k_{eff}\Delta\bar{T}_{max}}{Y^2}}+\underbrace{(1-\varepsilon)\rho_s\sum_i-\Delta H_i\frac{\partial q_i}{\partial t}}_{\frac{(1-\varepsilon)\rho_s\left(-\Delta H_{CO2}\Delta q_{HR}\right)}{t_{HR}}} \tag{4.9}$$

$$\Delta q_{HR}=q_{max}-q_{feed} \tag{4.10}$$

$$\Delta(C_{p,s}T)_{HR}=\Delta C_{p,s}^{HR}T_{amb}-C_{p,s}^{feed}\Delta\bar{T}_{max} \tag{4.11}$$

Then, the time scale can be calculated by the following equation:

$$t_{HR}\sim\frac{(1-\varepsilon)\rho_s XY^2\left(-\Delta H_{CO2}\Delta q_{HR}-\Delta(C_{p,s}T)_{HR}\right)}{\left(v_{in}\rho C_pY^2+k_{eff}X\right)\Delta\bar{T}_{max}} \tag{4.12}$$

The total time scale is obtained by summing those of feeding phase and heat-removing phase, which represent the end time of adsorption process, as follows:

$$t_{ad}=t_{feed}+t_{HR} \tag{4.13}$$

4.2.3 Desorption process

During desorption process, adsorbate CO_2 is desorbed at high temperature and collected away from the bed. The mass scaling analysis of the process is as follows:

$$\underbrace{\varepsilon\frac{\partial(\rho Y_i)}{\partial t}}_{\frac{\varepsilon\rho Y_{CO2}}{t_{de}}}+\underbrace{\frac{\partial(\rho v_xY_i)}{\partial x}}_{\frac{v_x\rho Y_{CO2}}{X}}=\underbrace{-(1-\varepsilon)\rho_sM_i\frac{\partial q_i}{\partial t}}_{\frac{(1-\varepsilon)\rho_sM_{CO2}\Delta q_{CO2}}{t_{de}}} \tag{4.14}$$

$$\Downarrow \qquad \Downarrow$$

$$\cancel{\frac{\varepsilon\rho_{CO2}X_{CO2}}{t_{de}}} \qquad \frac{v_x\rho_{CO2}X_{CO2}}{X}$$

$$v_x \sim \frac{(1-\varepsilon)\rho_s M_{CO2} \Delta q_{CO2} X}{t_{de} \rho_{CO2} X_{CO2}} \tag{4.15}$$

where the unkown parameters are set as:

$$\Delta q_{CO2} = q_{max} - q_{min} \tag{4.16}$$

$$X_{CO2} \sim 1 \tag{4.17}$$

Next, an analysis of the energy equation is conducted. Since this process is primarily controlled by heat transfer, grasping the heat conduction term is crucial. The following equations are derived:

$$\Delta T = T_{HTF} - T_{amb} \tag{4.18}$$

$$h_{HTF}(T_{HTF} - T_w) \sim \frac{k_{eff}}{Y^2}(T_w - T_{amb}) \tag{4.19}$$

$$T_w - T_{amb} \sim \frac{h_{HTF} \Delta T}{h_{HTF} + k_{eff}/Y^2} \tag{4.20}$$

$$h_{HTF} = \frac{Nu_{HTF} k_{HTF}}{d_e} \tag{4.21}$$

$$Nu_{HTF} = \begin{cases} 4.36 + 5.36 \times 10^{-9} Re_{HTF}^{2.39} & Re_{HTF} < 2300 \\ \dfrac{(f_{HTF}/8)(Re_{HTF} - 1000) Pr_{HTF}}{1.07 + 12.7\sqrt{f_{HTF}/8}(Pr_{HTF}^{2/3} - 1)} & Re_{HTF} \geq 2300 \end{cases} \tag{4.22}$$

$$f_{HTF} = \left[1.82 \log_{10}(Re_{HTF}) - 1.64\right]^{-2} \tag{4.23}$$

$$Re_{HTF} = \frac{4 m_{HTF}}{\pi \mu D_e} \tag{4.24}$$

It can be seen that the heat transfer in this process is highly related to the flow rate of the external HTF. Thus, the scaling analysis can be done as follows:

$$\underbrace{(1-\varepsilon)\frac{\partial(\rho_s C_{p,s}T)}{\partial t}}_{\frac{(1-\varepsilon)\rho_s\Delta(C_{p,s}T)_{de}}{t_{de}}} + \underbrace{\frac{\partial(v_x\rho C_pT)}{\partial x}}_{\frac{v_x\rho_{CO2}X_{CO2}C_p\overline{T}}{X}} = \underbrace{k_{eff}\frac{\partial^2 T}{\partial y^2}}_{\frac{k_{eff}h_{HTF}\Delta T}{2Y^2(h_{HTF}+k_{eff}/Y^2)}} + \underbrace{(1-\varepsilon)\rho_s\sum_i -\Delta H_i\frac{\partial q_i}{\partial t}}_{\frac{(1-\varepsilon)\rho_s(-\Delta H_{CO2}\Delta q_{CO2})}{t_{de}}} \quad (4.25)$$

$$\Downarrow$$

$$\cancel{\frac{(1-\varepsilon)\rho_s M_{CO2}\Delta q C_p\overline{T}}{t_{de}}}$$

$$\Delta(C_{p,s}T)_{de} = C_{p,s}^{min}\Delta T - \Delta C_{p,s}T_{amb} \quad (4.26)$$

$$t_{de} \sim \frac{2(Y^2h_{HTF}+k_{eff})(1-\varepsilon)\rho_s\left[\Delta(C_{p,s}T)+(-\Delta H_{CO2}\Delta q)\right]}{k_{eff}h_{HTF}\Delta T} \quad (4.27)$$

4.2.4 Cooling process

During the cooling process, it is assumed that the adsorption uptake remains almost unchanged. For the closed adsorption bed at this stage, the time scale can be derived as follows:

$$\underbrace{(1-\varepsilon)\frac{\partial(\rho_s C_{p,s}T)}{\partial t}}_{\frac{(1-\varepsilon)\rho_s C_{p,s}^{min}\Delta T}{t_{cool}}} + \cancel{\frac{\partial(v_x\rho C_pT)}{\partial x}} = \underbrace{k_{eff}\frac{\partial^2 T}{\partial y^2}}_{\frac{k_{eff}\Delta T}{2Y^2}} + \cancel{(1-\varepsilon)\rho_s\sum_i -\Delta H_i\frac{\partial q_i}{\partial t}} \quad (4.28)$$

$$t_{cool} \sim \frac{2Y^2(1-\varepsilon)\rho_s C_{p,s}^{min}}{k_{eff}} \quad (4.29)$$

4.2.5 Performance analysis

In order to evaluate and optimize the CO_2 adsorption performance, based on the

scaling analyses of the three stages, the performance of TSA cycle needs to be further investigated. The parameters characterizing the CO_2 adsorption cycle performance are defined as follows:

$$\text{Purity of } CO_2 = \frac{\int_{\text{Desorption}} F_{CO_2} dt}{\sum_i \int_{\text{Desorption}} F_i dt} \tag{4.30}$$

$$\text{Recovery of } CO_2 = \frac{\int_{\text{Desorption}} F_{CO_2} dt}{\int_{\text{Adsorption}} F_{CO_2} dt} \tag{4.31}$$

$$\text{Productivity of } CO_2 = \frac{\int_{\text{Desorption}} F_{CO_2} M_{CO_2} dt}{t_{cycle} M_s} \tag{4.32}$$

Due to the simplifications in the scaling analysis, the inlet and outlet CO_2 flow rates are obtained from the net adsorption uptake of the cycle, which still provides guidance for optimizing the performance from the perspective of overall trend. Fig. 4.2 illustrates the variation trends of CO_2 purity, recovery and productivity with ambient temperature. As the ambient temperature increases, all three parameters decrease, with the decline rate becoming increasingly larger. This indicates that the noticeable reduction in net uptake has a detrimental effect on the overall cycle performance.

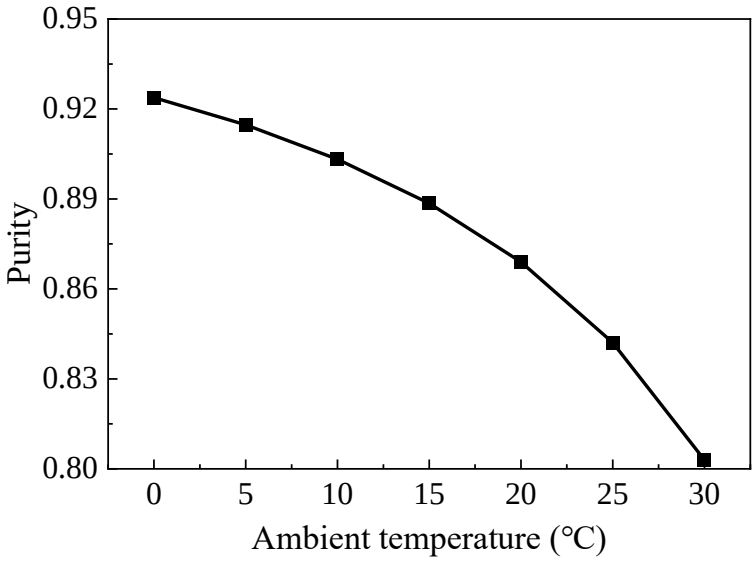
0.95
0.92
0.89
0.86
0.83
0.80
Purity
0
5
10
15
20
25
30
Ambient temperature (°C)

(a)

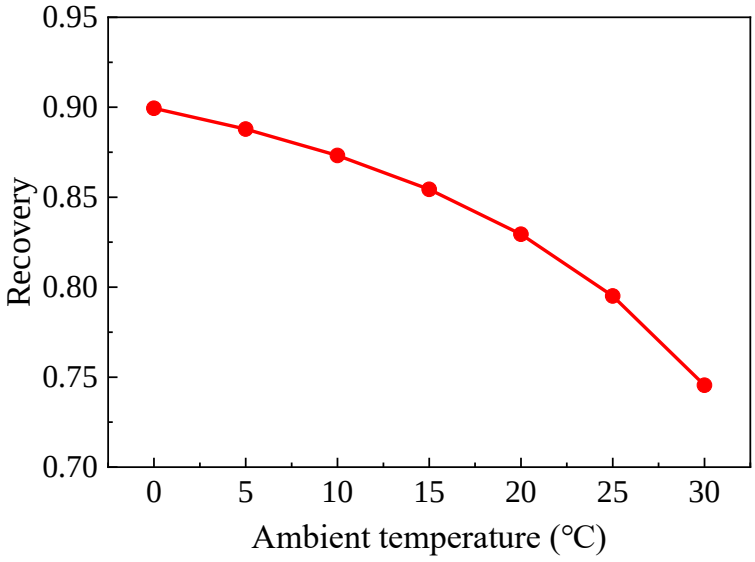
0.95
0.90
0.85
0.80
0.75
0.70
Recovery
0
5
10
15
20
25
30
Ambient temperature (°C)

(b)

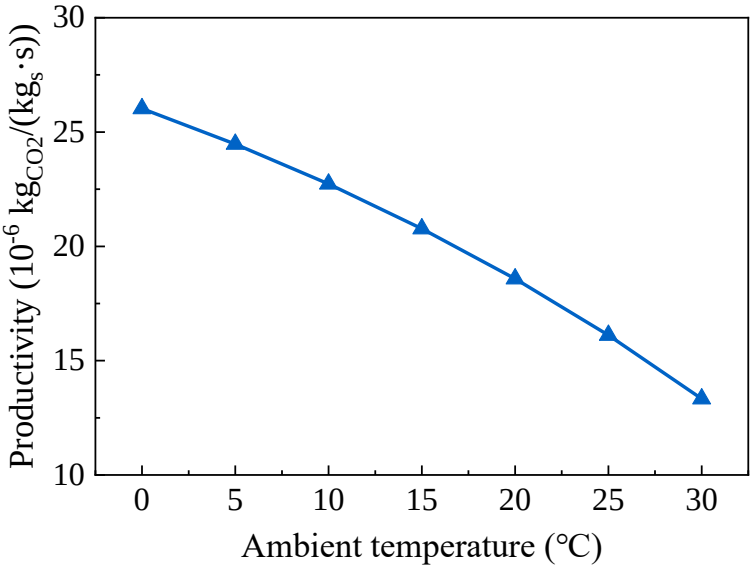

(c)

Fig. 4.2 Performance parameters versus ambient temperature: (a) Purity, (b) Recovery, (c) Productivity.

Fig. 4.3 shows the variation trends of CO_2 purity, recovery and productivity with respect to the HTF temperature at an HTF flow rate of 0.2 kg/s. In contrast to the influence of ambient temperature, an increase in the HTF temperature enhances all performance parameters. A higher HTF temperature reduces the minimum uptake, thereby indirectly improving the net uptake. Hence, it can be seen that under a fixed HTF flow rate, decreasing the ambient temperature and increasing the HTF temperature both contribute to improving the system performance.

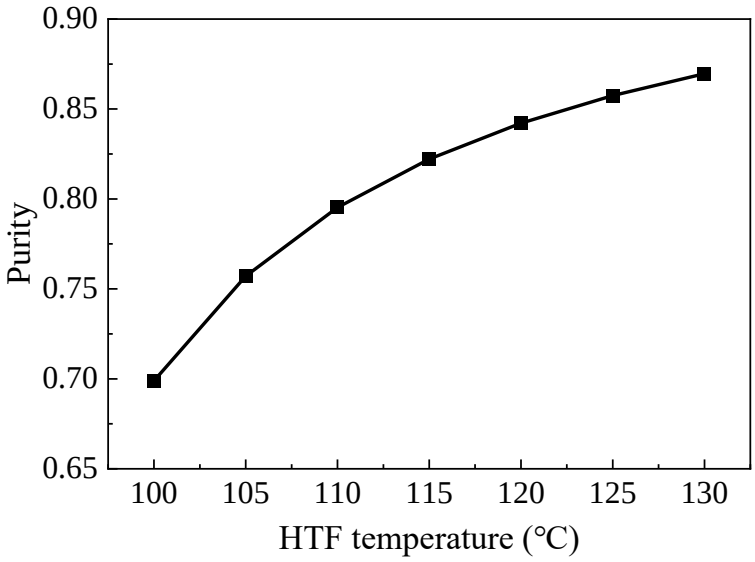
Purity
0.90
0.85
0.80
0.75
0.70
0.65
100
105
110
115
120
125
130
HTF temperature (°C)

(a)

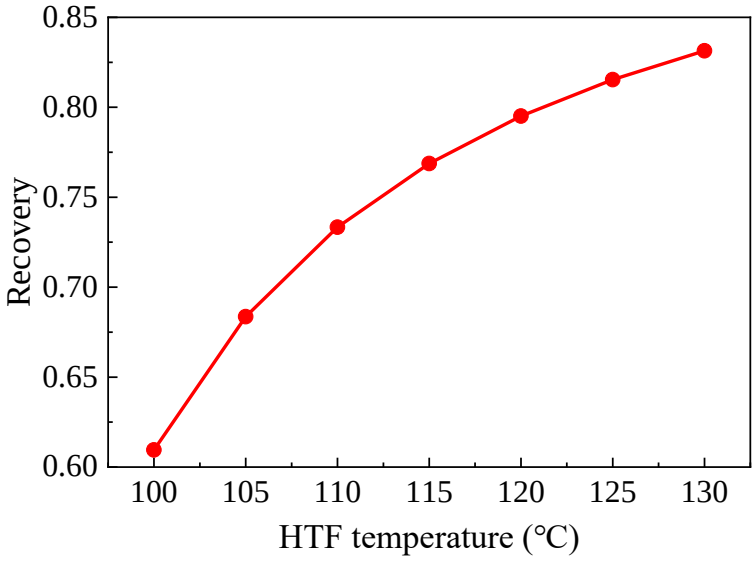
Recovery
0.85
0.80
0.75
0.70
0.65
0.60
100
105
110
115
120
125
130
HTF temperature (°C)

(b)

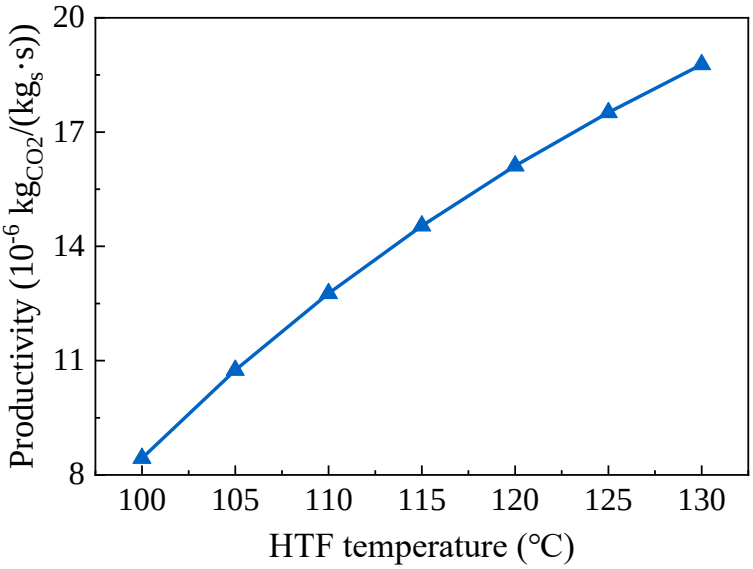

(c)

Fig. 4.3 Performance parameters versus HTF temperature: (a) Purity, (b) Recovery, (c) Productivity.

Figs. 4.4 and 4.5 elucidate the effects of the inlet velocity during the adsorption period and the HTF flow rate during the desorption period, respectively, on the CO_2 productivity. An increase in both the inlet velocity and the HTF flow rate contributes to enhancing the CO_2 productivity. Under the same net adsorption uptake, they respectively shorten the adsorption time and desorption time, thereby increasing the CO_2 capture capacity per unit time. However, it is noteworthy that an increase in the inlet velocity during adsorption may potentially reduce the CO_2 recovery due to the higher time proportion of the heat-removing phase.

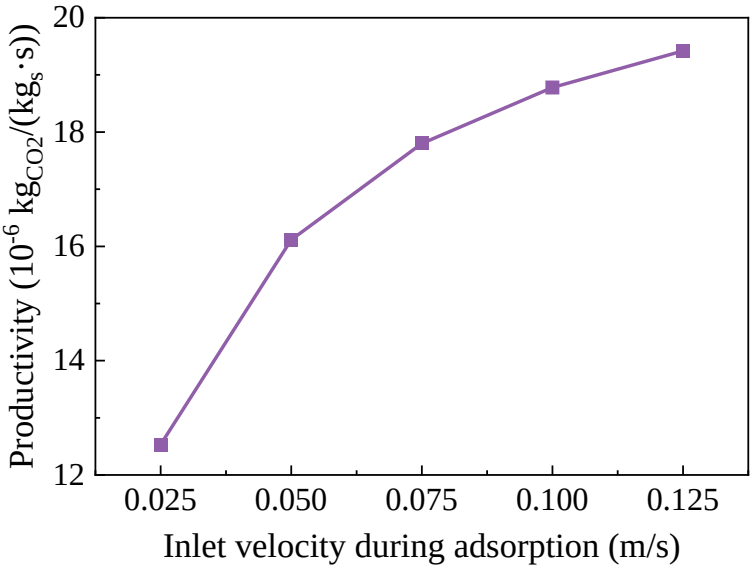

Fig. 4.4 Productivity versus inlet velocity during adsorption.

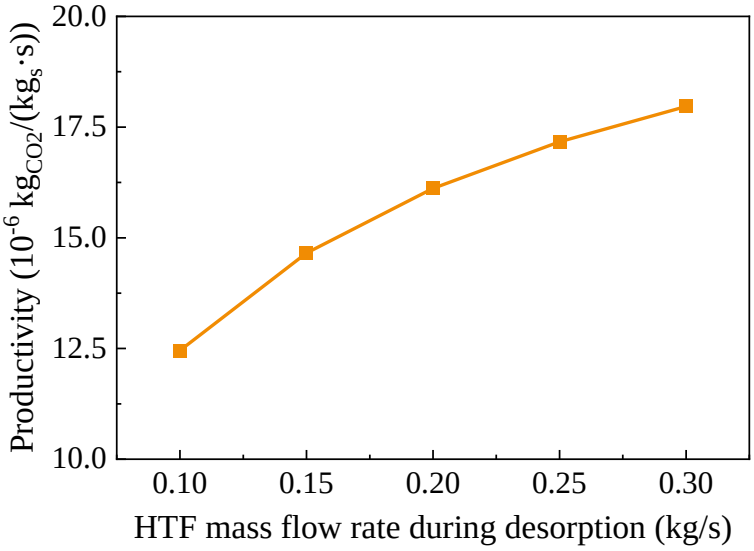

Fig. 4.5 Productivity versus HTF mass flow rate during desorption.

4.3 Performance analysis of AHT-TSA system

The AHT system can upgrade low-grade waste heat to an utilizable level, benefiting adsorption-based CO_2 capture. Integrating a heat storage tank allows the AHT system to provide stable temperature and flow output, precisely meeting the thermal demands of downstream applications. In this section, the TSA system coupled with AHT is further investigated, where the HTF flow rate is stabilized at the average output flow rate of AHT system. The corresponding system diagram is shown in Fig. 4.6. Besides CO_2 productivity, which characterizes the rate, the specific energy consumption (SEC) representing energy consumption is also considered.

$$\text{SEC of } CO_2 = \frac{Q_{de}}{\Delta q} \tag{4.33}$$

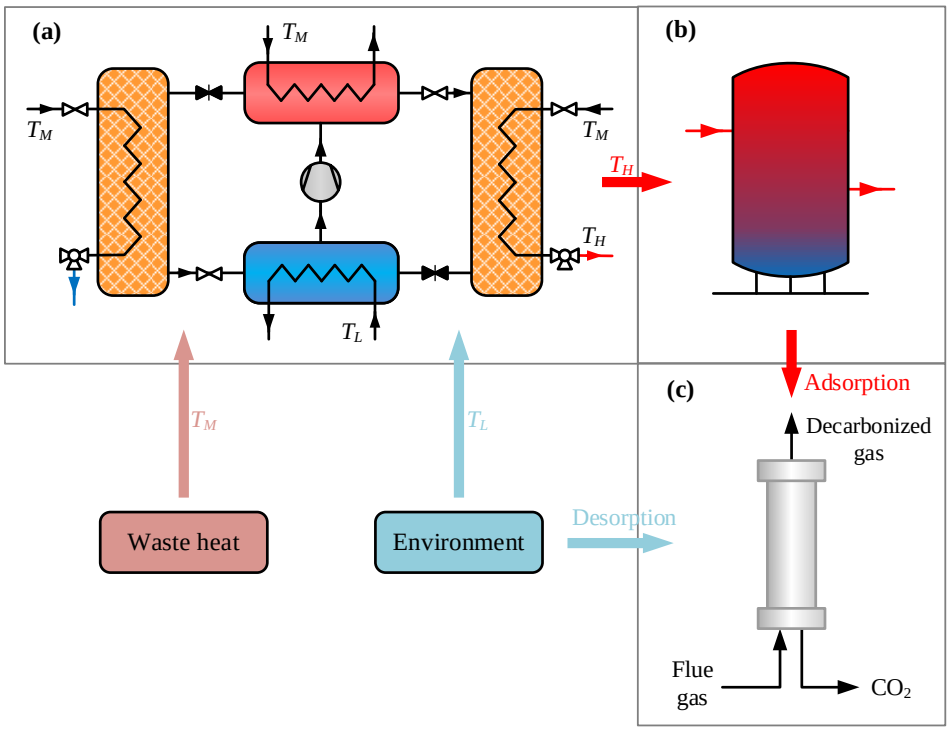

Fig. 4.6 Schematic diagram of AHT-TSA system: (a) AHT, (b) Heat storage tank, (c) TSA system.

Fig. 4.7 illustrates CO_2 productivity and SEC at different AHT target temperature lifts. As the target temperature lift increases, the productivity initially shows a significant rise from 20 ºC to 40 ºC. However, when the lift is increased from 40 ºC to 50 ºC, the productivity begins to slightly decline. Referring to the discussion on temperature lift limitations in Section 2.4, this temperature lift approaches the limit, leading to a degradation in system performance. Further optimization may be necessary to ensure the highest efficiency in CO_2 capture performance. Additionally, the SEC gradually decreases with increasing target temperature lift, from 6.47 MJ/kg_{CO2} down to 3.27 MJ/kg_{CO2}.

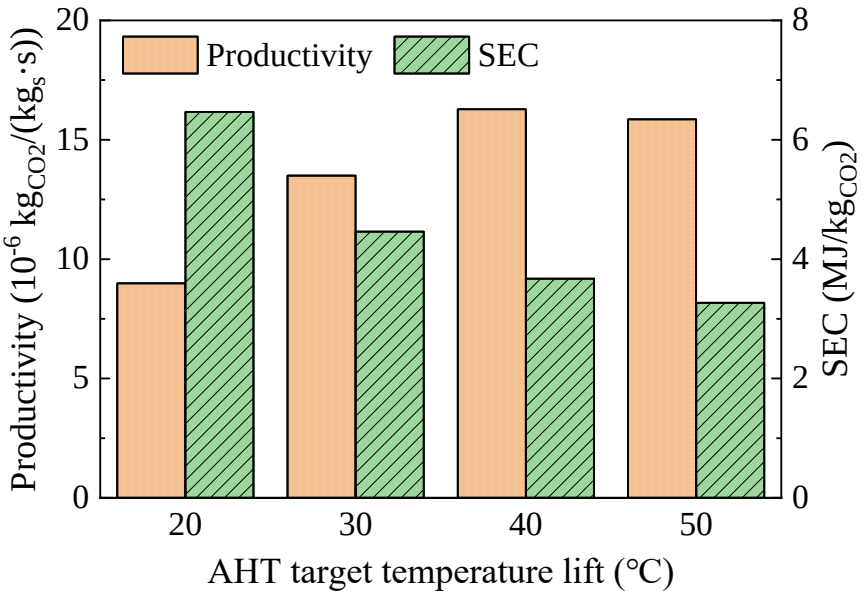

Fig. 4.7 CO_2 productivity and SEC at different AHT target temperature lifts.

Fig. 4.8 shows the effect of ambient temperature on the performance of the

coupled system. As the ambient temperature increases from 0 ºC to 30 ºC, the CO_2 productivity significantly decreases. Simultaneously, the SEC increases markedly, from 2.21 MJ/kg_{CO2} to 4.47 MJ/kg_{CO2}. According to the results in Section 2.4, the ambient temperature range of 0-30 ºC has almost no effect on the performance of the AHT; therefore, the primary impact here is on the net uptake of the TSA system. These results indicate that lower ambient temperatures help to enhance productivity and reduce energy consumption, which is significant for optimizing the performance of open CO_2 systems. In addition, waste heat used directly for desorption in the absence of AHT is also considered.

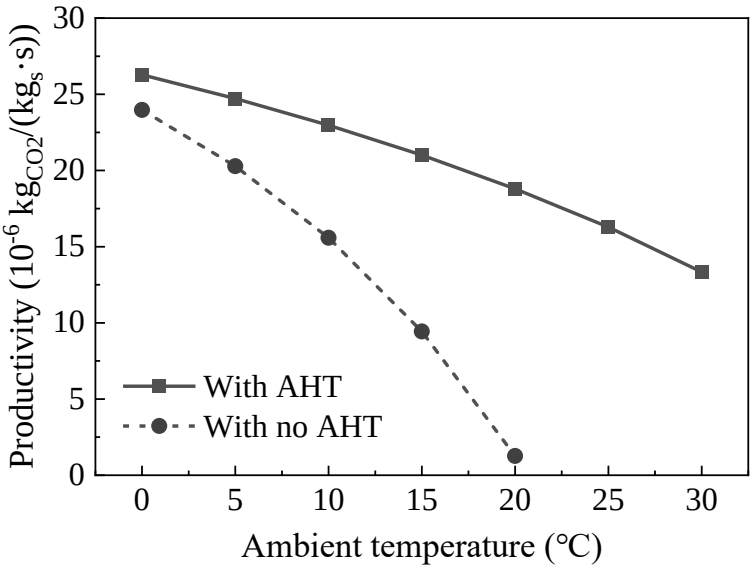

(a)

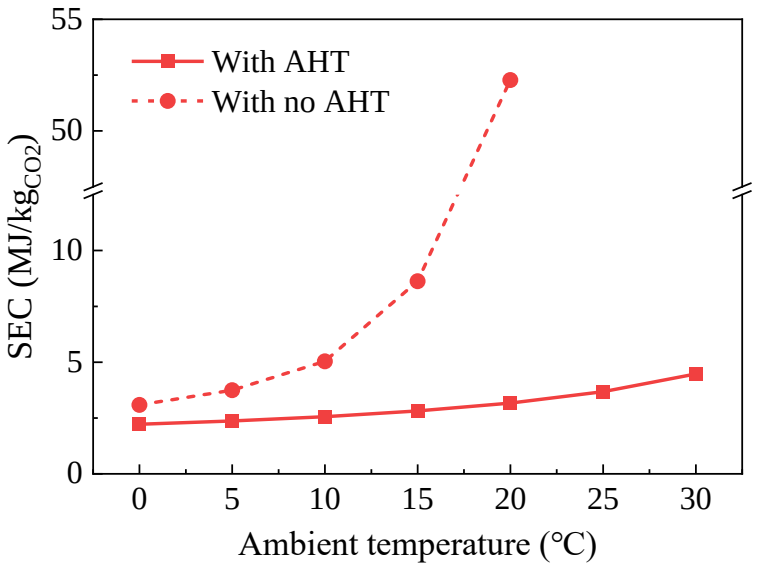

(b)

Fig. 4.8 (a) CO_2 productivity and (b) SEC versus ambient temperature.

Fig. 4.9 (a) shows the variation of CO_2 productivity with waste heat temperature, and (b) shows the variation of SEC with waste heat temperature. The results indicate that as the waste heat temperature increases from 70 °C to 90 °C, CO_2 productivity significantly increases while the SEC significantly decreases. This suggests that at the same temperature lift, increasing the waste heat temperature can effectively enhance the performance of the CO_2 adsorption system, increasing productivity and reducing energy consumption, which is of great importance for optimizing energy utilization.

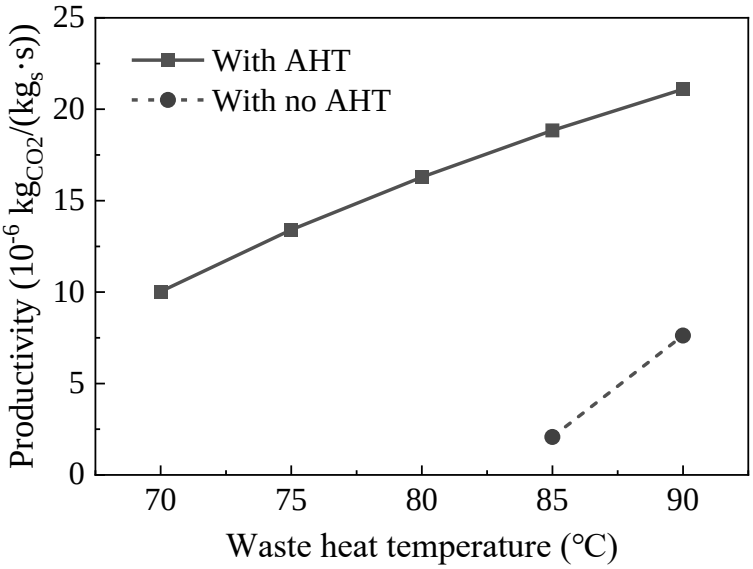

(a)

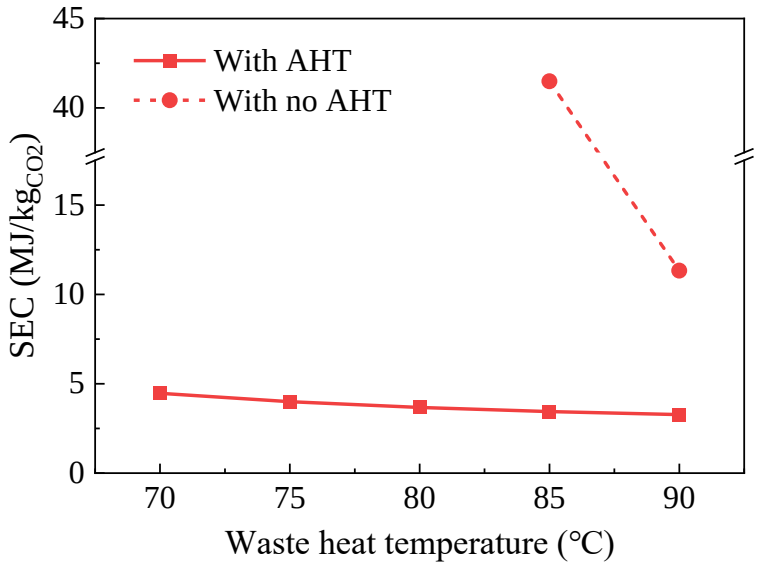

(b)

Fig. 4.9 (a) CO_2 productivity and (b) SEC versus waste heat temperature.

4.4 Conclusions

This chapter analyzed the performance of CO_2 temperature swing adsorption (TSA) system coupled with an adsorption heat transformer (AHT). Key findings include:

1. The integration of the AHT system with the TSA cycle significantly enhances the utilization of low-grade waste heat, elevating it to a more usable level. This is particularly beneficial for CO_2 adsorption processes where stable and controlled temperature outputs are crucial.

2. Increasing waste heat temperature from 70 ºC to 90 ºC boosts CO_2 productivity and reduces specific energy consumption (SEC), indicating better performance at higher temperatures.

3. Higher ambient temperatures (0 ºC to 30 ºC) decrease CO_2 productivity and increase SEC, showing lower temperatures favor better performance.

4. Optimizing AHT target temperature lifts can balance high CO_2 productivity with low energy consumption.

These findings demonstrate the potential of AHT-TSA system for effective waste heat recovery and CO_2 capture, supporting enhanced energy efficiency and sustainability.

Chapter 5 Conclusions and future prospects

5.1 Conclusions

This study has systematically explored the dynamic modeling of an LPJ-driven adsorption heat transformer (AHT) system and the scaling analysis of open carbon dioxide (CO_2) adsorption. The following key insights have been derived from the comprehensive investigations:

1. Enhanced understanding of AHT system through dynamic modeling: The dynamic models developed for the AHT system have provided deeper insights into the transient behaviors under varying operational conditions. These models have successfully captured the complex interplay between mass transfer dynamics and thermal response, thereby facilitating a more nuanced understanding of system performance.

2. Optimization of system performance: Through sensitivity analysis, critical parameters influencing the performance of the AHT system were identified, enabling targeted improvements. The optimization of these parameters has led to enhanced efficiency and stability of the system, thus promoting the effective utilization of low-grade waste heat.

3. Validity of scaling analysis: The scaling analysis has been meticulously validated through comparison with computational fluid dynamics (CFD) simulations,

demonstrating its robustness in predicting the operational behavior of the open CO_2 adsorption process. This validation underscores the utility of scaling analysis as a potent tool for preliminary assessments in the design and optimization of CO_2 adsorption system.

4. Contribution to low-grade waste heat upgrade and utilization: The study has contributed advancements to the field of low-grade waste heat recovery by demonstrating the feasibility and effectiveness of using an integrated AHT-TSA system for waste heat upgrade. The findings offer promising avenues for the deployment of such technologies in industrial applications, aiming to bolster energy efficiency and sustainability.

In conclusion, the findings not only enrich the existing academic field on adsorption technologies but also lay a solid foundation for future technological innovations in sustainable energy systems. The methodologies developed herein hold the potential to improve the efficiency of waste heat recovery processes, making a fractional contribution to the field of energy engineering.

5.2 Future prospects

The findings of this study pave the way for several promising research directions. Future studies could focus on integrating renewable energy sources with the AHT system to enhance its sustainability and efficiency. Additionally, expanding the application scope to include industrial scales with variable operational conditions could validate the adaptability and robustness of the developed models. Exploring advanced materials for adsorption and refining system design to optimize heat and

mass transfer processes would also be crucial. These endeavors will not only further the development of adsorption technologies but also contribute to global efforts in energy conservation and emission reduction.

References

[1] Clausse M, Merel J, Meunier F. Numerical parametric study on CO2 capture by indirect thermal swing adsorption. Int J Greenh Gas Control 2011;5:1206–13.

[2] Forman C, Muritala IK, Pardemann R, Meyer B. Estimating the global waste heat potential. Renew Sustain Energy Rev 2016;57:1568–79. https://doi.org/10.1016/j.rser.2015.12.192.

[3] Lal R. Land use changes and fluctuating climate. Soil Hydrol Chang Clim 2022.

[4] Dimitrov RS. The Paris agreement on climate change: Behind closed doors. Glob Environ Polit 2016;16:1–11.

[5] Friedrichs J. The future is not what it used to be: Climate change and energy scarcity. MIT Press; 2013.

[6] Wang L, Patel PL, Yu S, Liu B, McLeod J, Clarke LE, et al. Win–win strategies to promote air pollutant control policies and non-fossil energy target regulation in China. Appl Energy 2016;163:244–53.

[7] Agarwal S, Tyagi M, R. K. Garg. Circular Economy Reinforcement to Diminish GHG Emissions: A grey DEMATEL Approach. Evergreen 2023;10:389–403. https://doi.org/10.5109/6781099.

[8] Wu B, Wang Z, Tian Y, Zheng S. The impact of industrial transformation and upgrading on fossil energy elasticity in China. J Clean Prod 2024;434:140287.

[9] Waste Heat Recovery: Technology and Opportunities in U.S. Industry. Department of Energy; 2008.

[10] Lu H, Price L, Zhang Q. Capturing the invisible resource: Analysis of waste heat potential in Chinese industry. Appl Energy 2016;161:497–511.

[11] Chen Y, Li C, Zeng Z. Proposal and comprehensive analysis of an innovative steam generation system by deep recovery of low-grade waste heat. J Clean Prod 2021;310:127509.

[12] Lestari NA. Reduction of CO_2 Emission by Integrated Biomass Gasification-Solid Oxide Fuel Cell Combined with Heat Recovery and in-situ CO_2 Utilization. Evergreen 2019;6:254–61. https://doi.org/10.5109/2349302.

[13] Verma K, Prakash O, A.S. Paikra, Tiwari P. Photovoltaic Panel Integration Using Phase Change Material (PCM): Review. Evergreen 2023;10:444–53. https://doi.org/10.5109/6782147.

[14] Brückner S, Liu S, Miró L, Radspieler M, Cabeza LF, Lävemann E. Industrial waste heat recovery technologies: An economic analysis of heat transformation technologies. Appl Energy 2015;151:157–67. https://doi.org/10.1016/j.apenergy.2015.01.147.

[15] Weiss W. Solar Heat for Industrial Applications: Potential, Framework Conditions and Built Examples. Inst Sustain Technol AEE Austria Httpwww Sustain Vic Gov Auresourcesdocumentssolarheatforindustrial Process Pdf Retrieved Oct 2012 2012.

[16] Klein P. Fundamentals of plastics thermoforming. Springer Nature; 2022.

[17] Mukhopadhyay R, De SK, Chakraborty S. Effect of vulcanization temperature and vulcanization systems on the structure and properties of natural rubber vulcanizates. Polymer 1977;18:1243–9.

[18] Hanshik C, Jeong H, Jeong K-W, Choi S-H. Improved productivity of the MSF (multi-stage flashing) desalination plant by increasing the TBT (top brine temperature). Energy 2016;107:683–92.

[19] Uusitalo A, Turunen-Saaresti T, Honkatukia J, Tiainen J, Jaatinen-Värri A. Numerical analysis of working fluids for large scale centrifugal compressor driven cascade heat pumps upgrading waste heat. Appl Energy 2020;269:115056.

[20] van der Pal M, Wemmers A, Smeding S, de Boer R. Technical and economical feasibility of the hybrid adsorption compression heat pump concept for industrial applications. Appl Therm Eng 2013;61:837–40. https://doi.org/10.1016/j.applthermaleng.2013.04.048.

[21] Dong L, Tong H, Liu X, Li M, Niu J. Comprehensive analysis of modified carbon dioxide heat pump systems and determination of operating schemes for residential heating: A multi-objective optimization approach. Energy Convers Manag 2024;306:118272.

[22] Hastürk E, Ernst S-J, Janiak C. Recent advances in adsorption heat transformation focusing on the development of adsorbent materials. Curr Opin Chem Eng 2019;24:26–36. https://doi.org/10.1016/j.coche.2018.12.011.

[23] Ma Z, Bao H, Roskilly AP. Performance analysis of ultralow grade waste heat upgrade using absorption heat transformer. Appl Therm Eng 2016;101:350–61.

https://doi.org/10.1016/j.applthermaleng.2016.02.002.

[24] Zhang X, Wu J, Li Z. Irreversibility characterization and analysis of coupled heat and mass transfer processes in an absorption system. Int J Heat Mass Transf 2019;133:1121–33. https://doi.org/10.1016/j.ijheatmasstransfer.2019.01.003.

[25] Rivera W, Best R, Cardoso MJ, Romero RJ. A review of absorption heat transformers. Appl Therm Eng 2015;91:654–70. https://doi.org/10.1016/j.applthermaleng.2015.08.021.

[26] Liu X, Hu Y, Wang Q, Yao L, Li M. Energetic, environmental and economic comparative analyses of modified transcritical CO2 heat pump system to replace R134a system for home heating. Energy 2021;229:120544.

[27] Richter M, Bouché M, Linder M. Heat transformation based on CaCl2/H2O–Part A: Closed operation principle. Appl Therm Eng 2016;102:615–21.

[28] Bouché M, Richter M, Linder M. Heat transformation based on CaCl2/H2O–Part B: Open operation principle. Appl Therm Eng 2016;102:641–7.

[29] Xu Z, Wang R. Absorption heat pump for waste heat reuse: current states and future development. Front Energy 2017;11:414–36.

[30] Naseem M, Park S, Lee S. Experimental and theoretical analysis of a trigeneration system consisting of adsorption chiller and high temperature PEMFC. Energy Convers Manag 2022;251:114977. https://doi.org/10.1016/j.enconman.2021.114977.

[31] Naseem M, Son N, Lee YD. Dynamic simulation and exergy analysis of adsorption chiller powered by low-grade waste heat from a fuel-cell system: Effect of multibed configuration and time constant. Energy Convers Manag 2023;293:117453. https://doi.org/10.1016/j.enconman.2023.117453.

[32] Liu YM, Yuan ZX, Wen X, Du CX. Evaluation on performance of solar adsorption cooling of silica gel and SAPO-34 zeolite. Appl Therm Eng 2021;182:116019. https://doi.org/10.1016/j.applthermaleng.2020.116019.

[33] Liu Y, Yuan Z, Liu Z. Experimental performance of a small solar system for adsorption cooling in summer and heating in winter. J Renew Sustain Energy 2022;14.

[34] Xu J, Pan Q, Zhang W, Liu Z, Wang R, Ge T. Design and experimental study on a hybrid adsorption refrigeration system using desiccant coated heat exchangers for

efficient energy utilization. Renew Sustain Energy Rev 2022;169. https://doi.org/10.1016/j.rser.2022.112890.

[35] Xu J, Zhang W, Liu Z, Pan Q, Wang R, Ge T. Energy and exergy analyses of a hybrid adsorption refrigeration system for simultaneous production of cold water and dry air. Energy Convers Manag 2023;286:117088. https://doi.org/10.1016/j.enconman.2023.117088.

[36] Xu J, Huang M, Liu Z, Pan Q, Wang R, Ge T. Performance evaluation of a high-efficient hybrid adsorption refrigeration system for ultralow-grade heat utilization. Energy 2024;288:129870. https://doi.org/10.1016/j.energy.2023.129870.

[37] Thu K, Saha BB, Chua KJ, Ng KC. Performance investigation of a waste heat-driven 3-bed 2-evaporator adsorption cycle for cooling and desalination. Int J Heat Mass Transf 2016;101:1111–22. https://doi.org/10.1016/j.ijheatmasstransfer.2016.05.127.

[38] Thu K, Saha BB, Mitra S, Chua KJ. Modeling and Simulation of Mass Recovery Process in Adsorption System for Cooling and Desalination. Energy Procedia, vol. 105, 2017, p. 2004–9. https://doi.org/10.1016/j.egypro.2017.03.574.

[39] AL-Dadah R, Mahmoud S, Elsayed E, Youssef P, Al-Mousawi F. Metal-organic framework materials for adsorption heat pumps. Energy 2020;190:116356. https://doi.org/10.1016/j.energy.2019.116356.

[40] Li G, Xue B, He X, Chen T, Wei X. Superhydrophobic Surface-modified zeolite to regulate the migration of nonadsorbed liquid water in an Open-loop adsorption heat pump. Appl Therm Eng 2022;215:118929.

[41] Li G, Qian S, Lee H, Hwang Y, Radermacher R. Experimental investigation of energy and exergy performance of short term adsorption heat storage for residential application. Energy 2014;65:675–91. https://doi.org/10.1016/j.energy.2013.12.017.

[42] Schreiber H, Graf S, Lanzerath F, Bardow A. Adsorption thermal energy storage for cogeneration in industrial batch processes: Experiment, dynamic modeling and system analysis. Appl Therm Eng 2015;89:485–93. https://doi.org/10.1016/j.applthermaleng.2015.06.016.

[43] Schreiber H, Lanzerath F, Reinert C, Grüntgens C, Bardow A. Heat lost or stored: Experimental analysis of adsorption thermal energy storage. Appl Therm Eng 2016;106:981–91. https://doi.org/10.1016/j.applthermaleng.2016.06.058.

[44] Chandra I, Patwardhan VS. Theoretical studies on adsorption heat transformer

using zeolite-water vapour pair. Heat Recovery Syst CHP 1990;10:527–37. https://doi.org/10.1016/0890-4332(90)90203-V.

[45] Aristov YI. Adsorptive transformation of ambient heat: A new cycle. Appl Therm Eng 2017;124:521–4. https://doi.org/10.1016/j.applthermaleng.2017.06.051.

[46] Tokarev MM, Gordeeva LG, Grekova AD, Aristov YI. Adsorption cycle "heat from cold" for upgrading the ambient heat: The testing a lab-scale prototype with the composite sorbent CaClBr/silica. Appl Energy 2018;211:136–45. https://doi.org/10.1016/j.apenergy.2017.11.015.

[47] Tokarev MM, Gordeeva LG, Shkatulov AI, Aristov YI. Testing the lab-scale "Heat from Cold" prototype with the "LiCl/silica – methanol" working pair. Energy Convers Manag 2018;159:213–20. https://doi.org/10.1016/j.enconman.2017.12.099.

[48] Engelpracht M, Gibelhaus A, Seiler J, Graf S, Nasruddin N, Bardow A. Upgrading Waste Heat from 90 to 110 °C: The Potential of Adsorption Heat Transformation. Energy Technol 2021;9:2000643. https://doi.org/10.1002/ente.202000643.

[49] Saren S, Mitra S, Miyazaki T, Ng KC, Thu K. A novel hybrid adsorption heat transformer – multi-effect distillation (AHT-MED) system for improved performance and waste heat upgrade. Appl Energy 2022;305:117744. https://doi.org/10.1016/j.apenergy.2021.117744.

[50] Saren S, Mitra S, Miksik F, Miyazaki T, Ng KC, Thu K. Impacts of the internal heat recovery scheme on the performance of an adsorption heat transformer cycle for temperature upgrade. Int Commun Heat Mass Transf 2023;144:106774. https://doi.org/10.1016/j.icheatmasstransfer.2023.106774.

[51] Yu C-H, Huang C-H, Tan C-S. A review of CO2 capture by absorption and adsorption. Aerosol Air Qual Res 2012;12:745–69.

[52] Skjervold VT, Mondino G, Riboldi L, Nord LO. Investigation of control strategies for adsorption-based CO2 capture from a thermal power plant under variable load operation. Energy 2023;268:126728. https://doi.org/10.1016/j.energy.2023.126728.

[53] Zhang ZX, Xu HJ. Thermodynamic modeling on multi-stage vacuum-pressure swing adsorption (VPSA) for direct air carbon capture with extreme dilute carbon dioxide. Energy 2023;276:127550. https://doi.org/10.1016/j.energy.2023.127550.

[54] Liu L, Kubota M, Li J, Kimura H, Bai Y, Wu R, et al. Comparative study on the

water uptake kinetics and dehumidification performance of silica gel and aluminophosphate zeolites coatings. Energy 2022;242:122957. https://doi.org/10.1016/j.energy.2021.122957.

[55] Yadav L, Ashutosh Kumar Verma, Dabra V, Yadav A. Performance Comparison of Different Desiccant Material Based Wheels for Air Conditioning Application. Evergreen 2023;10:912–23. https://doi.org/10.5109/6792886.

[56] Strong C, Carrier Y, Handan Tezel F. Experimental optimization of operating conditions for an open bulk-scale silica gel/water vapour adsorption energy storage system. Appl Energy 2022;312:118533. https://doi.org/10.1016/j.apenergy.2022.118533.

[57] Djubaedah E, Wulandari A, Nasruddin, Krisnandi K. Surface Area Modification of Natural Zeolite Through NaCl Counterbalanced Treatment to Apply in Adsorption Heat Storage System. Evergreen 2020;7:26–31. https://doi.org/10.5109/2740938.

[58] Yue L, Xia Q, Wang L, Wang L, DaCosta H, Yang J, et al. CO2 adsorption at nitrogen-doped carbons prepared by K2CO3 activation of urea-modified coconut shell. J Colloid Interface Sci 2018;511:259–67.

[59] Kulkarni AR, Sholl DS. Analysis of Equilibrium-Based TSA Processes for Direct Capture of CO_2 from Air. Ind Eng Chem Res 2012;51:8631–45. https://doi.org/10.1021/ie300691c.

[60] Zhao R, Liu L, Zhao L, Deng S, Li S, Zhang Y, et al. Thermodynamic exploration of temperature vacuum swing adsorption for direct air capture of carbon dioxide in buildings. Energy Convers Manag 2019;183:418–26. https://doi.org/10.1016/j.enconman.2019.01.009.

[61] Darunte LA, Oetomo AD, Walton KS, David S. Sholl, Jones CW. Direct Air Capture of CO_2 Using Amine Functionalized MIL-101(Cr). ACS Sustain Chem Eng 2016;4:5761–8. https://doi.org/10.1021/acssuschemeng.6b01692.

[62] Elfving J, Bajamundi C, Kauppinen J, Sainio T. Modelling of equilibrium working capacity of PSA, TSA and TVSA processes for CO2 adsorption under direct air capture conditions. J CO2 Util 2017;22:270–7.

[63] Haghpanah R, Majumder A, Nilam R, Rajendran A, Farooq S, Karimi IA, et al. Multiobjective Optimization of a Four-Step Adsorption Process for Postcombustion CO_2 Capture Via Finite Volume Simulation. Ind Eng Chem Res 2013;52:4249–65. https://doi.org/10.1021/ie302658y.

[64] Qasem NAA, Ben-Mansour R. Energy and productivity efficient vacuum pressure swing adsorption process to separate CO2 from CO2/N2 mixture using Mg-MOF-74: A CFD simulation. Appl Energy 2018;209:190–202. https://doi.org/10.1016/j.apenergy.2017.10.098.

[65] Liu B, Lian Y, Li S, Deng S, Zhao L, Chen B, et al. Experimental investigation on separation and energy-efficiency performance of temperature swing adsorption system for CO2 capture. Sep Purif Technol 2019;227:115670. https://doi.org/10.1016/j.seppur.2019.06.008.

[66] Wu K, Deng S, Li S, Zhao R, Yuan X, Zhao L. Preliminary experimental study on the performance of CO2 capture prototype based on temperature swing adsorption (TSA). Carbon Capture Sci Technol 2022;2:100035. https://doi.org/10.1016/j.ccst.2022.100035.

[67] Wang L, Liu Z, Li P, Yu J, Rodrigues AE. Experimental and modeling investigation on post-combustion carbon dioxide capture using zeolite 13X-APG by hybrid VTSA process. Chem Eng J 2012;197:151–61. https://doi.org/10.1016/j.cej.2012.05.017.

[68] Ben-Mansour R, Qasem NAA. An efficient temperature swing adsorption (TSA) process for separating CO2 from CO2/N2 mixture using Mg-MOF-74. Energy Convers Manag 2018;156:10–24. https://doi.org/10.1016/j.enconman.2017.11.010.

[69] Khurana M, Farooq S. Simulation and optimization of a 6-step dual-reflux VSA cycle for post-combustion CO2 capture. Chem Eng Sci 2016;152:507–15. https://doi.org/10.1016/j.ces.2016.06.033.

[70] Li S, Deng S, Zhao R, Zhao L, Xu W, Yuan X, et al. Entropy analysis on energy-consumption process and improvement method of temperature/vacuum swing adsorption (TVSA) cycle. Energy 2019;179:876–89. https://doi.org/10.1016/j.energy.2019.05.027.

[71] Plaza MG, Rubiera F. Evaluation of a novel multibed heat-integrated vacuum and temperature swing adsorption post-combustion CO2 capture process. Appl Energy 2019;250:916–25. https://doi.org/10.1016/j.apenergy.2019.05.079.

[72] Hedin N, Andersson L, Bergström L, Yan J. Adsorbents for the post-combustion capture of CO2 using rapid temperature swing or vacuum swing adsorption. Appl Energy 2013;104:418–33. https://doi.org/10.1016/j.apenergy.2012.11.034.

[73] Sinha A, Darunte LA, Jones CW, Realff MJ, Kawajiri Y. Systems Design and

Economic Analysis of Direct Air Capture of CO_2 through Temperature Vacuum Swing Adsorption Using MIL-101(Cr)-PEI-800 and mmen-Mg_2 (dobpdc) MOF Adsorbents. Ind Eng Chem Res 2017;56:750–64. https://doi.org/10.1021/acs.iecr.6b03887.

[74] Ben-Mansour R, Qasem NAA. An efficient temperature swing adsorption (TSA) process for separating CO2 from CO2/N2 mixture using Mg-MOF-74. Energy Convers Manag 2018;156:10–24. https://doi.org/10.1016/j.enconman.2017.11.010.

[75] Lian Y, Deng S, Li S, Guo Z, Zhao L, Yuan X. Numerical analysis on CO2 capture process of temperature swing adsorption (TSA): Optimization of reactor geometry. Int J Greenh Gas Control 2019;85:187–98. https://doi.org/10.1016/j.ijggc.2019.03.029.

[76] Chen L, Deng S, Zhao R, Zhu Y, Zhao L, Li S. Temperature swing adsorption for CO2 capture: Thermal design and management on adsorption bed with single-tube/three-tube internal heat exchanger. Appl Therm Eng 2021;199:117538. https://doi.org/10.1016/j.applthermaleng.2021.117538.

[77] Zhu X, Ge T, Yang F, Wang R. Design of steam-assisted temperature vacuum-swing adsorption processes for efficient CO2 capture from ambient air. Renew Sustain Energy Rev 2021;137:110651. https://doi.org/10.1016/j.rser.2020.110651.

[78] Saren S, Mishra VK, Thu K, Mitra S. Scaling analysis of large pressure jump driven adsorption of water vapour in columnar porous silica gel bed. Int Commun Heat Mass Transf 2022;135:106101. https://doi.org/10.1016/j.icheatmasstransfer.2022.106101.

[79] Tokarev MM, Zlobin AA, Aristov YuI. A new version of the large pressure jump (T-LPJ) method for dynamic study of pressure-initiated adsorptive cycles for heat storage and transformation. Energy 2019;179:542–8. https://doi.org/10.1016/j.energy.2019.04.164.

[80] Shapiro AH. The dynamics and thermodynamics of compressible fluid flow. N Y Ronald Press 1953.

[81] Co C. Flow of Fluids Through Valves, Fittings, and Pipe. Crane Company; 1988.

[82] Dai Y, Wang J, Gao L. Parametric optimization and comparative study of organic Rankine cycle (ORC) for low grade waste heat recovery. Energy Convers Manag 2009;50:576–82. https://doi.org/10.1016/j.enconman.2008.10.018.

[83] Mittal H, Al Alili A, Alhassan SM, Susantyoko RA. Zeolites and superporous

hydrogels-based hybrid composites as solid desiccants to capture water vapors from humid air. Microporous Mesoporous Mater 2022;342:112116.

[84] El-Sharkawy II, AbdelMeguid H, Saha BB. Potential application of solar powered adsorption cooling systems in the Middle East. Appl Energy 2014;126:235–45. https://doi.org/10.1016/j.apenergy.2014.03.092.

[85] Sun B, Chakraborty A. Thermodynamic formalism of water uptakes on solid porous adsorbents for adsorption cooling applications. Appl Phys Lett 2014;104.

[86] Wei Benjamin Teo H, Chakraborty A, Fan W. Improved adsorption characteristics data for AQSOA types zeolites and water systems under static and dynamic conditions. Microporous Mesoporous Mater 2017;242:109–17. https://doi.org/10.1016/j.micromeso.2017.01.015.

[87] Youssef PG, Mahmoud SM, AL-Dadah RK. Performance analysis of four bed adsorption water desalination/refrigeration system, comparison of AQSOA-Z02 to silica-gel. Desalination 2015;375:100–7. https://doi.org/10.1016/j.desal.2015.08.002.

[88] Alsaman AS, Ibrahim EMM, Ahmed MS, Farid AM, Ali ES, Askalany AA. Experimental investigation of innovative composite Maxsorb III adsorbent for cooling and water desalination. J Clean Prod 2023;418:138047. https://doi.org/10.1016/j.jclepro.2023.138047.

[89] Selvakumar P, Somasundaram P, Thangavel P. Performance study on evacuated tube solar collector using therminol D-12 as heat transfer fluid coupled with parabolic trough. Energy Convers Manag 2014;85:505–10. https://doi.org/10.1016/j.enconman.2014.05.069.

[90] Bashir AI, Everts M, Bennacer R, Meyer JP. Single-phase forced convection heat transfer and pressure drop in circular tubes in the laminar and transitional flow regimes. Exp Therm Fluid Sci 2019;109:109891. https://doi.org/10.1016/j.expthermflusci.2019.109891.

[91] Gnielinski V. New equations for heat and mass transfer in turbulent pipe and channel flow. Int Chem Eng 1976;16:359–67.

[92] Saren S, Mitra S, Miksik F, Miyazaki T, Ng KC, Thu K. Investigating maximum temperature lift potential of the adsorption heat transformer cycle using IUPAC classified isotherms. Int J Heat Mass Transf 2024;225:125384. https://doi.org/10.1016/j.ijheatmasstransfer.2024.125384.

[93] Saloux E, Candanedo J. Modelling stratified thermal energy storage tanks using an advanced flowrate distribution of the received flow. Appl Energy 2019;241:34–45.

[94] Zeng Z, Grigg R. A criterion for non-Darcy flow in porous media. Transp Porous Media 2006;63:57–69.

[95] Ben-Mansour R, Abuelyamen A, Qasem NAA. Thermal design and management towards high capacity CO2 adsorption systems. Energy Convers Manag 2020;212:112796. https://doi.org/10.1016/j.enconman.2020.112796.

[96] Mohammed RH, Mesalhy O, Elsayed ML, Chow LC. Novel compact bed design for adsorption cooling systems: Parametric numerical study. Int J Refrig 2017;80:238–51. https://doi.org/10.1016/j.ijrefrig.2017.04.028.

[97] Dantas TLP, Luna FMT, Silva IJ, Torres AEB, de Azevedo DCS, Rodrigues AE, et al. Carbon dioxide–nitrogen separation through pressure swing adsorption. Chem Eng J 2011;172:698–704. https://doi.org/10.1016/j.cej.2011.06.037.

[98] Farooq S, Ruthven DM. Heat effects in adsorption column dynamics. 2. Experimental validation of the one-dimensional model. Ind Eng Chem Res 1990;29:1084–90. https://doi.org/10.1021/ie00102a020.

[99] Toth J. State equation of the solid-gas interface layers. Acta Chim Hung 1971;69:311–28.

[100] Dantas TLP, Luna FMT, Silva Jr IJ, Torres AEB, de Azevedo DCS, Rodrigues AE, et al. Modeling of the fixed - bed adsorption of carbon dioxide and a carbon dioxide - nitrogen mixture on zeolite 13X. Braz J Chem Eng 2011;28:533–44. https://doi.org/10.1590/S0104-66322011000300018.

[101] Ergun S. Fluid flow through packed columns. Chem Eng Prog 1952;48:89.

[102] Pang M, Zhang T, Ji X, Wu J, Song S. Measurement of the coefficient of seepage characteristics in pore-crushed coal bodies around gas extraction boreholes. Energy 2022;254:124276. https://doi.org/10.1016/j.energy.2022.124276.

[103] Ansys Fluent 2020. https://www.ansys.com/products/fluids/ansys-fluent.

[104] Zhang J, Webley PA, Xiao P. Effect of process parameters on power requirements of vacuum swing adsorption technology for CO2 capture from flue gas. Energy Convers Manag 2008;49:346–56. https://doi.org/10.1016/j.enconman.2007.06.007.

[105] Mulgundmath VP, Jones RA, Tezel FH, Thibault J. Fixed bed adsorption for the removal of carbon dioxide from nitrogen: Breakthrough behaviour and modelling

for heat and mass transfer. Sep Purif Technol 2012;85:17–27. https://doi.org/10.1016/j.seppur.2011.07.038.

[106] Wang S, Li Y, Li Z. Fast Adsorption Kinetics of CO $_2$ on Solid Amine Sorbent Measured Using Microfluidized Bed Thermogravimetric Analysis. Ind Eng Chem Res 2020;59:6855–66. https://doi.org/10.1021/acs.iecr.9b05386.

[107] Wang X, Chen L, Guo Q. Development of hybrid amine-functionalized MCM-41 sorbents for CO2 capture. Chem Eng J 2015;260:573–81. https://doi.org/10.1016/j.cej.2014.08.107.

[108] SIDABUTAR R, IRIANY MST. Adsorption-Desorption System For CO2 Removal In Biogas Using Natural Zeolite-Based Adsorbent. J Eng Sci Technol 2018;13:3058–70.

[109] Susarla N, Haghpanah R, Karimi IA, Farooq S, Rajendran A, Tan LSC, et al. Energy and cost estimates for capturing CO2 from a dry flue gas using pressure/vacuum swing adsorption. Chem Eng Res Des 2015;102:354–67. https://doi.org/10.1016/j.cherd.2015.06.033.

[110] Gardner RH, O'neill RV, Mankin JB, Carney JH. A comparison of sensitivity analysis and error analysis based on a stream ecosystem model. Ecol Model 1981;12:173–90.

[111] Jørgensen SE, Bendoricchio G. Fundamentals of ecological modelling. vol. 21. Elsevier; 2001.

[112] Lin J, Thu K, Karthik S, Shahzad MW, Wang R, Chua KJ. Understanding the transient behavior of the dew point evaporative cooler from the first and second law of thermodynamics. Energy Convers Manag 2021;244:114471.

[113] Wang Y, Chen H, Wang H, Xu G, Lei J, Huang Q, et al. A novel carbon dioxide capture system for a cement plant based on waste heat utilization. Energy Convers Manag 2022;257:115426. https://doi.org/10.1016/j.enconman.2022.115426.

[114] Nandhini R, Sivaprakash B, Rajamohan N. Waste heat recovery at low temperature from heat pumps, power cycles and integrated systems–Review on system performance and environmental perspectives. Sustain Energy Technol Assess 2022;52:102214.

[115] Li A, Thu K, Ismail AB, Ng KC. A heat transfer correlation for transient vapor uptake of powdered adsorbent embedded onto the fins of heat exchangers. Appl Therm Eng 2016;93:668–77.

https://doi.org/10.1016/j.applthermaleng.2015.09.057.

[116] Wakao N, Funazkri T. Effect of fluid dispersion coefficients on particle-to-fluid mass transfer coefficients in packed beds: Correlation of sherwood numbers. Chem Eng Sci 1978;33:1375–84. https://doi.org/10.1016/0009-2509(78)85120-3.

[117] Yang RT. Gas separation by adsorption processes. vol. 1. World Scientific; 1997.

[118] Hirschfelder JO, Curtiss CF, Bird RB. Molecular Theory of Gases and Liquids. Phys Today 1955;8:17–17. https://doi.org/10.1063/1.3061949.

[119] Park Y, Ju Y, Park D, Lee C-H. Adsorption equilibria and kinetics of six pure gases on pelletized zeolite 13X up to 1.0 MPa: CO 2 , CO, N 2 , CH 4 , Ar and H 2. Chem Eng J 2016;292:348–65. https://doi.org/10.1016/j.cej.2016.02.046.

[120] Chung K, Park D, Kim K-M, Lee C-H. Adsorption equilibria and kinetics of ethane and ethylene on zeolite 13X pellets. Microporous Mesoporous Mater 2022;343:112199. https://doi.org/10.1016/j.micromeso.2022.112199.

[121] Kamiuto K, Goubaru A, Ermalina. Diffusion coefficients of carbon dioxide within type 13X zeolite particles. Chem Eng Commun 2006;193:628–38.

[122] Bär N-K, McDaniel PL, Coe CG, Seiffert G, Kärger J. Measurement of intracrystalline diffusion of nitrogen in zeolites NaX and NaCaA using pulsed field gradient n.m.r. Zeolites 1997;18:71–4. https://doi.org/10.1016/S0144-2449(96)00114-5.

Appendix A Attached data for Chapter 2

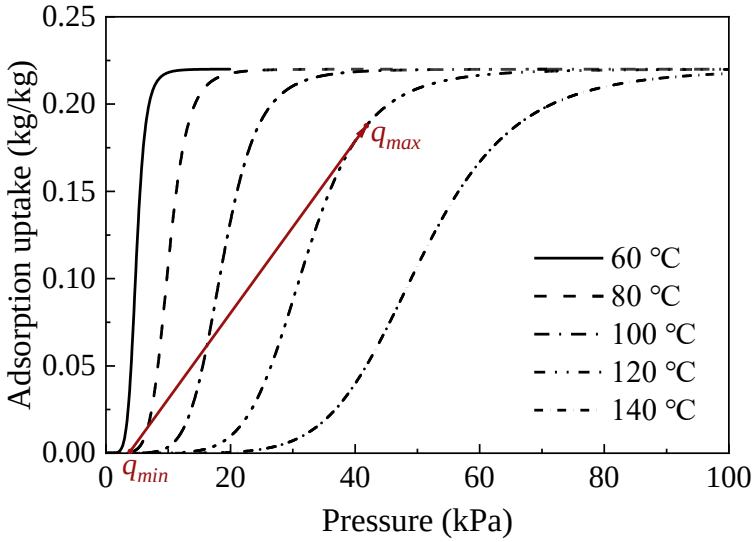

Fig. A.1 Adsorption isotherms of working pair AQSOA-Z05/water [86] and range of equilibrium uptake at reference conditions.

Table A.1 Heat transfer parameters required for adsorption bed [115].

Parameter	Meaning	Value
(A/M) (m^2/kg)	Ratio of heat transfer area to adsorbent mass	1.76
β	Finned ratio	6
η_o	Overall fin surface efficiency	0.95
N_b	Number of branch tube	12

d_i (mm)	Inner diameter of base tube	7.747
d_o (mm)	Outer diameter of base tube	9.525
$h_{ads/des}$ (W/(m^2·K))	Heat transfer coefficient on adsorption/desorption side	60

Appendix B Attached data for Chapter 3

Table B.1 Models for calculation of adsorption time constant in open adsorption.

	Model	Description
LDF equation [98]	$\frac{1}{k_{L,i}}=\frac{r_p q_{0,i}}{3k_f C_{0,i}}+\frac{r_p^2 q_{0,i}}{15\varepsilon_p D_{p,i} C_{0,i}}+\frac{r_c^2}{15D_{c,i}}$	
Film mass transfer coefficient [116]	$Sh=2.0+1.1Re^{0.6}Sc^{1/3}$ $Sh=\frac{k_f d_p}{D_m}$, $Re=\frac{\rho v d_p}{\mu}$, $Sc=\frac{\mu}{\rho D_m}$	A=1.06036, B=0.15610, C=0.19300, D=0.47635, E=1.03587, F=1.52996, G=1.76474, H=3.89411.
Pore diffusivity [117]	$\frac{1}{D_{p,i}}=\tau_p\left(\frac{1}{D_{m,i}}+\frac{1}{D_{k,i}}\right)$	
Knudsen diffusivity [117]	$D_{k,i}=97r_{po}\sqrt{\frac{T}{1000M_i}}$	σ is 3.996 Å for CO_2 and 3.667 Å for N_2.
Crystal diffusivity [117]	$D_{c,i}=D_{c0,i}\mathrm{e}^{-\left(E_{a,i}/RT\right)}$	ε/k is 190 K for CO_2 and 99.8 K for N_2.
Molecular diffusivity [118]	$D_m=\sum_{i=1}^{n}y_i D_{m,i}$, $D_{m,i}=\frac{1-y_i}{\sum_{j=1,j\neq i}^{n}\frac{y_j}{D_{ij}}}$ $D_{ij}=\frac{1.8583\times10^{-2}\sqrt{T^3(1/1000M_i+1/1000M_j)}}{P\sigma_{ij}^2\Omega_{ij}}$ $\Omega_{ij}=\frac{A}{(T^*)^B}+\frac{C}{\mathrm{e}^{DT^*}}+\frac{E}{\mathrm{e}^{FT^*}}+\frac{G}{\mathrm{e}^{HT^*}}$ $T^*=\frac{T}{(\varepsilon/k)_{ij}}$	The units of the involved parameters are listed in Nomenclature.

$$\sigma_{ij} = (\sigma_i + \sigma_j)/2, \quad (\varepsilon/k)_{ij} = \sqrt{(\varepsilon/k)_i (\varepsilon/k)_j}$$

Table B.2 Parameters for calculation of adsorption time constant in open adsorption.

Parameter	Value
r_c (μm)	0.75 [67]
r_{po} (nm)	140.7 [119]
ε_p	0.292 [119]
τ_p	2.5 [120]
$D_{c0,CO2}$ (m^2/s)	6.7e-13 [121]
$D_{c0,N2}$ (m^2/s)	1.9e-7 [122]
$E_{a,CO2}$ (J/mol)	11700 [121]
$E_{a,N2}$ (J/mol)	10800 [122]